UNIVERSITY OF CALIFORNIA SAN DIEGO

Application of Nitrogen-Vacancy Center Magnetometry to the Study of Novel Quantum Materials

A dissertation submitted in partial satisfaction of the
requirements for the degree Doctor of Philosophy

in

Physics

by

Nathan McLaughlin

Committee in charge:

Professor Chunhui Du, Chair
Professor Richard Averitt, Co-Chair
Professor Eric Fullerton
Professor Tenio Popmintchev

2024

The Dissertation of Nathan McLaughlin is approved, and it is acceptable in quality and form for publication on microfilm and electronically.

University of California San Diego

2024

DEDICATION

This dissertation is dedicated to all those who (for some reason) supported and encouraged me on this journey.

To my advisor, Professor Chunhui Du, who graciously accepted me into her lab, and through long hours of hard work guided me and contributed immensely to what I've been able to accomplish.

To my fellow labmates: Gerald Yan, Hanyi Lu, Mengqi Huang, Senlei Li, and Jingcheng Zhou, whose friendship and counsel were invaluable

To Eric Lee-Wong, and Evan Cobb, for being dedicated friends and constant commiseration partners.

To my parents and brothers, who have been my guiding examples.

And finally to my beloved Rebecca, whose patience and cherished company have kept my spirits high through the years, and with luck, for many years to come.

EPIGRAPH

Nature uses only the longest threads to weave her patterns,
so each small piece of her fabric reveals the organization of the entire tapestry.

Richard Feynman

TABLE OF CONTENTS

LIST OF FIGURES

ACKNOWLEDGEMENTS

I would like to acknowledge my advisor and chair of my committee, Professor Chunhui Du, for her unwavering support and for being a constant source of wisdom and advice. She graciously accepted me into her lab, and immediately began teaching and guiding me through the many trials and trevails of experimental physics. I would like to thank her for her trust in me, and for all the knowledge and experience I've gained over the years we've worked together.

I would also like to thank my colleagues in the Du group: Gerald Yan, Hanyi Lu, Mengqi Huang, Senlei Li, Jingcheng Zhou, and Dziga Djugba. Our work was often intensely collaborative, and I owe a great deal to the work and advice given to my labmates. Their companionship was key to keeping spirits high, both inside the lab and out. To my fellows in the UCSD physics department Evan Cobb, Jake Spisak, Zubenelgenubi Scott, Peter Kim, Max Poore, Eric Lee-Wong, James Wiley, and many others: of all that I have gained during my graduate education, I am perhaps most grateful for these friendships.

I must also thank my parents and brothers for all they have done to guide me. Through competitive science fairs and frequent dinnertime discussion, my family has instilled in me a love and appreciation for science in general, and physics in particular. More than that, they have consistently demonstrated patience, understanding, and thoughtfullness even in difficult times. It is by this example that I will continue to try to live.

From the bottom of my heart, I must also thank my partner Rebecca Chan for supporting me through the years. I am very grateful that you joined me in San Diego for my final two years there, and I can't wait to continue our adventures wherever life takes us next.

I would like to acknowledge Paul Y. Wang for his help with COMSOL simulations during the VO_2 project, and Francesco Casola for fabricating the diamond nanobeams used in this dissertation.

I would also like to acknowledge my collaborators: Prof. Eric E. Fullerton for the use of his Physical Property Measurement System (PPMS) for electrical transport characterization, and his student Yuxuan Xiao for help with sample preparation. I'm also very grateful to Eric

Lee-Wong for his help in sample preparation and measurement. Thanks also to Prof. Tenio Popmintchev and Prof. Richard Averitt for their generosity in agreeing to be on my committee, and for their mentorship.

Throughout my studies, valuable insight was provided on a number of topics by a number of fellow scientists: Yu-Hang Li, Ran Cheng, Yi-Zhuang You, Suyang Xu, Sheng-Chin Ho, Anyuan Gao, Peter Johnson, John Tranquada, Ruolan Xue, Mark Ku, and many others.

Chapter 2, is adapted with permission from Adv. Quantum Technol. 202000142 (2021). Copyright 2021 John Wiley and Sons. The dissertation author was an author of this paper, and coauthors are Yoav Kalcheim (equal contribution), Albert Suceava, Hailong Wang, Ivan K. Schuller, and Chunhui Rita Du

Chapter 3 is adapted with permission from Nano Lett. 2021, 21, 17, 7277–7283. Copyright 2021 American Chemical Society. The dissertation author was an author of this paper, and coauthors are Hailong Wang, Mengqi Huang, Eric Lee-Wong, Lunhui Hu, Hanyi Lu, Gerald Q. Yan, Genda Gu, Congjun Wu, Yi-Zhuang You, and Chunhui Rita Du

Chapter 4 is adapted with permission from Nano Lett. 2022, 22, 14, 5810–5817. Copyright 2022 American Chemical Society. The dissertation author was an author of this paper, and coauthors are Chaowei Hu, Mengqi Huang, Shu Zhang, Hanyi Lu, Gerald Q. Yan, Hailong Wang, Yaroslav Tserkovnyak, Ni Ni, and and Chunhui Rita Du

Chapter 5 is adapted with permission from ACS Nano 2023, 17, 24, 25689–25696. Copyright 2023 The Authors. The dissertation author was an author of this paper, and coauthors are Senlei Li, Jeffrey A. Brock, Shu Zhang, Hanyi Lu, Mengqi Huang, Yuxuan Xiao, Jingcheng Zhou, Yaroslav Tserkovnyak, Eric E. Fullerton, Hailong Wang, and Chunhui Rita Du

VITA

2018	Bachelor of Arts, University of California, Davis
2018–2020	Teaching Assistant, Department of Physics University of California, San Diego
2019–2023	Research Assistant, University of California San Diego
2023	Short-Term Affiliate, Georgia Institute of Technology
2024	Doctor of Philosophy, University of California San Diego

PUBLICATIONS

Wang, Xiaoche, Yuxuan Xiao, Chuanpu Liu, Eric Lee-Wong, **Nathan J. McLaughlin**, Hanfeng Wang, Mingzhong Wu, Hailong Wang, Eric E. Fullerton, and Chunhui Rita Du. "Electrical control of coherent spin rotation of a single-spin qubit." npj Quantum Information 6, no. 1 (2020): 78.

Nathan J. McLaughlin, Yoav Kalcheim, Albert Suceava, Hailong Wang, Ivan K. Schuller, and Chunhui Rita Du. "Quantum Sensing of Insulator-to-Metal Transitions in a Mott Insulator." Advanced Quantum Technologies 4, no. 5 (2021): 2000142.

Nathan J. McLaughlin, Hailong Wang, Mengqi Huang, Eric Lee-Wong, Lunhui Hu, Hanyi Lu, Gerald Q. Yan et al. "Strong correlation between superconductivity and ferromagnetism in an Fe-chalcogenide superconductor." Nano Letters 21, no. 17 (2021): 7277-7283.

Wang, Hailong, Shu Zhang, **Nathan J. McLaughlin**, Benedetta Flebus, Mengqi Huang, Yuxuan Xiao, Chuanpu Liu et al. "Noninvasive measurements of spin transport properties of an antiferromagnetic insulator." Science advances 8, no. 1 (2022): eabg8562.

Nathan J. McLaughlin, Chaowei Hu, Mengqi Huang, Shu Zhang, Hanyi Lu, Gerald Q. Yan, Hailong Wang, Yaroslav Tserkovnyak, Ni Ni, and Chunhui Rita Du. "Quantum imaging of magnetic phase transitions and spin fluctuations in intrinsic magnetic topological nanoflakes." Nano Letters 22, no. 14 (2022): 5810-5817.

Huang, Mengqi, Jingcheng Zhou, Di Chen, Hanyi Lu, **Nathan J. McLaughlin**, Senlei Li, Mohammed Alghamdi et al. "Wide field imaging of van der Waals ferromagnet Fe3GeTe2 by spin defects in hexagonal boron nitride." Nature communications 13, no. 1 (2022): 5369.

Yan, Gerald Q., Senlei Li, Tatsuya Yamamoto, Mengqi Huang, **Nathan J. McLaughlin**, Takayuki Nozaki, Hailong Wang, Shinji Yuasa, and Chunhui Rita Du. "Electric-Field-Induced Coherent Control of Nitrogen-Vacancy Centers." Physical Review Applied 18, no. 6 (2022): 064031.

Li, Senlei, Mengqi Huang, Hanyi Lu, **Nathan J. McLaughlin**, Yuxuan Xiao, Jingcheng Zhou, Eric E. Fullerton, Hua Chen, Hailong Wang, and Chunhui Rita Du. "Nanoscale magnetic domains in polycrystalline Mn3Sn films imaged by a scanning single-spin magnetometer." Nano Letters (2023).

Zhou, Jingcheng, Gerald Q. Yan, Mengqi Huang, **Nathan J. McLaughlin**, Chunhui Rita Du, and Hailong Wang. "Quantum sensing of local stray field environment of micron-scale magnetic disks." Applied Physics Letters 123, no. 2 (2023).

Nathan J. McLaughlin, Senlei Li, Jeffrey A. Brock, Shu Zhang, Hanyi Lu, Mengqi Huang, Yuxuan Xiao, Jingcheng Zhou, Yaroslav Tserkovnyak, Eric E. Fullerton, Hailong Wang, and Chunhui Rita Du. "Local Control of a Single Nitrogen-Vacancy Center by Nanoscale Engineered Magnetic Domain Wall Motion" *Manuscript in preparation*

Chunli Tang, Laith Alahmed, Muntasir Mahdi, Yuzan Xiong, Jerad Inman, **Nathan J. McLaughlin**, Christoph Zollitsch, Tae Hee Kim, Chunhui Rita Du, Hidekazu Kurebayashi, Elton J.G. Santos, Wei Zhang, Peng Li, and Wencan Jin "Spin dynamics in van der Waals magnetic systems" Physics Reports 1032, (2023): 1-36.

ABSTRACT OF THE DISSERTATION

Application of Nitrogen-Vacancy Center Magnetometry to the Study of Novel Quantum Materials

by

Nathan McLaughlin

Doctor of Philosophy in Physics

University of California San Diego, 2024

Professor Chunhui Du, Chair
Professor Richard Averitt, Co-Chair

The nitrogen-vacancy center has been an active subject of investigation for decades. Recently however, the pace of this research has accelerated dramatically to take advantage of the superlative qualities possessed by these optically active defects in diamond, including their extended quantum coherence, single-spin addressability, and their ability to probe magnetic fields non-invasively and with ultra-high sensitivity in a broad temperature range. The peculiar qualities of NV centers, including their diverse and extraordinary modes of measurement, are explored in this dissertation. From basic diamond nanostructures, to the cutting-edge scanning modes of research, the development and implementation of various techniques in NV magnetometry are

hereafter traced. Along the way, these methods are applied to VO_2 (a Mott insulator), FTS (a 2D superconductor possessing a ferromagnetic moment), the $MnBi_2Te_4$ $(Bi_2Te_3)_n$ class of materials possessing non-trivial quantum transport properties, and to the study of domain walls in [Co-Ni] multilayer heterostructures. These studies were conducted using a combination of home-built confocal and widefield microscope setups, and commercially acquired scanning measurement systems. In this, I hope to document a journey of understanding and utilization of the NV center defect, starting from basic applications through to the current state-of-the-art. The NV center is likely the most studied optically active intrinsic spin qubit to date, but these methods may be expanded and applied to a whole class of optical defects in diamond, silicon carbide, and now 2-dimensional van der Waals heterostructure systems. The countless opportunities these studies present in the field of quantum computation and quantum sensing are just beginning to emerge.

Chapter 1

Background Information

1.1 Introduction

As the world reaches inexorably towards quantum technologies to advance past the limitations of classical architectures, nitrogen-vacancy (NV) centers in diamond have been for decades been reliably used to advance our understanding in the areas of quantum sensing[1,2], quantum imaging[3–5], and quantum computation[6–10]. This is in part owing to their incredible quantum coherence from milli-kelvin[11] to above room temperature[12], and their ultra-high magnetic field sensitivity[2,5,13]. This chapter will describe the necessary background information as to why and how these defects can be used to optimal effect to advance our understanding of novel magnetic systems, and towards the development of quantum hybrid devices, which will be necessary to continue and invigorate the quantum revolution.

1.2 Nitrogen-Vacancy Center Defect

1.2.1 NV Center crystalline lattice structure

The nitrogen-vacancy (NV) defect consists of a substitutional nitrogen defect adjacent to a lattice vacancy on a nearest-neighbor site, as depicted in Figure 1.1a. The NV center therefore has a well defined direction, which must necessarily respect the four distinct C−C bond directions in the diamond lattice[1,14]: [111], [$\bar{1}\bar{1}1$], [$1\bar{1}1$], [$\bar{1}11$]. The NV center has been observed to occur in two charge states: the neutral NV^0 state and the negatively charged NV^-

state. The NV^0 state is formed by 5 electrons, two of which are contributed by the N atom, and the other three from the dangling bonds left by the C atoms surrounding the vacancy. This results in an overall spin S = 1/2 system. With the addition of one more electron received by a nearby substitutional N donor[15,16], the total number is brought up to 6 electrons, resulting in the negatively charged NV^- state with an overall S = 1 spin triplet state. It is perhaps more intuitive to consider the NV^- as consisting of two holes, rather than 6 electrons. While the neutral charge state NV^0 has been utilized in quantum sensing experiments[17–19], the sole spin defect state discussed in this dissertation will be the negatively charged NV^- state, and hereafter this state will be referred to simply as an NV center.

1.2.2 NV center electronic energy levels

The NV center represents a three-level quantum system. This consists of a ground state triplet with $^3A_2$ symmetry and spin states $|m_s = 0, \pm 1\rangle$, and excited state triplet with ^3E symmetry and spin states $|m_s = 0, \pm 1\rangle$, and two intermediate singlet states with $^1A_1$ and ^1E symmetry, and spin states $|m_s = 0\rangle$ for both. A magnetic spin-spin interaction means that the $|m_s = \pm 1\rangle$ spin states are separate from the ground $|m_s = 0\rangle$ by a zero field splitting (ZFS) parameter D_{gs} = 2.87 GHz and D_{es} = 1.42 GHz for the ground state and excited state, respectively. The $|m_s = \pm 1\rangle$ are degenerate to each other in zero external field conditions.

With the addition of an external field oriented along the NV-axis $B_{||}$, the $|m_s = \pm 1\rangle$ will experience Zeeman splitting, with a magnitude given by: $2\tilde{\gamma}B_{||}$, where $\tilde{\gamma} = g\mu_B/h$ = 2.8 MHz/G is the gyromagnetic ratio of the NV center. In a real system, there is also an off-axis parameter E $\approx$ 5 MHz, which appears due to physical strain in the diamond lattice, and may account for a small splitting between the $|m_s = \pm 1\rangle$ spin states. The Hamiltonian $\mathscr{H}$ for this system is then given as[1]:

$$\mathscr{H} = DS_z^2 + E(S_x^2 - S_y^2) + \tilde{\gamma}\mathbf{B}\cdot\mathbf{S} \tag{1.1}$$

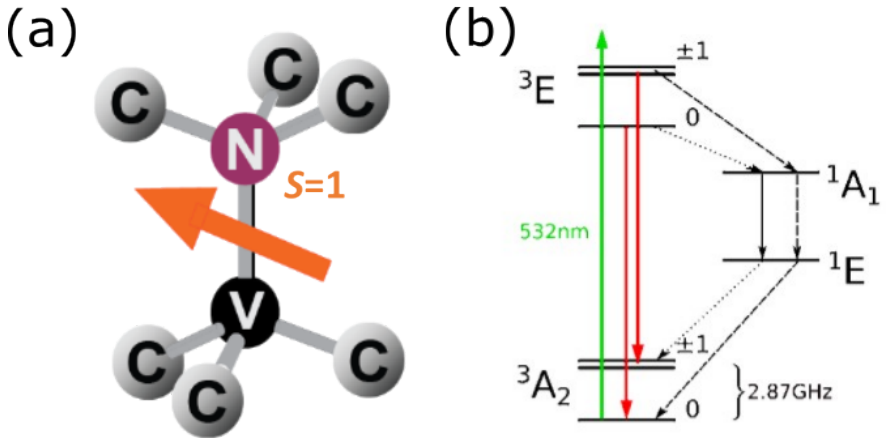

Figure 1.1. Basic structure and photophysics of NV center defect a) Schematic of lattice structure of NV center spin-1 defect in diamond lattice. b) Energy levels for the NV center spin state.

the first term of which represents the zero-field splitting of the $|m_s = \pm 1\rangle$ and $|m_s = 0$ states, the second term represents mechanical strain induced effects, and the third term relates to Zeeman splitting.

The NV center is a defect which can be initialized and read-out optically. Transitions between the ground and excited states may be effected off-resonantly (usually by visible λ = 532 nm or 515nm green laser light, due to high commercial availability). As depicted in Figure 1.1b, after absorption of a green photon, the NV in an $|m_s = 0\rangle$ state may undergo a spin-conserving transition from the ground to an excited vibronic state. This state will quickly undergo a phonon-mediated relaxation into the electronic excited $|m_s = 0\rangle$ state. After a brief lifetime of $\approx$10 ns, the NV will decay either directly back to the electronic ground state. This will either release optical radiation at the zero-phonon line (ZPL) of 637 nm, if the decay happens directly into the electronic ground state, or it will release radiation into a broad phonon sideband ($\lambda \approx$ 637-750 nm), if again there is a radiation-less phonon-mediated relaxation to the electronic ground state. For $|m_s = \pm 1\rangle$, the relaxation method to the ground state is no longer spin-conserving, nor is

it radiative[1]. NV centers in the excited $|m_s = \pm 1\rangle$ spin states have some probability to decay through an inter-system crossing through the $^1A_1$ and ^1E singlet spin states, which have a longer spin lifetime on the order of 100s of nanoseconds[20,21]. The final radiation-less transition may happen into either the ground $|m_s = 0\rangle$ or $|m_s = \pm 1\rangle$ states with equal probability. This feature of the $|m_s = 0\rangle$ and $|m_s = \pm 1\rangle$ spin states possessing different optical relaxation properties introduces the concept of spin-dependent photoluminescence (PL), which the the basis for all subsequent measurement techniques in NV measurements. In summary, NV centers in the $|m_s = 0\rangle$ state appear darker under green laser illumination than do NV centers in the $|m_s = \pm 1\rangle$ states.

These optical properties would be interesting, but unhelpful without a consistent way to manipulate the NV spin state. Fortunately this is trivial to accomplish with the application of RF magnetic fields. After initialization in the ground $|m_s = 0\rangle$ state, application of microwave fields at frequencies resonant with NV transition energies will drive the NV center into the $|m_s = \pm 1\rangle$ spin states, thus allowing the possibility of mapping the relative location of these resonances to the ZFS value, and deducing the applied external static field condition. With these properties in mind, subsequent sections will describe in more detail the various measurement modes available to an NV researcher

1.3 NV center measurement techniques

1.3.1 Continuous wave Optically Detected Magnetic Resonance (ODMR)

Optically dependent magnetic resonance (ODMR) measurements are the simplest and most essential measurement which can be made of the NV center. Continuous-wave ODMR measurements or continuous-wave electron spin resonance (CW-ESR) measurements are performed with continous illumination of the NV center by green laser light at 532 nm or 515 nm. The frequency of an RF magnetic field applied via an adjacent Au stripline is then swept.

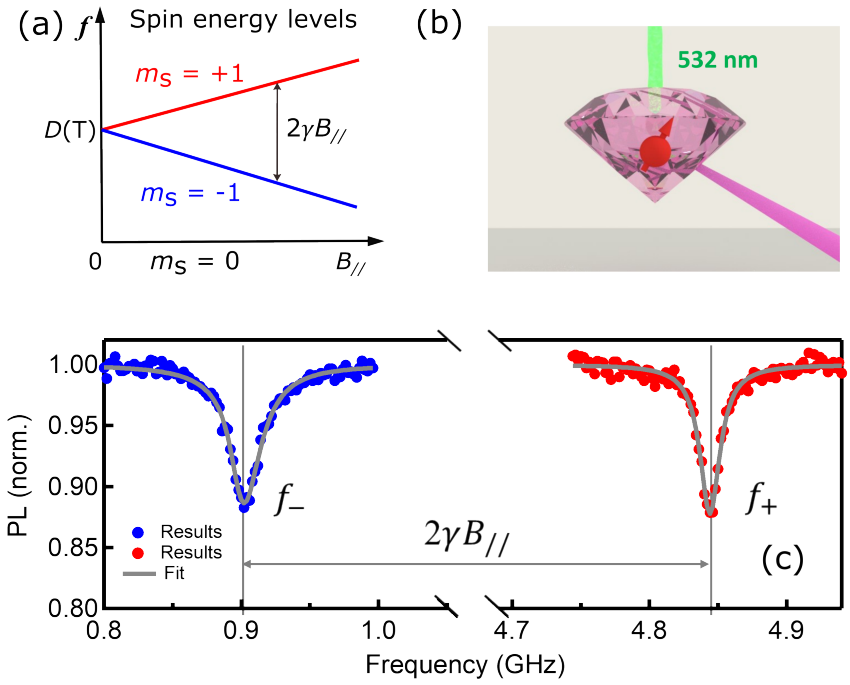

Figure 1.2. Optically detected magnetic resonance measurements of an NV center. (a) Zeeman effect induced splitting of degenerate $|m_s = \pm 1\rangle$ spin states due to applied external field $B_{||}$. (b) Schematic showing NV defect releasing red photons in response to a readout pulse from a 532 nm green laser. (c) An ODMR spectrum in which the measure $B_{||} = 700G$. This figure is adapted from Ref. [22].

While the RF frequency is off-resonant with the NV center $|m_s = \pm 1\rangle$ spin states, the NV in its bright, maximum photoluminescence (PL) state. When the RF frequency matches the $|m_s = +1\rangle$ or $|m_s = -1\rangle$ resonances, a dip in PL is seen. With zero applied field, one will observe a single dip in photoluminescence located at f = 2.87 GHz. For an applied magnetic field with non-zero projection on the NV quantization axis for a single NV center, two PL dips will be seen. The Zeeman induced splitting is shown in Figure 1.2a, and a dataset showing these resonance dips is given in Figure 1.2c. The general format of an NV experiment is shown schematically in Figure 1.2b. By noting the location of these resonance dips, the projection of an externally applied field along the NV-axis is determined as[1]:

$$B_{NV} = \frac{f_+ - f_-}{2\tilde{\gamma}} \tag{1.2}$$

where $f_{\pm 1}$ are the frequencies of the resonant frequencies for the $|m_s = \pm 1\rangle$ spin states. Static external field oriented perpendicular to the NV-axis will have the effect of increasing the center frequency of the two transitions to >2.87 GHz. Since the initialization and readout both happen with the green laser illumination on, this technique, while extremely easy to implement, has a reduced PL contrast compared to other techniques, which will be discussed in the next section.

1.3.2 Rabi Oscillations

When continuous microwave excitation is applied to the NV center on resonance with either of the $|m_s = \pm 1\rangle$ frequencies, the NV spin state will coherently oscillate between the ground $|m_s = 0\rangle$ and the selected of the possible $|m_s = \pm 1\rangle$ spin states[24,25]. These are known as Rabi oscillations, and they are the first introduction to pulsed microwave manipulation measurements. The frequency of these oscillations depends primarily on the amplitude of the resonant RF field perpendicular to the NV center axis, as shown by the following relation[26]:

$$f_{Rabi} = \frac{\tilde{\gamma}}{\sqrt{2}} |\mathbf{e}_{NV} \times \mathbf{B}_{AC}| \tag{1.3}$$

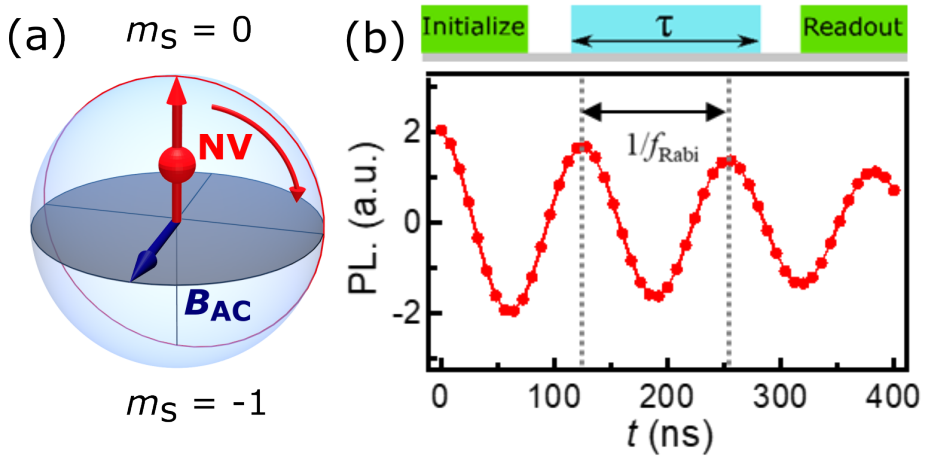

Figure 1.3. (a) Schematic of Rabi oscillations on the Bloch sphere, showing oscillations between the $|m_s = 0\rangle$ and $|m_s = -1\rangle$ states. (b) An experimental measurement spectrum of NV Rabi oscillation measured using the optical and microwave sequence illustrated in the top panel. This figure is adapted from Ref. [23]

where f_{Rabi} is the Rabi oscillation frequency, e_{NV} is a unit vector along the NV-axis direction, and B_{AC} is an AC magnetic field at the NV spin resonance frequency (either f_+ or f_-.) From this measurement is gained the ability to coherently control the relative populations in the ground spin states, for precise spin state control. For example a π-pulse, defined as half a Rabi oscillation period, will drive the NV spin state into either the $|m_s = +1\rangle$ or $|m_s = -1\rangle$ spin states with optimal efficiency. The spin manipulation described can be visualized more easily as happening on the surface of the Bloch sphere, as depicted in Figure 1.3a for the $|m_s = -1\rangle$ state. The pulsed measurement sequence used to accomplish this is shown in the top panel of Figure 1.3b, above an example of a measured Rabi spectrum.

1.3.3 Spin coherence measurements (T_1,T_2, and T_2^*)

The coherence properties of NV centers are typically given by reference to characterization of their T_1,T_2, and T_2^* coherence times. The origin, and significance of these times are

described below.

A spin-polarized NV state will eventually, due to phononic interactions with the crystal lattice, relax back into a thermally-mixed state. For example, an NV center with wavefunction $|\psi\rangle$ which has been optically initialized into the $|m_s = 0\rangle$ state ($|\langle\psi|m_s = 0\rangle|^2 = 1$ will relax until there is an equal distribution of probability for the NV to be in any of the ground spin states ($|\langle\psi|m_s = 0\rangle|^2 = |\langle\psi|m_s = +1\rangle|^2 = |\langle\psi|m_s = -1\rangle|^2 = 1/3$). The timescale over which this takes place is characterized by the T_1 time constant. This time constant is measured using the pulse sequence shown in the top panel of Figure 1.4b. The curves which result are shown is Figure 1.4b-c. Details on the fitting can be found in Appendix section A.5. The intimate involvement of phonons in this relaxation process means that the T_1 time is very sensitive to temperature. It is also affected by misalignment of applied magnetic fields, and from impurities in the diamond[1,14,17]. By altering the Zeeman induced splitting of the NV energy levels, as shown in the diagram in Figure 1.4a, different frequencies of magnetic noise can be probed[28–30].

The T_2 time characterizes spin decoherence, also known as homogeneous spin dephasing. This spin-spin relaxation time is intrinsic to a given NV and its local environment. The factors that effect the T_2 time include the presence of C^{13} impurities in the diamond, substitutional N electrons, other nearby NV spins, and other paramagnetic spin defects. The T_2 time is measured using a Hahn echo sequence[32], as shown in the top panel of Figure 1.5, above a typical T_2 dataset. The length of the NV coherence can be extended through dynamical decoupling sequences, or by using isotopically pure diamond samples[26].

The inhomogeneous spin dephasing time, or T_2^* time, can be considered the effective T_2 time. T_2^* is always less than or equal to the T_2 time, because these spin dephasing effects include spin-spin interactions in the NV local environment, and also local inhomogeneity in distribution of externally applied magnetic fields. The T_2^* time can be measured using a Ramsay sequence.

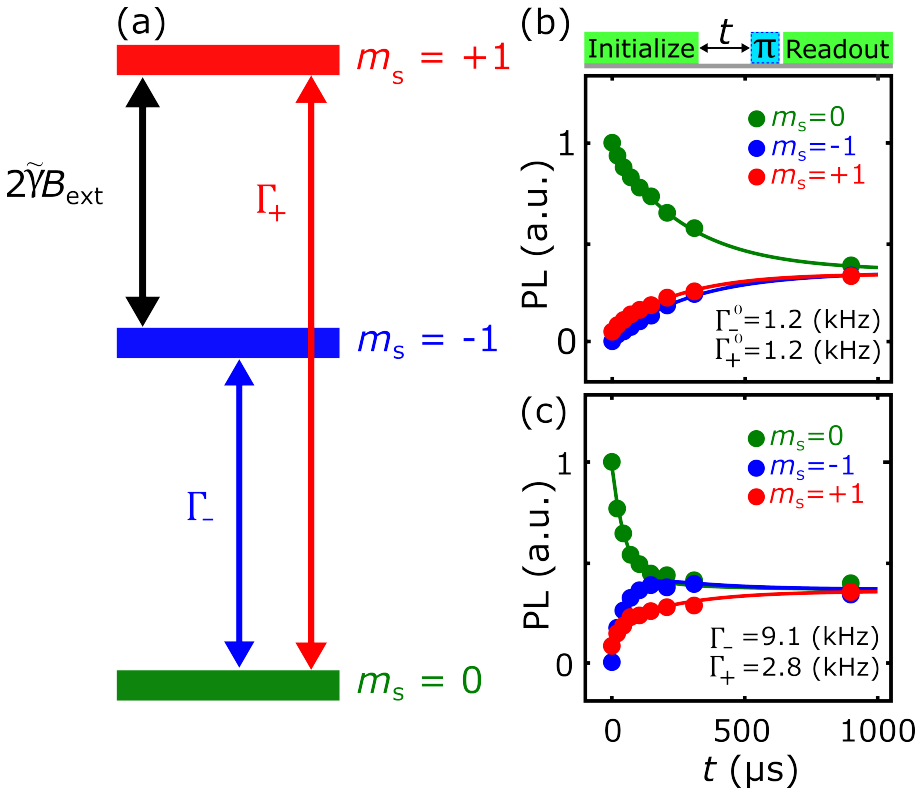

Figure 1.4. (a) Schematic illustration of NV spin relaxation in a three-level system. (b-c) A set of NV relaxometry data showing the spin dependent NV photoluminescence measured as a function of delay time t. The intrinsic NV relaxation rates are shown in (b), while the NV relaxation rates in proximity to a magnetic sample are shown in (c). This figure is adapted from Ref. [27]

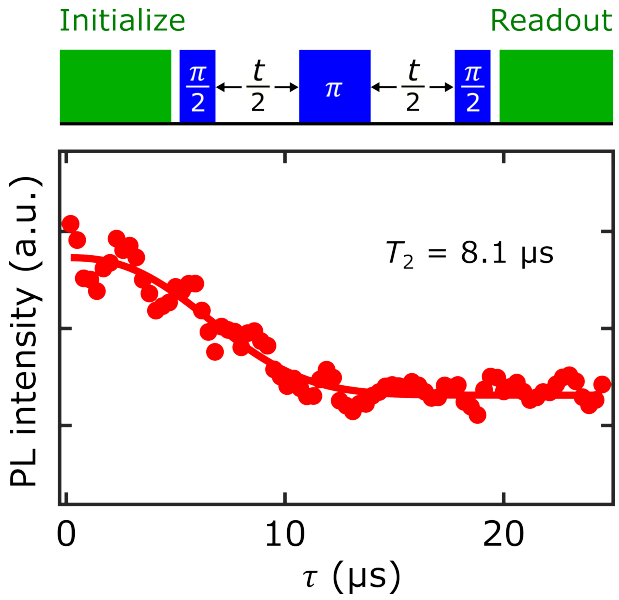

Figure 1.5. A measured Hahn echo spectrum of an NV center. The Hahn echo optical and microwave sequence are illustrated in the top panel. This figure is adapted from Ref. [31]

1.4 Diamond micro and nano-structures

1.4.1 Nanobeams

Diamond nanobeam microstructures containing single NV centers[33] were fabricated from a chemical vapor deposition (CVD) grown diamond by a combination of top-down etching and angled etching processes. The NV-to-sample distance was estimated to be $\approx$100 nm[34], ensuring sufficient thermal and field sensitivity. The nanobeams are fabricated on the [100] surface of the diamond, with their long axis along the [011] direction. The NV centers in these diamonds are naturally formed during growth at a density of around $1/\mu m^3$. The four possible NV axis directions are populated uniformly and randomly. To ensure a pristine diamond surface, acid cleaning is performed both before and after the fabrication process. Individual nanobeams are in the shape of an equilateral triangular prism with approximate dimensions of 500 nm $\times$ 500 nm $\times$ 10μm. The typical NV-to-sample distance of these nanobeams is approximately 100 nm. This tends to be more than sufficient for ensuring high thermal contact and field sensitivity. Diamond nanobeams are transferred to the surface of materials of interest using a micromechanical transfer stage utilizing a titanium tip with tip radius $<$0.5 μm, and 6° taper angle. Images of the transfer setup and process can be found in Figure 1.6.

1.4.2 Diamond membranes (ensembles)

For measurements of 2D materials in widefield microscopy experiments (optical setup described in Appendix section A.7.1, diamond membranes can be used[27,23,35,4,36]. Single crystal diamond membranes in this dissertation were fabricated for this purpose. They are fabricated to be approximately square, with dimensions of 3 mm $\times$ 3 mm, and thickness of 20-50 μm. The out-of-plane direction can either be along the diamond [001], or [111] axes, depending on the particular requirements of the experiment. [111] cut diamond membranes have 1 of the possible NV axis directions oriented directly out-of-plane[37], while [001] cut membranes have the 4 possible directions directed at 54° from out-of-plane, and aligned parallel to the sides of the

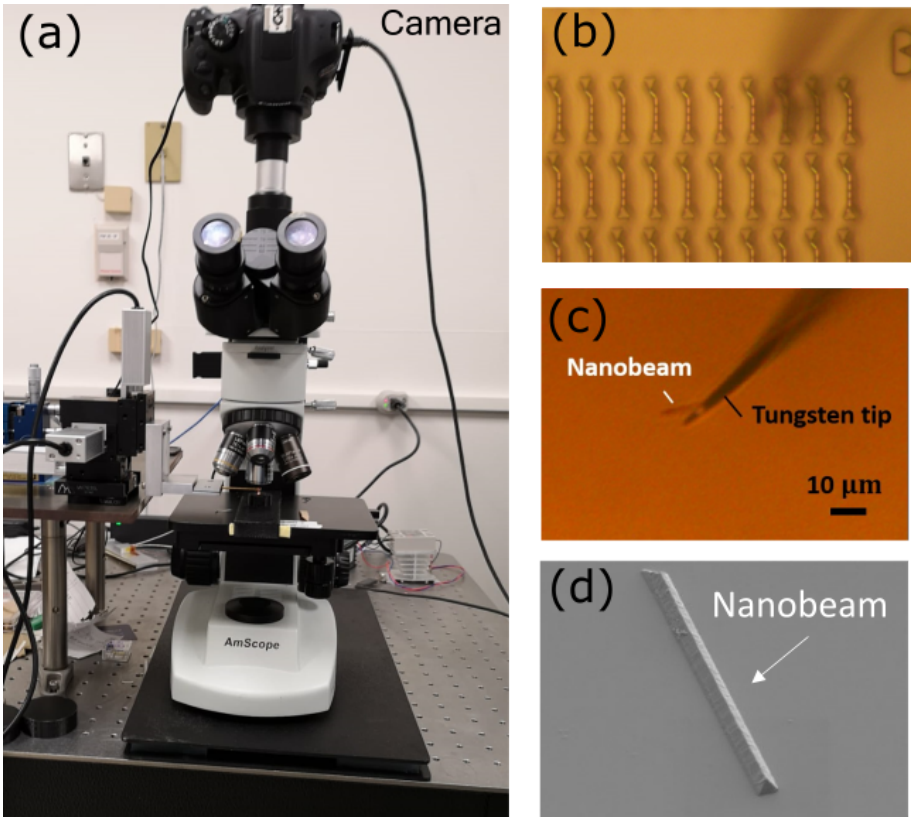

Figure 1.6. (a) Transfer stage for diamond nanobeams. An xyz-movement stage controls the movements of a tungsten tip with high precision. This allows breaking of a nanobeam from a fabricated diamond substrate (b), Carrying the nanobeam on the tungsten tip (c), and finally depositing the nanobeam on a sample of interest, as shown in an SEM image (d).

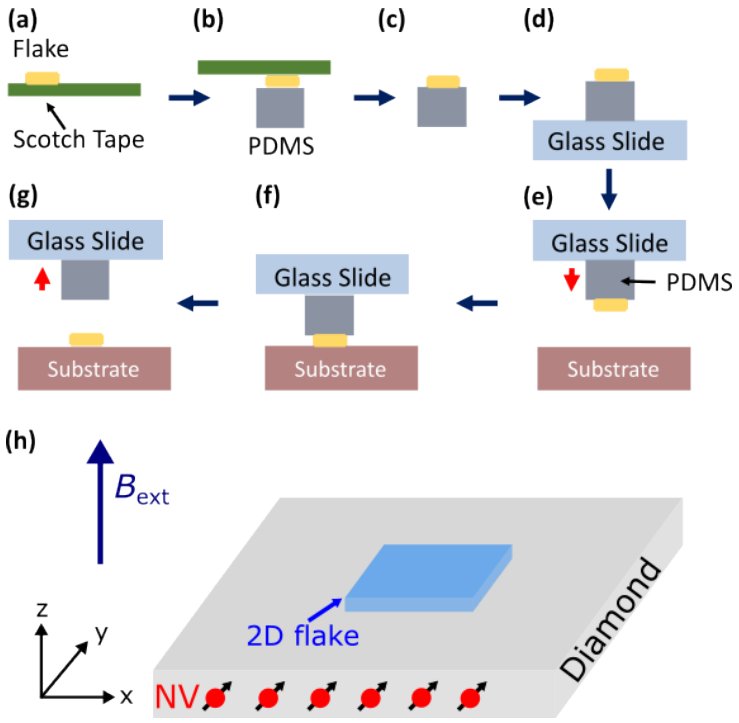

Figure 1.7. Schematic of the dry viscoelastic 2D transfer of 2D materials onto arbitrary substrates. (a) Flakes are cleaved into thinner sections using scotch tape. (b) The tape with flakes is then pressed against a block of PDMS. (c) Removing the tape will leave exfoliated flakes on the surface of the PDMS. (d) Securing flakes on a glass slide creates a stamping arm that can be mechanically controlled by a three dimensional micro-positioner. (e),(f) Positioning the sample to a desirable position and pressing down with the stamping arm to the surface of a substrate. (g) Slowly lifting the glass slide stamp separates the flake from the PDMS cube and leaves the flake on the substrate. (h) Schematic of the final product, ready for measurement. The 2D flake is in nanoscale contact with the diamond and shallowly implanted NV centers. Typically a bias field B_{ext} is applied to aid measurement using the NV centers, and to manipulate the magnetic properties of the 2D flake. This figure is adapted from Ref. [23]

membrane. NV centers are implanted in these membranes by $^{15}N_{+}$ ion irradiated, with energy between 3-6 keV. The depth of the resulting NV centers can be characterized by Stopping and Range of Ions in Matter (SRIM) Monte Carlo simulations[38]. Near-to-surface NV centers will have a higher sensitivity to static and dynamic magnetic fields, with a reduced coherence time and higher instability due to paramagnetic defects at the diamond surface[39]. On-chip Au waveguides were fabricated on the surface of diamond membranes by standard photolithography techniques, magnetron sputtering, and liftoff processes to deliver the microwave signals to manipulate NV spin states.

1.4.3 Diamond scanning probes

All the diamond probes used in the forthcoming scanned experiments were purchased commercially. These probes feature high-quality single crystal diamond structures at the end of a cantilever attached to a quartz tuning fork. The tuning fork is attached to a ceramic carrier plate, and is used in our custom atomic force microscope (AFM) system which expects probes in an Akiyama geometry. The probes used in this dissertation have four possible NV orientations, all at 54° from the out-of-plane direction. The single NV center is implanted at the end of a pillar, which extends down towards the sample. The height of this pillar is approximately 1-3 μm, and the pillar end is circular, with a diameter of 250-300 nm. A image of a typical diamond probe taken using a confocal microscope setup is shown in Figure 1.8.

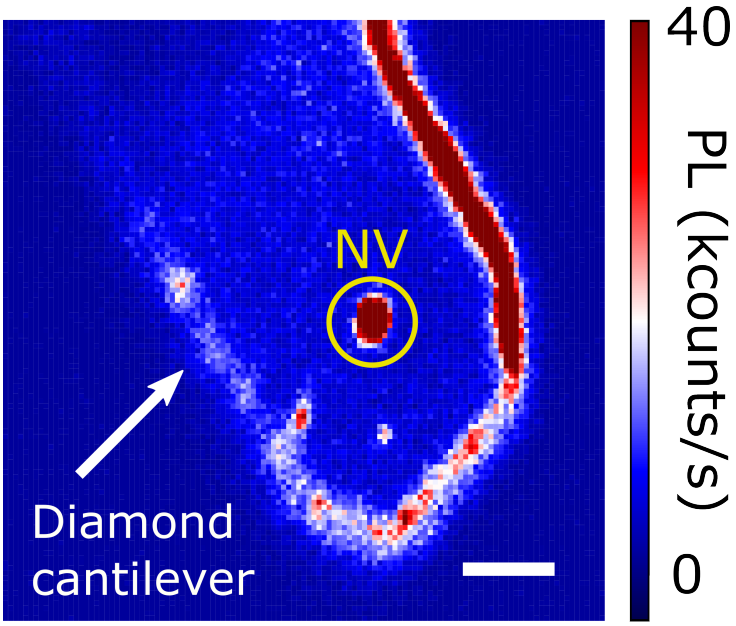

Figure 1.8. Confocal image of the diamond probe at the end of the AFM cantilever. Note the single NV center at the center of the probe. Other areas of high photoluminescence, for example around the edge of the probe, can be attributed to optical artifacts rather than the presence of additional NVs. This figure is adapted from Ref. [31]

Chapter 2

Quantum Sensing of Insulator-to-Metal Transitions in a Mott Insulator

2.1 Introduction

As technology begins to reach the fundamental limitations of the von Neumann computing architectures, new paradigms are urgently required to improve the processing speed, data storage capacity, and energy efficiency for next-generation information technologies.[40] Among many potential contenders, neuromorphic computing[41–43] has attracted immense research interest due its capability to mimic the highly interconnected structure of biological neural systems like the human brain.[44] Insulator-to-metal transitions (IMTs) in Mott materials featuring first-order, threshold firing type resistive switching behavior are directly relevant in this context due to their significant potential for implementing artificial spiking neurons in neuromorphic circuits.[45–49] Thus, great efforts have been devoted to understanding and controlling the mechanism for resistive switching in materials exhibiting an IMT.[50–54] Successful applications of IMTs to emergent neuromorphic computing platforms require advances in theory, material discovery, and equally importantly, a detailed knowledge of the local electrical and thermal properties of Mott materials down to the nanoscale regime.

Conventional research on IMTs has been mainly focused on global electrical transport measurements as well as structural characterizations, rendering limited information on the local properties of the studied materials. To address this challenge, here, we utilized nitrogen vacancy

(NV) centers to perform local quantum sensing of the voltage-induced IMT in a prototypical Mott material: vanadium dioxide VO_2.[42,46,55] Notably, the measured magnetic fields generated by the VO_2 devices exhibit a characteristic step-like jump around a "critical" electric current, in agreement with the formation of conducting filaments during the voltage-induced IMT.[42,56] The temperature profile we observed for both pristine and ion-irradiated VO_2 films are explained both by thermal[57] and nonthermal origins.[58] We expect that the presented NV-based quantum sensing platform can be extended naturally to other Mott insulators, offering a new perspective to reveal the local thermal and electrical behaviors in Mott-material-based neuromorphic devices.

2.2 Measurement platform and device structure

The studied VO_2 films were 170nm thick and were deposited on Al_2O_3 (012) substrates by reactive radio-frequency magnetron sputtering.[42] The growth was done in a 4 mTorr Ar:O_2 (92-8%) atmosphere and at a substrate temperature of 470 °C. The sample was then cooled down at a rate of 12 °C min-1. Two 125 nm thick Ti/Au electrodes were fabricated with a separation of 10 μm were fabricated using standard photolithography and e-beam evaporation on top of the pristine VO_2 films for electrical transport measurements. Some of these devices were then irradiated using focused ion beam (FIB) techniques. The region in between the electrical contacts was irradiated using a 30 keV, 6.2×10^{15} ions/cm^2 focused Ga-ion beam. This beam was rastered across the region of interest with a 50% overlap between successive raster locations to ensure a uniform dose. This width of this region was $\approx 2\ \mu$m, and extended just far enough so as not to damage the Ti/Au electrodes.

For NV measurements, we utilized patterned diamond nanobeams (details on fabrication and dimensions found in section 1.4.1) which were transferred on top of the VO_2 film between the two Au electrical contacts. A schematic of The measurement platform and device structure used are illustrated in Figure 2.1a, while a scanning electron microscope (SEM) image of an actual device is given in Figure 2.1b. A confocal image of this device is shown in Figure2.1c.

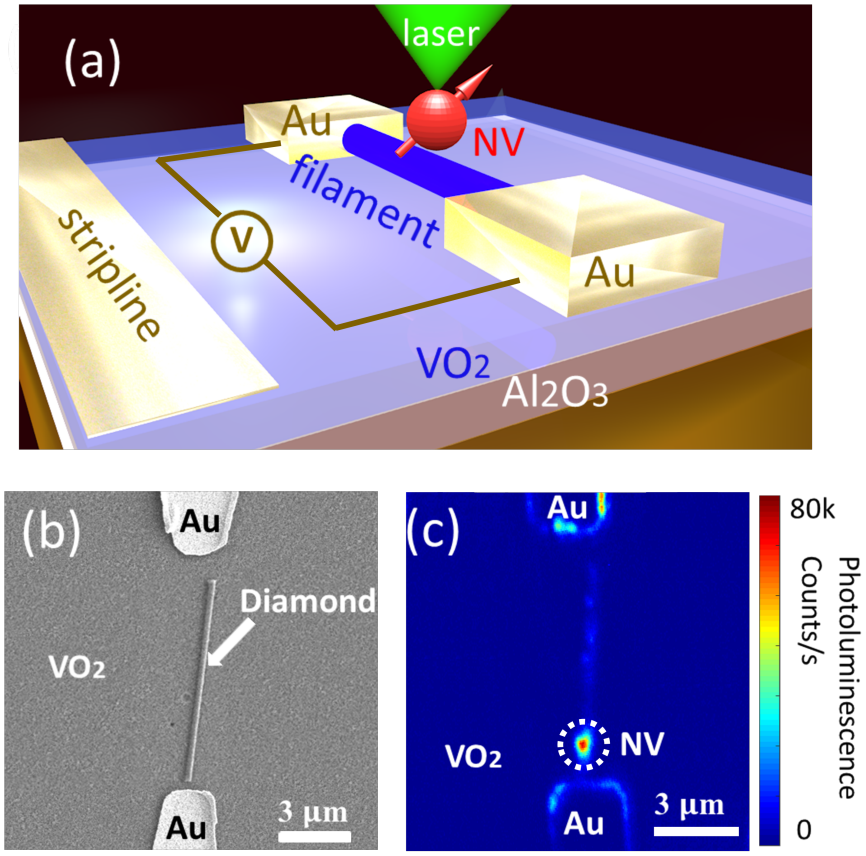

Figure 2.1. (a) Schematic of a prepared NV-VO_2 device consisting of two Au electrodes and an Au microwave stripline fabricated on top of a 170 nm thick VO_2 thin film. A diamond nanobeam containing individually addressable NV centers is transferred on top of the VO_2 film to perform local thermal and field sensing of IMT. (b) A scanning electron microscopy (SEM) image showing a patterned diamond nanobeam situated between the Au electrical contacts. (c) A photoluminescence image showing a diamond nanobeam containing a single NV spin positioned between the two the Au electrical contacts. This figure is adapted from Ref. [22].

The high photoluminescence at the indicated NV site demonstrates the single-spin addressability of our measurement system. The Au stripline fabricated next to the electrical contacts provides microwave control of the NV spin states.[34,25] The whole sample was mounted on a heating stage to allow for a precise adjustment of the base temperature. IMTs can be thermally and/or electrically triggered in the VO_2 device, accompanied by orders of magnitude decrease in electrical resistivity.[57–59] The NV center positioned on top of the VO_2 film serves as a local probe of the temperature and magnetic field at the NV site.

2.3 Results

2.3.1 Electrical transport characterization

We first performed electrical transport measurements to characterize the temperature induced IMT in the VO_2 device. Figure 2.2a shows the resistance of the VO_2 device as a function of the base temperature. The blue and the red curves correspond to the heating and cooling branches, respectively. The device features a characteristic IMT around 335 K, in agreement with the critical temperature T_c reported in previous works.[42,60] After establishing the resistance-temperature profile, we demonstrate an electrically induced IMT in the VO_2 device. In these measurements, the base temperature was maintained at a constant value below T_c, while an electric current I_{dc} applied in the VO_2 channel was slowly varied and the voltage was simultaneously measured between the two Au contacts. At a certain critical current I_c, a conducting filament stretching between the tips of the two Au contacts was formed in the VO_2 film, leading to a sudden and significant drop of the measured voltages as shown in Figure 2.2b. This is due to a metallic filament forming between the Au contacts which is visible by optical microscopy due to the change in optical constants (Figure 2.2c). Note that the magnitudes of the critical currents and voltages of the electrically induced IMT depend on the base temperature of the device. The closer the base temperature is to T_c, the smaller the electric power is required to activate the resistive switching as illustrated in Figure 2.2d. When the base temperature

of the device is too far below T_c, it is not possible to trigger voltage-induced IMTs in the VO_2 film without reaching excessively high voltages, where irreversible phase variations into other vanadium oxide compounds could occur.[59] In the following NV measurements, the base temperature of the sample is set to be above 295 K to avoid irreversible damage to the VO_2 devices.

2.3.2 NV data

Pristine VO_2

Next, we demonstrate the NV center's ability to accurately detect the local temperature and magnetic field environment of the VO_2 device during the voltage-induced IMTs. To perform the optically detected NV electron spin resonance (ESR) measurements, an external magnetic field was applied and aligned along the NV-axis and the base temperature of the device was maintained at a constant value. A constant microwave current with a frequency f was delivered by the nearby Au stripline. The component of the Oersted field parallel to the NV-axis ($B_{||}$) generated by the electric current flowing through the VO_2 was measured as illustrated in Figure 2.3a. The local temperature T_L at the NV site can be extracted from the NV ESR measurements as follows: $T_L = \frac{f_+ - f_-}{2b} - \frac{a}{b}$,[61–63] where a and b are fitting parameters equal to 2.8983 $\pm$ 0.002 GHz and -88.9 $\pm$ 5.8 kHz K^{-1}, respectively. These values are obtained by measuring $f_\pm$ as a function of the sample temperature. Since the measurements were performed in a vacuum environment of $\sim 10^{-6}$ and due to the nanoscale proximity established between the NV center and the VO_2 sample, the NV center is well thermalized with its immediate vicinity in the device in the steady-state, and the local temperature of the VO_2 sample can be reliably measured.

Figure 2.3b,c shows the extracted Oersted field and the local temperature T_L as a function of the applied electric current I_{dc} at three different base temperatures of 320, 325, and 330 K. For low electric currents $I_{dc} < I_c$, VO_2 is in a homogeneous semi-insulating state and the electric current is sparsely distributed in the device, leading to a negligibly small Oersted field at the NV site. When the electric current reaches its critical value ($I_{dc} = I_c$), the IMT is electrically

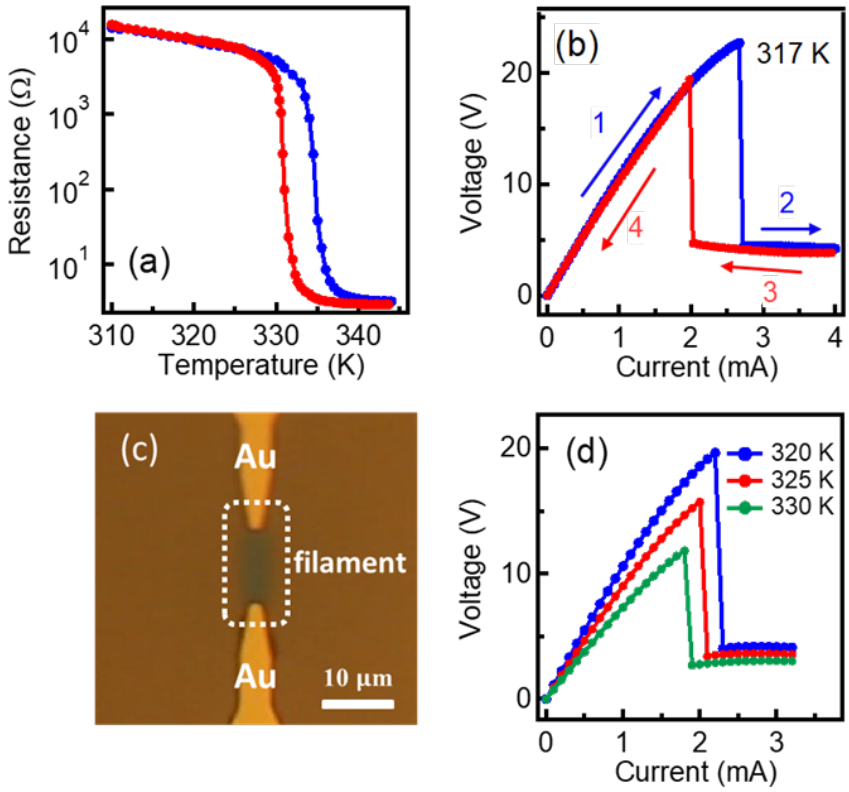

Figure 2.2. (a) Resistance of a pristine VO_2 device measured as a function of the base temperature. Blue and red curves correspond to the heating and cooling branches, respectively. (b) The voltage (V) measured as a function of applied current (I_{dc}) at a base temperature of 317 K. Blue and red curves correspond to increasing and decreasing current, respectively. When sweeping the current down, the filament shrinks and supports the metallic state with a lower critical current. (c) An optical image showing the formation of a conducting filament (dark color) between the two Au contacts. (d) Electric voltage (V) measured as a function of the applied current (I_{dc}) in the VO_2 device at three different base temperatures. This figure is adapted from Ref. [22].

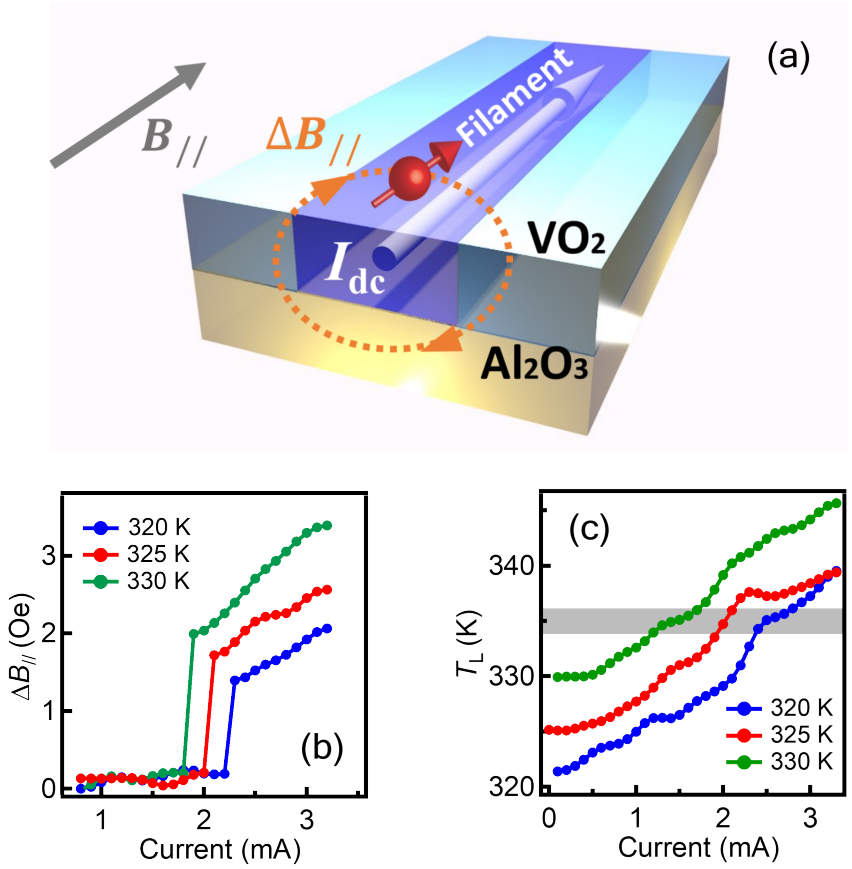

Figure 2.3. (a) Schematic of NV sensing of the local temperature and the Oersted field $\Delta B_{||}$ generated by the electric current flowing the VO_2 film. (b) Electric current dependence of the IMT-induced local magnetic field $\Delta B_{||}$ at the NV site. The blue, red, and green curves correspond to the base temperatures of 320, 325, and 330 K, respectively. The jumps correspond to the resistive switching events as shown in Figure 2.2d. (c) Local temperature extracted from the NV ESR measurements as a function of the electric currents. The experimental error of the measured temperature is ± 1.2 K, which mainly comes from the uncertainty of measuring NV ESR frequency and the calibration of temperature-dependent NV zero-field splitting frequency. The gray color stripe marks a temperature regime of 335 ± 1 K, where the thermally induced IMTs are expected to occur. This figure is adapted from Ref. [22].

triggered, accompanied by the formation of a conducting filament in the VO_2 film. Since the electric current is then mainly concentrated in the conducting filament, the local current density and the Oersted field experienced by the NV center are significantly enhanced (Figure 2.3b). These sudden jumps in magnetic field correspond to switching events observed in the electrical transport measurements.

In contrast to the jump-type variation of the Oersted field, the measured local temperature T_L exhibits a gradual increase as a function of I_{dc}. It is worth mentioning that T_L measured at different base temperatures reaches a similar value (≈335 K) during resistive switching, demonstrating the thermal origin of the voltage-induced IMT observed in a pristine VO_2 film.[57,64] At a sufficiently large electric current, Joule heating along the current path locally increases the temperature of the VO_2 film to the critical value (≈335 K) and triggers the formation of the conducting filaments.

Irradiated VO_2

In addition to Joule heating, it has been suggested that electric fields may also induce the IMT, but the origin of this effect is still debated.[58,65–71] A number of reports have indicated that the IMT may be induced without reaching the IMT critical temperature.[51,52,64,72–75] However, due to the inhomogeneous nature of the IMT and the need for simulations of the current and temperature distribution in the sample, direct evidence for the nonthermally induced IMT remains elusive. Local measurements of temperature in the nanoscale during the IMT are of great value to confirm the possibility of nonthermal switching. Next, we applied the NV-based quantum sensing platform to ion-irradiated VO_2 thin film devices to access the mechanism of nonthermally induced IMT.[76] We employed a focused ion beam to irradiate gallium ions onto the VO_2 film in a ≈2 μm wide region that connects the Au contacts. The gallium irradiation has interesting effects on the transport properties of the VO_2 thin film. First of all, the voltage-induced IMTs can be triggered at a much lower base temperature with reduced current/voltage/power as shown in Figure 2.4a. However, the resistance-temperature characteristics of the ion-irradiated VO_2

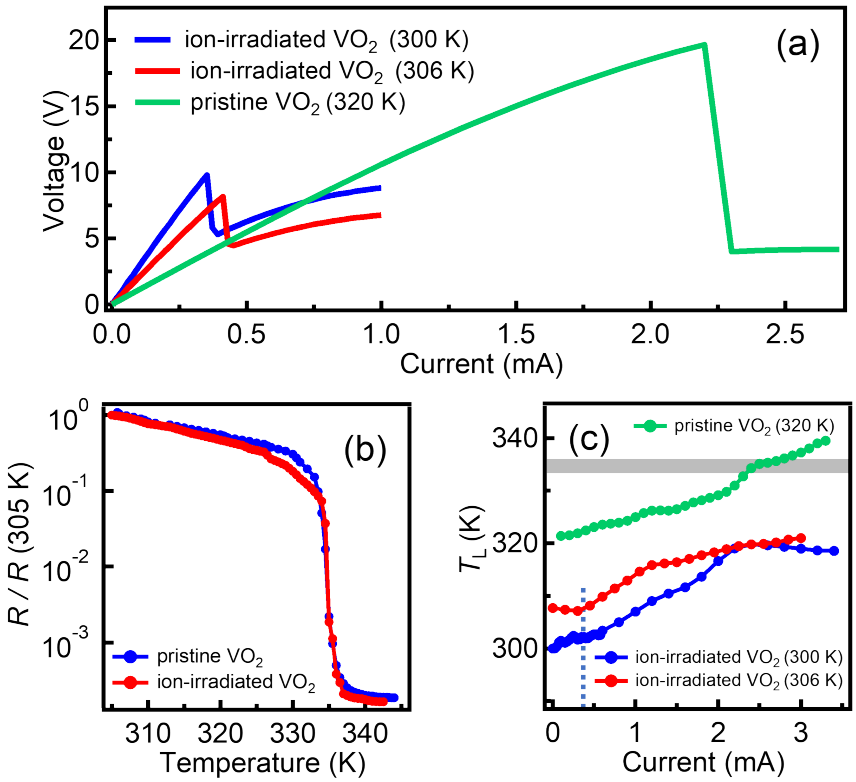

Figure 2.4. ((a) Comparison of voltage-induced IMTs in pristine and ion-irradiated VO_2 films. (b) Variation of the normalized resistance [R/R(305 K)] of pristine and ion-irradiated VO_2 devices measured as a function of the base temperature. (c) Local temperature extracted from the NV ESR measurements versus the applied electric current for pristine and ion-irradiated VO_2 devices. The uncertainty on the measured temperature is ± 1.2 K. The gray color stripe marks a temperature regime of 335 ± 1 K, where the thermally induced IMTs are expected to happen. The blue dash line indicates the critical current for the electrically induced IMTs. This figure is adapted from Ref. [22].

device remain largely the same, showing a similar T_c as in the pristine sample (Figure 2.4b). Figure 2.4c shows the local temperature extracted from the NV ESR measurements as a function of I_{dc}. In stark contrast to the pristine VO_2 sample, the local temperature measured at the critical current barely changes from the base temperature which can be up to 35 K lower than T_c. It is important to note that the NV center is situated on the symmetry axis between the two contacts and is in contact with the conducting filament formed in the ion-irradiated VO_2 device. The absence of substantial heating both before and after the switching process demonstrates the nonthermal origin of the electrically induced IMT in the ion-irradiated VO_2 sample.[58]

2.4 COMSOL Simulations

We have simulated our measurements in COMSOL Multiphysics software, to better understand the thermal and electrical interactions at play in our measurements. Relevant thermal and electrical material properties for the Au contacts, and the Al_2O_3 (sapphire) substrate are directly available from the COMSOL material database. The substrate was modelled as a 1280 $\times$ 1300 $\times$ 1000 μm block sufficiently large to encompass the dimension of a single VO_2 device. To accurately simulate heating of the device, we impose a constant temperature condition on the face of the substrate opposite the VO_2. This is very similar to the action of the resistive heater below our experimental device. The thermal conductivity κ of VO_2 is implemented as a step function: 3.4 W(m·K)$^{-1}$ for $300 < T < 340$ and 6 W(m·K)$^{-1}$ for 340 K $< T <$ 600 K.[77,78] κ for diamond and air is 2500 W(m·K)$^{-1}$ and 0.03 W(m·K)$^{-1}$,[79] respectively. The electrical conductivity of VO_2 was obtained using an experimental resistance-temperature curve for the device, which was then scaled so that the resistance of the simulated device was identical to that measured in experiment. Distributed ordinary differential equations were incorporated to account for the hysteresis present in the electrical conductivity of VO_2, as well as to suppress the conductivity in a small region around the leads, to reduce non-physical fringing effects.[64] The filament formation was modeled using Electrical Currents, Heat Transfer in Solids, and

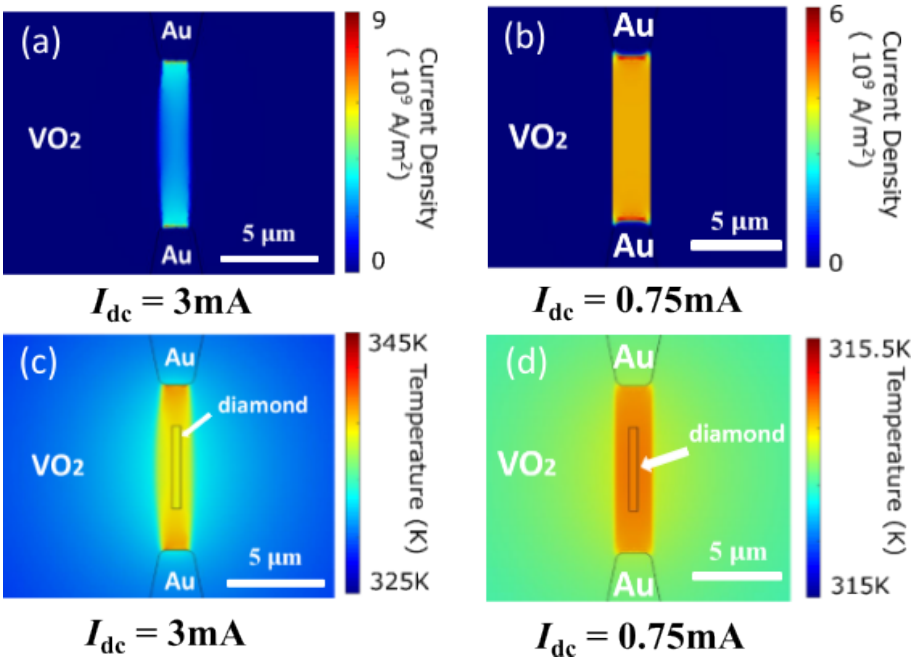

Figure 2.5. COMSOL simulations of current distribution in pristine (a) and irradiated (b) VO_2 with an applied electric current of 3mA and 0.75mA respectively. COMSOL simulations of the temperature profile in both cases are given for pristine VO_2 (c) and irradiated VO_2 (d), with a base temperature of 325 K and 315 K, respectively. Note that a simulated diamond nanobeam is located on the symmetry axis of the two Au contacts. This figure is adapted from Ref. [22].

Electromagnetic Heating packages. For pristine samples, the electrical and thermal conductivity only depend on the temperature. The irradiated region of a VO_2 sample was treated as having conductivity as a function of both temperature and the electric field. This approach was chosen as a result of the observation that minimal heating occurs before and after filament formation for irradiated samples, indicating that an electronic mechanism plays a role in the IMT. Once the filament is formed at higher current values, a separate approach needs to be employed as the electric field inside the filament would drop drastically and return the VO_2 to the insulating state. We use the effective temperature model to obtain a spatial approximation of where the filament would form.[64] Then, we treated the VO_2 in that region as having transitioned to the metallic behavior by imposing the electrical and thermal conductivities of the conducting phase. This measure allows for electric current values to extend into the regime beyond the IMT, while the irradiated devices still exhibit little heating as observed experimentally. In Figure 2.5a and Figure 2.5c and we simulate the current distribution and temperature profile for pristine VO_2 with an applied electric current of 3mA, and a base temperature of 325K. In Figure 2.5b and Figure 2.5d and we simulate the current distribution and temperature profile for irradiated VO_2 with an applied electric current of 0.75mA, and a base temperature of 315K. These simulations mimic many of the details that are observed experimentally. For example, the width of the current filaments (around 1 mA), and the fact that for the pristine sample, this width increases with increasing current. We also see that the magnetic field profile experienced by an NV center above the filament is in reasonable bounds, using the Biot-Savart Law, and that the diamond is well thermalized to the VO_2 surface, even assuming pessimistic values about the interfacial thermal conductivity between the diamond and the sample.

2.5 Mechanism of electric field assisted carrier generation in irradiated VO_2 devices

Our results are consistent with a previous study showing indirect evidence for nonthermal switching and support field-assisted carrier generation as the switching mechanism.[58,80,81]. With a sufficiently large electric field, in-gap states created by ion beam irradiation could be electrically excited, emitting charge into the conduction band, as illustrated in Figure 2.6a. This increases the number of free carriers and causes the collapse of the Mott insulator state through a doping-driven IMT.[58] We have studied the relationship between the conductance σ and the electric field E of the devices. If this phenomenon of non-thermally induced switching were the result of the Poole-Frenkel effect, we would expect the logarithm of conductance to have a square root dependence on the electric field: $\ln(\sigma) \propto E^{0.5}$. However, in our measurements, we observe a much better fit to a quadratic relationship between conductance σ and electric field E. Our fitting equation is: $\ln(\sigma) = \ln(\sigma_0) + \left(\frac{V}{E_0 d}\right)$, where σ_0 and E_0 are the fitting parameters. In this equation, $E = V/d$, where V is the applied voltage across the region of VO_2 of width d. The results of this fit are shown in 2.6b. This fitting implies a better theoretical agreement to the mechanism of phonon-assisted tunneling. In comparison to thermally induced resistive switching, we highlight that the critical currents are significantly reduced, as well as the energy dissipation in the doping-driven IMT, which may offer significant advantages for developing energy-efficient neuromorphic circuits in a broad temperature range.

2.6 Conclusion

These studies have served as a demonstration of NV centers as a sensitive local probe of the thermally and nonthermally induced IMTs in VO_2 devices. By measuring the local temperature and the magnetic field environment via the optically detected NV electron spin resonances, the underlying electrical phase transitions in proximal VO_2 devices was accessed in a nonperturbative way at the nanoscale. This technique allowed us to obtain direct evidence

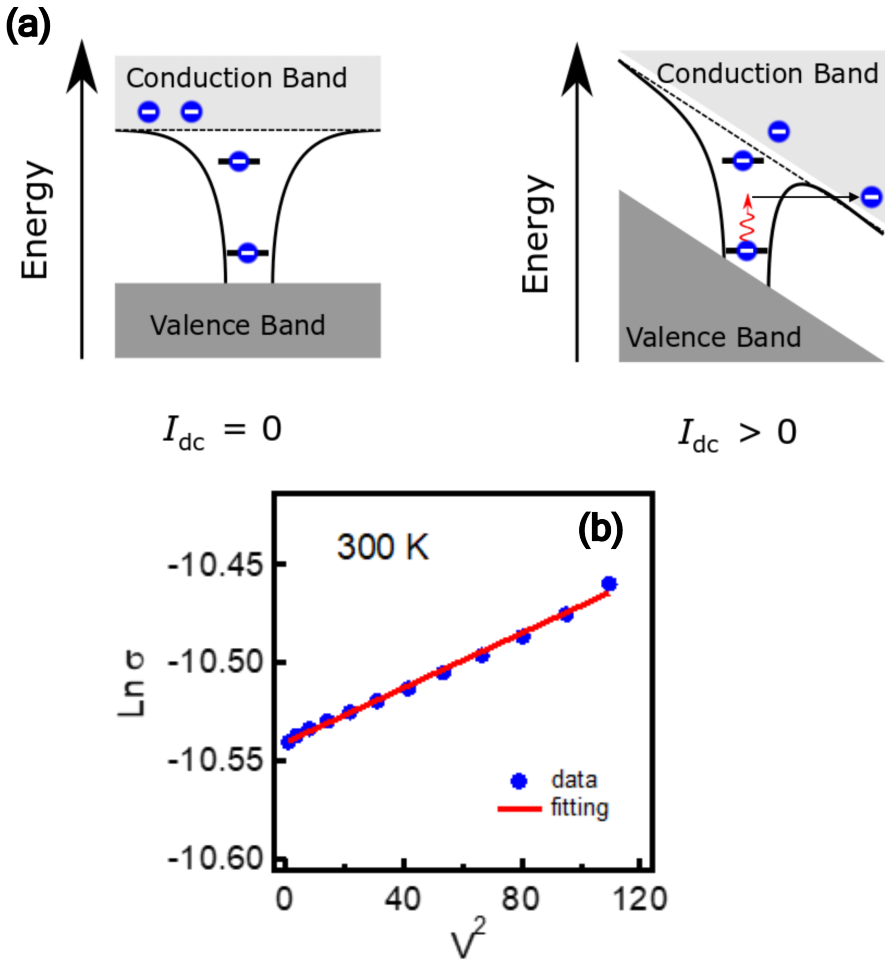

Figure 2.6. (a) Schematic of the field-assisted carrier generation through a doping-driven IMT. Application of a voltage allows electrons in new doped energy levels to tunnel into the conduction band with the assistance of phonons, as illustrated in the right panel. (b) Fit to the conductivity enhancement due to phonon-assisted tunneling for an irradiated VO_2 sample. Blue points are the experimental results and the red line is a fit to $\ln(\sigma) = \ln(\sigma_0) + \left(\frac{V}{E_0 d}\right)$, with d = 10 μm and E_0 = 3.79 MV/m. This figure is adapted from Ref. [22].

for a nonthermally induced electrical IMT in a Mott insulator. The findings also have important implications for our understanding of the physics of Mott insulators and their applications. By employing patterned diamond nanostructures with shallowly implanted NV centers,[82,13,83] we expect that the local resolution of such NV quantum sensing platform could potentially reach the few-nanometer length scale, offering new opportunities to reveal the electrical and thermal behaviors in Mott insulators and many other quantum materials. Additionally, using techniques described in the following chapters, we expect many more opportunities to demonstrate the coupling between NV centers and Mott insulators, to develop our understanding of next-generation neuromorphic devices.

2.7 Acknowledgements

Chapter 2, is adapted with permission from Adv. Quantum Technol. 202000142 (2021). Copyright 2021 John Wiley and Sons. The dissertation author was an author of this paper, and coauthors are Yoav Kalcheim (equal contribution), Albert Suceava, Hailong Wang, Ivan K. Schuller, and Chunhui Rita Du

Chapter 3

Strong Correlation Between Superconductivity and Ferromagnetism in an Fe-Chalcogenide Superconductor

3.1 Introduction

The interplay among topology, superconductivity, and magnetism promises to bring a plethora of exotic and unintuitive behaviors in emergent quantum materials. The family of Fe-chalcogenide superconductors $FeTe_xSe_{1-x}$ are directly relevant in this context due to their intrinsic topological band structure, high-temperature superconductivity, and unconventional pairing symmetry. Despite enormous promise and expectation, the local magnetic properties of $FeTe_xSe_{1-x}$ remain largely unexplored, which prevents a comprehensive understanding of their underlying material properties. Exploiting nitrogen vacancy (NV) centers in diamond, here we report nanoscale quantum sensing and imaging of magnetic flux generated by exfoliated $FeTe_xSe_{1-x}$ flakes, demonstrating strong correlation between superconductivity and ferromagnetism in $FeTe_xSe_{1-x}$. The coexistence of superconductivity and ferromagnetism in an established topological superconductor opens up new opportunities for exploring exotic spin and charge transport phenomena in quantum materials. The demonstrated coupling between NV centers and $FeTe_xSe_{1-x}$ may also find applications in developing hybrid architectures for next-generation, solid-state-based quantum information technologies.

Topological superconductors harboring exotic Majorana Fermions have received intensive research interest over the past several years due to their significant potential for developing transformative, fault-tolerant, quantum-computing paradigms.[84,85] This emergent class of superconductors is distinguishable from its conventional counterparts by its topologically protected surface or edge state, as well as exhibiting a range of exotic and highly interesting quantum phenomena.[84,86] Among the potential material candidates, the $FeTe_xSe_{1-x}$ family naturally stands out due to its high superconducting transition temperature, simple crystal structure, and intrinsic topological band structure due to the bulk band-inversion induced by spin-orbit coupling.[87–90]

Over the past few years, pioneering research efforts have gone toward experimentally investigating the topological nature and the superconducting properties of $FeTe_xSe_{1-x}$.[87,89,91] The topological superconductivity observed in these experiments is a consequence of the proximity effect from the bulk superconductivity to the surface Dirac state. It is natural to examine whether the surface superconductivity can provide important information about the bulk gap function symmetry. In particular, time-reversal symmetry as well as parity and charge conjugation are three fundamental discrete symmetries of interest. The existence or lack of time-reversal symmetry breaking (TRSB) is an important question for exploring pairing mechanisms in strongly correlated superconductors. TRSB pairing symmetries have been theoretically proposed in iron-based superconductors.[92] Experimentally, thermal transport and angle-resolved photoemission spectroscopy studies suggest the spontaneous TRSB and opening of a band gap at the surface Dirac cone in superconducting $FeTe_xSe_{1-x}$,[93,94] which indicates the presence of ferromagnetism induced by an intrinsic unconventional pairing symmetry.[95] The interplay among topology,[87,89,91,96] superconductivity,[87,90] and magnetism[93,94] makes $FeTe_xSe_{1-x}$ an attractive platform to explore a range of emergent quantum spin and charge transport phenomena,[94,97,98] such as Majorana Fermions[89,91] and higher-order topological superconductivity[99–101] as recently reported. Despite remarkable progress, detailed knowledge of the local magnetic properties of superconducting $FeTe_xSe_{1-x}$ remains elusive, and direct evidence to corroborate the coexistence of superconductivity and ferromagnetism in $FeTe_xSe_{1-x}$ is still lacking. The major difficulty

results from the fact that the magnetic flux generated by superconductors is often shielded by the Meissner effect,[102] which is challenging to access using conventional magnetometry methods.

Here, we use nitrogen-vacancy (NV) centers to perform nanoscale quantum imaging and sensing of magnetic flux generated by an exfoliated $FeTe_{0.7}Se_{0.3}$ (FTS) flake.[94] By performing NV Rabi oscillation measurements,[24,25] we directly image the spatial distribution of supercurrents in FTS. By measuring magnetic stray fields and fluctuations by the NV optical detection of magnetic resonance (ODMR) and relaxometry techniques,[34,29,30,3,103] we demonstrate strong correlation between superconductivity and ferromagnetism in FTS.[95] The presented NV quantum sensing and imaging platform operates in an accessible, table-top format, which can be extended naturally to a large family of two-dimensional van der Waals materials,[104] providing new opportunities for investigating local electrical and magnetic behaviors in emergent quantum materials.

3.2 Measurement Platform and sample

Figure 3.1a shows a schematic of our measurement platform, where a 140 nm thick FTS flake with lateral dimensions of $\sim$11 μm $\times$ $\sim$9 μm is transferred onto a single crystal diamond substrate containing NV centers implanted $\sim$5 nm below the surface. The density of NV centers is characterized to be $\sim 1500/\mu m^2$, providing a convenient platform to achieve wide-field imaging based on the ensemble of NV spins.[4,36,35] An on-chip Au stripline is fabricated on the diamond sample, allowing the application of microwave currents to control the quantum spin state of the NV centers. A photoluminescence image [Figure 3.1b] shows an overview of a prepared NV-FTS device, where an FTS flake is located $\sim$4 μm from the Au stripline. The exfoliated FTS flake exhibits the characteristic superconducting phase transition at T_c = 14.5 K, as shown in Figure 3.1c, in agreement with the previous electrical transport study.[93]

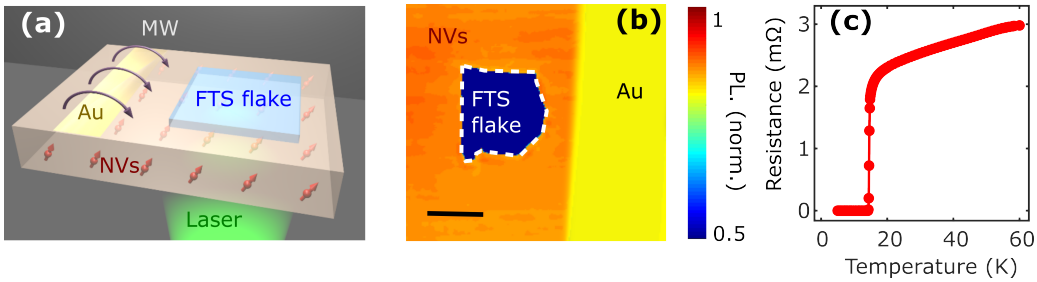

Figure 3.1. Measurement of magnetic flux generated by an exfoliated FTS flake by NV centers. (a) Schematic of an exfoliated FTS flake transferred onto a diamond membrane for NV wide-field magnetic imaging measurements. (b) Photoluminescence image showing an overview of a prepared NV-FTS device. The scale bar is 5 μm. (c) Electrical transport measurements show a characteristic superconducting phase transition at 14.5 K for an exfoliated FTS flake. (d,e) Schematic of Rabi oscillations on the Bloch sphere and an experimental measurement spectrum of NV Rabi oscillation. The top panel of (e) shows the optical and microwave sequence of NV Rabi oscillation measurements. This figure is adapted from Ref. [23].

3.3 Results

3.3.1 Imaging supercurrents with AC widefield microscopy

We first employed NV wide-field microscopy[4,36,35] to perform Rabi oscillation measurements to image circular AC supercurrents in the FTS flake. For more details on the rabi measurement, see Figure 1.3. The amplitude of the applied microwave magnetic field B_{AC} can be obtained by the frequency of the Rabi oscillation f_{Rabi} as follows: $B_{AC} = \frac{\sqrt{3} f_{Rabi}}{\gamma}$, where γ is the gyromagnetic ratio of an NV spin (more details shown in Figure 1.3). In the prepared NV-FTS device, the microwave magnetic field B_{AC} at individual NV sites contains two potential contributions: the oscillating Oersted field B_{MW} produced by the microwave current flowing in the on-chip Au stripline and the magnetic field B_{SU} generated by supercurrents in the FTS flake, as illustrated in Figure 3.2a,b. When $T > T_c$, the Rabi oscillation of NV centers is only driven by the Oersted field B_{MW}. When temperature falls below T_c, circular supercurrents in FTS modify

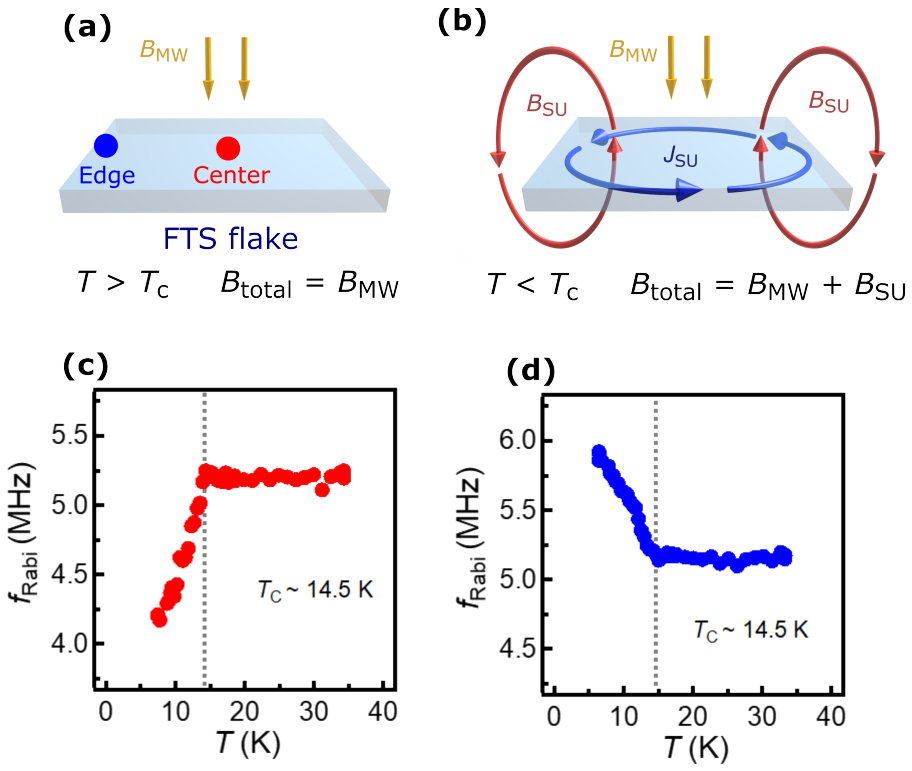

Figure 3.2. Local quantum sensing of superconducting phase transition of an FTS flake. (a,b) Schematic of the spatial profile of the microwave magnetic field environment of an FTS flake above and below T_c. (c), (d) Temperature dependence of Rabi oscillation frequency f_{Rabi} of NV centers located underneath the central (c) and edge (d) areas of the FTS flake. The Meissner screening effect reduces (increases) the effective microwave field in the central (edge) area of the FTS flake, leading to the opposite variations of f_{Rabi} across T_c. This figure is adapted from Ref. [23].

the spatial distribution of the microwave magnetic field surrounding the FTS flake. In the central area of the FTS flake, the microwave field B_{SU} generated by supercurrents is in the opposite direction of the external microwave field B_{MW}, effectively reducing the NV Rabi oscillation rate f_{Rabi}. B_{SU} and B_{MW} follow the same direction in the boundary area of the FTS flake, leading to an enhancement of f_{Rabi}. Figure 3.2c,d shows the temperature dependence of the measured Rabi oscillation frequency f_{Rabi} for NV centers underneath the central and boundary areas of the FTS flake, respectively. Notably, f_{Rabi} exhibits a sudden decrease (increase) when temperature falls below the T_c of FTS, in agreement with the picture of the Meissner screening effect discussed above.[105,106] By subtracting the external microwave field generated by the on-chip Au stripline, the internal magnetic field B_{SU} due exclusively to the circulating supercurrents in the FTS flake can be extracted. Figure 3.3a-c shows 2D maps of B_{SU} measured at 5, 8.5, and 10 K. When T = 5 K, magnetic flux expulsion due to the Meissner effect[106,107] leads to a negative magnetic field in the central area of the flake and a positive magnetic field in the edge area. Note that the sign of B_{SU} represents its orientation relative to the external microwave field. The magnitude of B_{SU} decreases with increasing temperature and eventually vanishes above T_c. Without considering the variation along the thickness direction, the spatially resolved B_{SU} allows us to reconstruct the 2D distribution of supercurrent J_{SU} in the FTS flake, as shown in Figure 3.3d-f.[4,36] The supercurrent forms a circular loop with a maximum density of $\sim$1 mA/μm2. It gradually decays and approaches zero in the central region of the FTS flake.

3.3.2 London penetration depth Analysis

Extraction of London penetration depth

The length scale that the supercurrents decay inside a superconductor is determined by the London penetration depth λ.[105] Microscopically, λ is associated with the imaginary part of the electrical conductivity and the superfluid density of FTS.[105] Using a machine learning analysis model,[108] we fit the spatial distribution of the microwave field B_{SU} to obtain 2D maps of London penetration depth, as shown in Figure 3.3g-i. Details on the fitting can be found in

Appendix section A.3. The spatial variation of λ within the exfoliated FTS flake demonstrates the existence of superconducting domains possibly induced by inhomogeneities or defects.[89]

Temperature dependence of the extracted London penetration depth

We now discuss the temperature dependence of the extracted London penetration depth of the FTS flake. We start from the general expression of the superfluid density $\rho_s(T) = \lambda(0)^2/\lambda(T)^2$, where $\lambda(0)^2$ and $\lambda(T)^2$ are the London penetration depths at 0 K and at temperature T, respectively. Here, we consider the superfluid density in th emodel of a single superconducting gap Δ. The temperature dependence of Δ is assumed to follow the classical Bardeen-Cooper-Schrieffer (BCS) theory: $\Delta(t) = \Delta(0)\delta(t)$, where $\Delta(0)$ is the superconducting gap at 0 K, $\delta(t) = tanh\left(1.82[1.018(t-1)]^{0.51}\right)$ is the normalized BCS gap,[109] and $t = T_c/T$. The superfluid density ρ_s is given by:[110]

$$\rho_s = 1 - 2\frac{\Delta(0)}{k_B T}\int_0^\infty f(1-f)dy \tag{3.1}$$

where k_B is the Boltzmann constant, $f = [exp(\beta E) + 1]^{-1}$ is the distribution function and $\beta = (k_B T)^{-1}$. The energy of the quasiparticles is given by $E = \sqrt{\varepsilon^2 + \Delta^2(t)}$, where ε is the energy of the normal electrons relative to the Fermi surface and the integration variable is $y = \varepsilon/\Delta(0)$. We fit the temperature dependence of $\lambda(T)$ measured in the central area of the FTS flake using Equation 3.1. $\lambda(0)$ is fitted to be $\approx$400 nm, in agreement with values reported by previous studies.[111] The obtained experimental results of $\lambda(T)$ agrees well with the BCS theory, as shown in Figure 3.4, demonstrating the validity of the London penetration depth obtained by our NV measurements.

3.3.3 Imaging of superconductivity-induced ferromagnetism

In conventional s-wave superconductors, ferromagnetism is usually prohibited because the characteristic spin-singlet s-wave pairing rule dictates antiparallel spin configuration of cooper pairs. Thus, the emergence of superconductivity-induced ferromagnetism is usually

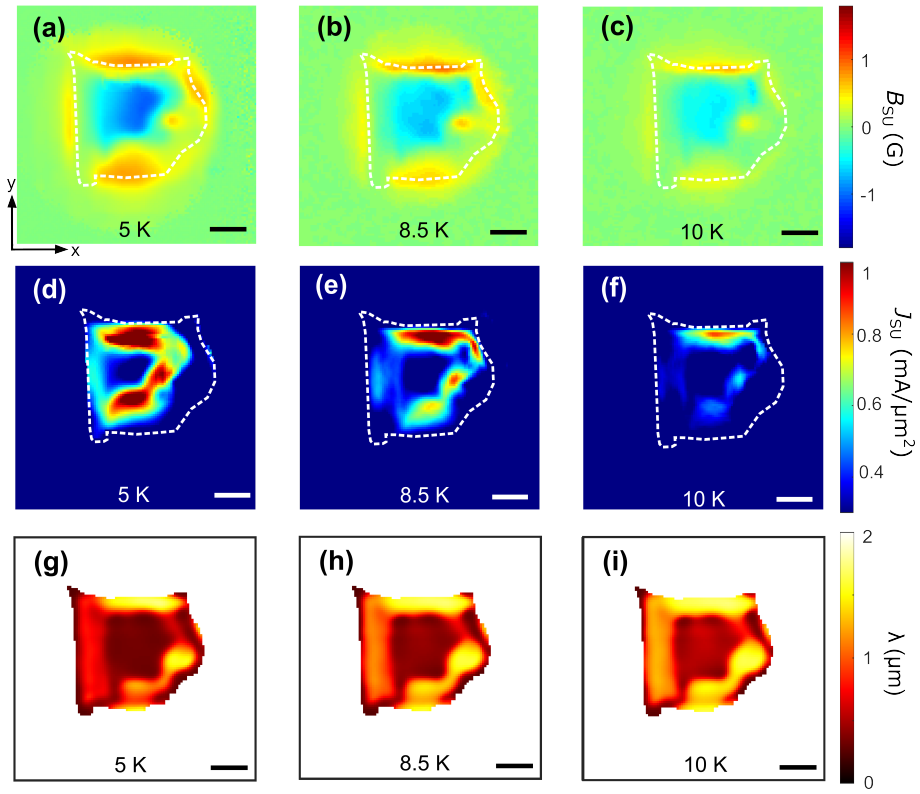

Figure 3.3. NV wide-field imaging of the internal microwave magnetic field, supercurrents, and London penetration depth of an FTS flake. (a-c) Two-dimensional imaging of the internal microwave magnetic field B_{SU} generated by supercurrents in the FTS flake at 5, 8.5, and 12 K. (d-f) Reconstructed spatial distribution of supercurrents in the FTS flake at 5, 8.5, and 12 K. (g-i) Two-dimensional maps of London penetration depth λ reconstructed by machining learning analysis with an assumption of a spatially dependent microwave conductivity. For all panels, the white dashed line marks the boundary of the exfoliated FTS flake and scale bar is 3 μm. This figure is adapted from Ref. [23].

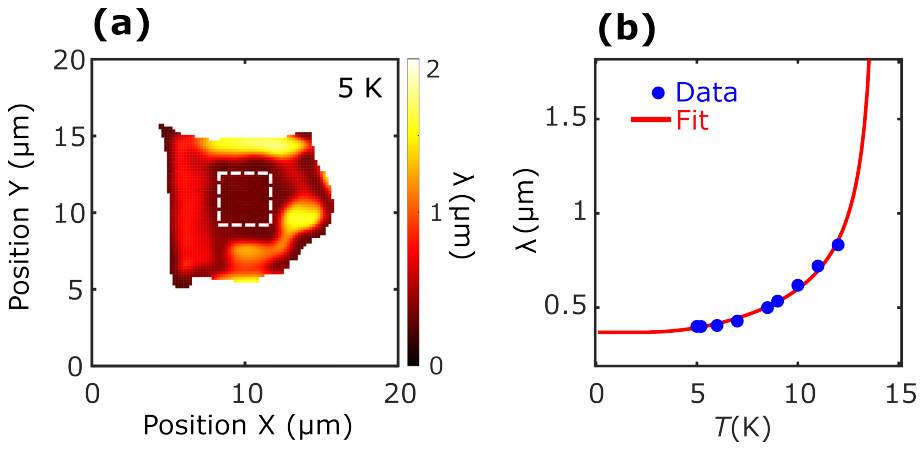

Figure 3.4. Temperature dependence of London penetration depth. (a) 2D map of London penetration depth λ of the FTS flake measured at 5K. The white dashed lines in the center of the flake marks the area of interest. (b) Temperature dependence of the average value of λ obtained at the central area of the flake. The experimental data (blue points) agrees well with the fitting result (red curve) based on Equation 3.1. This figure is adapted from Ref. [23].

accompanied by the spin triplet states or unconventional superconducting pairing symmetries such as experimentally observed in UPt_3,[112] UTe_2,[113] $Ba_1-xKxFe_2As_2$,[114] and recently theoretically predicted in FTS.[95] Next, we employ the NV ODMR technique[13,5,115] to detect magnetic stray fields generated by a superconducting FTS flake, providing direct evidence to the superconductivity-correlated ferromagnetism. Figure 3.5a shows a schematic of our measurement geometry. An external magnetic field B_{ext} ~60 G is applied with an angle of 39° relative to the normal of the sample plane. The in-plane projection of B_{ext} is approximately along the x-axis direction. Note that both supercurrents and magnetization in the FTS flake can potentially produce a sizable stray field. If the superconductivity-correlated ferromagnetism is spontaneously aligned to the direction of the external magnetic field, the out-of-plane component of the stray field generated by a tilted ferro-magnetization is negligibly small in the central area of the FTS flake and exhibits opposite signs at the $+x$ and $-x$ boundaries, as illustrated in Figure

3.5a. In contrast, the out-of-plane component of the internal field generated by supercurrents follows the characteristic Meissner effect, exhibiting a decrease in the center and an increase on the boundary of the FTS flake, as shown in Figure 3.2b. On the basis of these two distinct spatial geometries, we can qualitatively separate these two effects.

The top panel of Figure 3.5b shows the microwave and optical sequence of pulsed NV ODMR measurements. We utilize 1 μs long green laser pulses for NV initialization and readout and 100 ns long microwave π-pulses to induce NV spin transitions. The entire sequence is repeated 15,000 times during one camera exposure period and the frequency f of the microwave pulses is swept for different camera exposure periods. When f matches the NV ESR conditions, reduced photoluminescence is observed. Note that the NV ensemble used in our study has four pairs of ESR transitions in one ODMR spectrum in response to an arbitrary magnetic field, allowing extraction of the out-of-plane component of the internal stray field B_z generated by the FTS flake. Figure 3.5b,f shows the 2D maps of B_z measured at 5 and 12 K, respectively. When $T < T_c$, $B_z = B_{SC} + B_{FM}$, where B_{SC} and B_{FM} represent the out-of-plane static magnetic fields produced by supercurrents and ferromagnetism in the FTS flake, respectively. At 5 K, B_z is dominated by the Meissner screening effect, showing a positive value at the boundary area of the FTS flake and a negative value in the central region. While the contribution of B_{FM} is heavily masked in this situation, the asymmetry of B_z along the x-axis direction indicates the existence of a tilted magnetization in the FTS flake. When T = 12 K in proximity to T_c, the Meissner effect is significantly suppressed due to the reduced supercurrents, thus, the asymmetry of B_z becomes more pronounced. The sign of B_z reverses at the two opposite boundaries of the FTS flake, providing clear evidence to the induced magnetic moment in superconducting FTS.

3.3.4 Machine-learning assisted separation of supercurrents and ferromagnetism induced fields

To quantitatively separate the two mutually entangled effects, we performed machine-learning assisted simulations to reconstruct the spatially dependent magnetic field B_{SC} and B_{FM}.

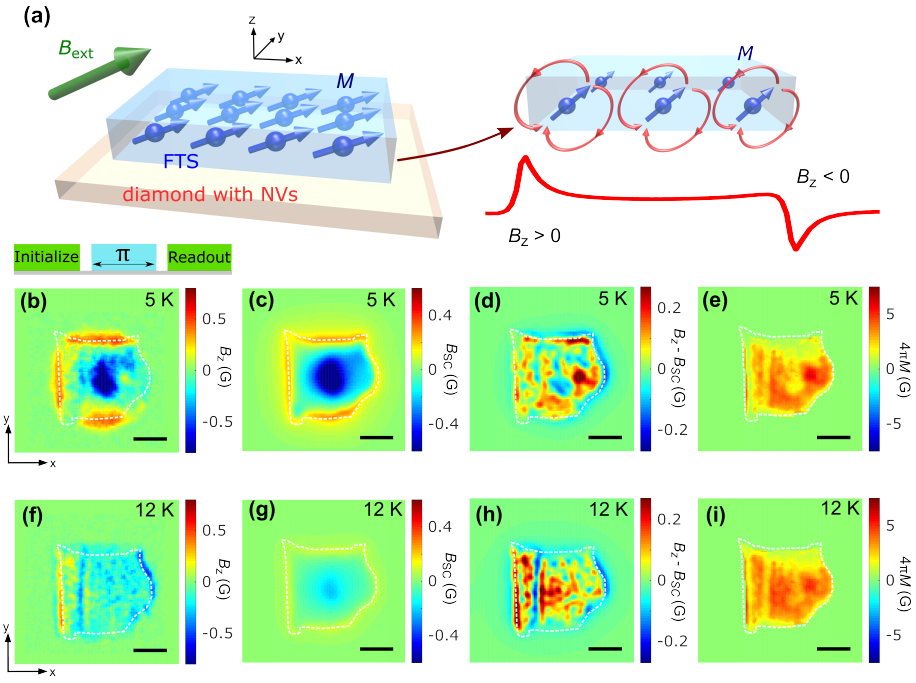

Figure 3.5. NV wide-field imaging of superconductivity-correlated ferromagnetism in FTS. (a) Experimental measurement geometry to detect superconductivity-correlated ferromagnetism in an FTS flake. An external magnetic field B_{ext} is applied to tilt the magnetization away from the equilibrium position (out-of-plane direction, z-axis). The in-plane projection of B_{ext} is approximately along the x-axis direction. The out-of-plane component of the internal DC magnetic field generated by the ferromagnetism shows the sign reversal feature at the $+x$ and $-x$ boundaries of the FTS flake. (b,f) Two-dimensional wide-field imaging of internal magnetic field B_z generated by the FTS flake at 5 K (b) and 12 K (f). (Top panel of b) Optical and microwave sequence of NV ODMR measurements. (c,g) Extracted 2D images of stray field B_{SC} produced by supercurrents at 5 K (c) and 12 K (g). (d,h) Extracted 2D images of stray field (B_z - B_{SC}) generated by the superconductivity-correlated ferromagnetism at 5 K (d) and 12 K (h). (e,i) Reconstructed spatially dependent magnetization of the superconducting FTS flake at 5 K (e) and 12 K (i). For panels (b-i), the white dashed line marks the boundary of the exfoliated FTS flake and scale bar is 3 μm. This figure is adapted from Ref. [23].

In brief, we first fit the measured B_z using the model of the Meissner effect to get the stray field B_{SC} produced by supercurrents (more details on calculation in Appendix section A.4). The remaining part (B_z - B_{SC}) will be fitted to the expression of the stray field B_{FM} produced by the superconductivity-correlated ferromagnetism in FTS (reconstruction details in Appendix section A.1). Figure 3.5c,d,g,h shows the extracted 2D maps of B_{SC} and (B_z - B_{SC}) at 5 and 12 K, respectively. The contribution from the supercurrents (Figures 3.5c,g) largely resembles the Meissner effect and becomes significantly reduced when temperature approaches T_c. The obtained 2D map of (B_z - B_{SC}) follows the "sign reversal" feature at the $+x$ and -x boundaries of the FTS flake, suggesting that the induced magnetic moment follows the direction of the external magnetic field. Note that the screening effect of in-plane magnetic fields by the supercurrents could also lead to an asymmetric magnetic field profile, however, with an opposite sign to a ferromagnet. Thus, such an effect does not play a significant role in our experiments. It is worth mentioning that (B_z - B_{SC}) exhibits a nonuniform distribution, indicating a multidomain structure [Figure 3.5d,h] of the superconductivity-correlated ferromagnetism in the FTS flake, which can be attributable to defects, inhomogeneity, and domain wall pinning effects.[115] When the in-plane component of the external magnetic field B_{ext} is rotated by $\sim$130°, the observed B_{SC} largely remains the same while the field pattern of (B_z - B_{SC}) rotates accordingly, confirming the weak anisotropy of the superconductivity-correlated ferromagnetism whose orientation is tunable by the external magnetic field. On the basis of the spatial-dependent (B_z - B_{SC}), we further reconstructed the 2D profile of the magnetization $4\pi M$ of FTS, as shown in Figure 3.5e,i. The obtained $4\pi M$ exhibits spatially dependent variation with an average value of $\sim$4 G for $T < T_c$. Theoretically, the upper limit of M of superconducting FTS can be estimated by assuming that all the charge carriers are polarized: $M_{max} = \frac{b\mu_B}{V}$, where $b\mu_B$ is the magnetization of each Fe atom, μ_B is the Bohr magneton, and V is the average volume containing one Fe cation. With b = 0.0464 and $V = 1.0 \times 10^{-28}$ m^3,[95] $4\pi M_{max}$ is calculated to be 15 Oe, which is in qualitative agreement with our experimental results. We highlight that the measured spin susceptibility of FTS at 12 K is about 200 times larger than the value measured in the paramagnetic state,

suggesting that the observed magnetic moment cannot be a result of spin polarization induced by the external magnetic field. In addition, we also performed NV measurements of the stray field B_z produced by FTS above T_c. The measured magnetic field falls below our detection limit over entire measurement region at 16 K. All of these results demonstrate that the observed ferromagnetism is indeed driven by the superconductivity in FTS.

3.3.5 Spin relaxometry measurements of spin fluctuations (thermal magnons) in superconducting FTS

In addition to DC stray fields, the superconductivity-correlated ferromagnetism in FTS also generates fluctuating magnetic fields at the characteristic frequencies of thermal magnons. When the frequency of FTS magnons matches the NV ESR frequency, the magnetic fluctuations will induce spin transitions of a proximal NV center, leading to an enhanced NV relaxation rate[34,28]

$$\Gamma_{\pm} = \frac{k_B T}{f_{\pm} h} \int D(f_{\pm}, k) f(k, z_{NV}) dk \tag{3.2}$$

where $f_{\pm}$ and $\Gamma_{\pm}$ are the NV ESR frequencies and NV relaxation rates of $m_s = 0 \leftrightarrow 1$ transitions, respectively, T is the temperature, k_B is the Boltzmann constant, h is the Planck constant, $D(f_{\pm}, k)$ is the magnon spectral density[34], k is the magnon wave vector, z_{NV} is the NV-to-sample distance, and $f(k, z_{NV}$ is the transfer function describing magnon-generated fluctuation magnetic fields at an NV site.[34] Specifically, $D(f_{\pm}, k) = \frac{1}{\pi} \frac{W}{W^2 + [\omega_m(B_{ext}, k) - 2\pi f_{\pm}]^2}$ is modeled as a Lorentzian function centered at the magnon dispersion $\omega_m(B_{ext}, k)$, and W is the width of the magnon modes.[34] For FTS with a small magnetization and magnetic anisotropy, $\omega_m \approx \gamma B_{ext} + \frac{D_s}{\hbar} k^2$, where D_s is the spin stiffness and $\hbar$ is the reduced Planck constant.[116] The transfer function $f(k, z_{NV})$ equals $Ck^3 e^{-2z_{NV}k}$,[34] where C is a constant. The term $k^3 e^{-2z_{NV}k}$ describes the efficiency of an NV center at detecting magnetic fluctuations due to magnons with different wave-vectors. Experimentally, we employ the NV relaxometry method to detect magnetic fluctuations,[34,30] providing another piece of evidence to the superconductivity-correlated ferromagnetism in FTS. Figure 3.6a shows

the schematic of the device structure for NV relaxometry measurements, where a patterned diamond nanobeam (details in section 1.4.1) is transferred onto the surface of an exfoliated FTS flake. Note that the choice of patterned diamond nanobeams instead of NV ensembles is to take advantage of the excellent quantum coherence of single NV spins, which is crucial for detecting low amplitude fluctuating magnetic fields. Figure 3.6c shows a confocal optical image of the prepared device, demonstrating the single-spin addressability of our measurement system. The top panel of Figure 3.6b shows the optical measurement sequence of NV relaxometry (more details on this measurement can be found in section 1.3.3). Figure. 3.6b shows the extracted NV spin relaxation rate Γ_- as a function of the external magnetic field B_{ext} applied along the NV axis measured at 5 K. Notably, Γ_- exhibits a significant variation with B_{ext} and follows the theoretical trend predicted by Equation 3.2, as shown by the red solid line in the bottom panel of Figure 3.6b, which is well correlated to the field-dependent variation of the magnon density of the FTS sample. Figure 3.6d plots the NV ESR frequencies $f_\pm$ and the minimum magnon frequency f_{min} of the TRSB-induced ferromagnetism in FTS as a function of B_{ext}. Here, f_{min} is set to be $\gamma B_{ext}/2\pi$ in approximation due to the weak magnetic moment and negligible anisotropy of the superconductivity-correlated ferromagnetism in FTS as probed by the ODMR experiments. The magnon density of FTS at a given frequency f can be calculated by multiplying the Bose-Einstein distribution function $\frac{1}{exp(\frac{fh}{k_BT})-1}$ by the magnon density of states.[34] At the measurement temperature where $k_BT \gg fh$, the Bose-Einstein distribution function evolves to the Rayleigh-Jeans distribution function $\frac{k_BT}{fh}$ and the magnon density of states is a constant in the 2D limit. Therefore, the magnon density falls off as $1/f$, as indicated by the fading color. The fluctuating magnetic fields generated by FTS is proportional to the magnon density which can be inferred from the measured NV relaxation rate. As B_{ext} increases from zero, the lower branch of the NV ESR frequency f_- decreases and probes the FTS thermal magnons with a higher density, leading to an enhancement of Γ_-, as shown in Figure 3.6b. The peak value of Γ emerges at B_{ext} $\sim$ 450 G, slightly before the crossing point of f_- and f_{min}. When $B_{ext} > 500$ G, f_- lies below the FTS magnon band, leading to a suppression of spin noise and a rapid

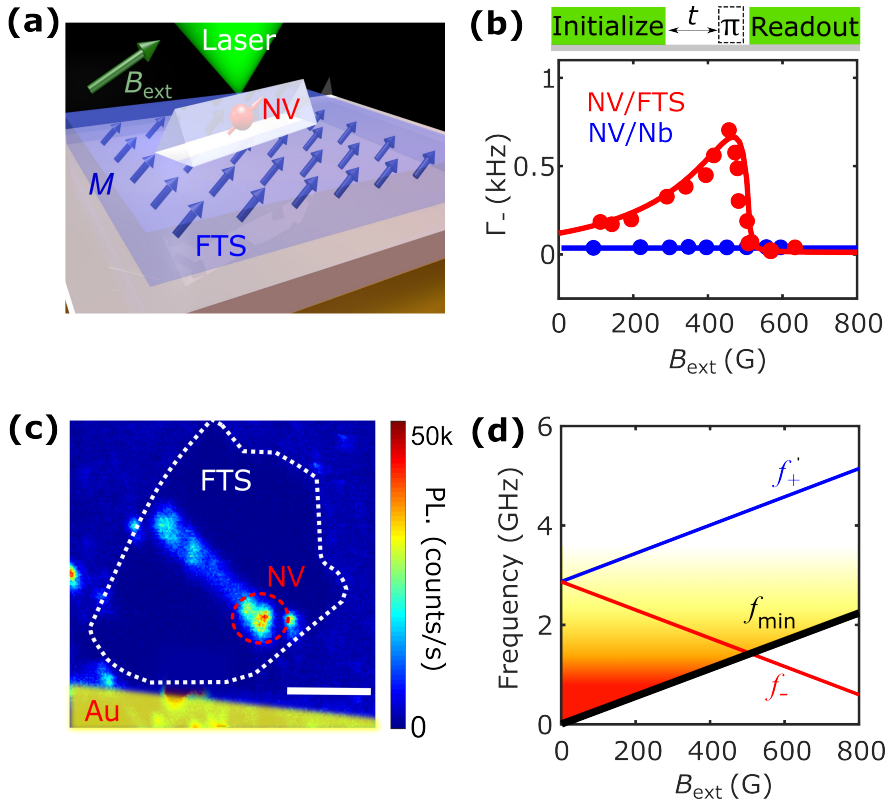

Figure 3.6. NV relaxometry measxurements of intrinsic magnetic fluctuations in superconducting FTS. (a) Schematic of a single NV spin contained in a patterned diamond nanobeam locally probing magnetic fluctuations in an FTS flake. (b) Photoluminescence image showing an individually addressable NV spin positioned on top of an FTS flake. The red dahsed line marks the position of the NV center and the white dashed line indicates the boundary of the FTS flake. Scale bar is 3 μm. (c) Top panel: the optical measurement sequence of NV relaxometry. Bottom panel: field dependent NV relaxation rate Γ_- of an NV center positioned on FTS (red points) and a conventional superconductor Nb (blue points) measured at 5 K. The red solid line is a fitting to Equation 3.2 and the blue solid line is a fitting to a Bardeen-Cooper-Schrieffer (BCS) model.[117,118] (d) Sketch of magnon density of superconductivity-correlated ferromagnetism in FTS and NV ESR frequencies $f_\pm$ as a function of the external magnetic field B_{ext}. The variation of the magnon density is illustrated by the fading color falling with $1/f$ dependence. This figure is adapted from Ref. [23].

decay of the measured NV relaxation rate. The excellent agreement between the experimentally measured NV relaxation rate Γ_- and the theoretical model described by Equation 3.2 further supports the existence of ferromagnetism in superconducting FTS. We highlight that the observed field-dependent variation of NV relaxation rate Γ_- is absent in the control measurement where an NV center is in proximity to a conventional s-wave superconductor Niobium (Nb), demonstrating that the enhanced fluctuating magnetic fields are mainly driven by ferromagnetism in the superconducting FTS flake instead of the spin excitations of quasiparticles.[117,118]

3.4 Physical origin of observed correlation between superconductivity and ferromagnetism

In FTS, the superconducting carriers are electrons and holes near the Fermi level, and localized magnetic moments can be carried by the d orbitals of Fe atoms,[119] impurities, or defects. Because of the weak exchange coupling of carriers at the Fe sites, long-range ferromagnetic ordering is absent in the normal state. When $T < T_c$, TRSB accompanied by unconventional pairing symmetries could take place, leading to the emergence of ferromagnetism in FTS. Because of the multiorbital nature of the Fe atoms,[95] there may exist nearly degenerate gap function symmetries. To reduce the free energy, they often prefer a superposition with a relative $\pm\frac{\pi}{2}$ phase difference in the mean-field theory. The ferromagnetic order is inversion symmetric, hence, it can only be induced by mixing two pairing orders with the same parity. The mixing between A_{1g} and A_{2g} or B_{1g} and B_{2g} can yield the ferromagnetic order along the z-direction. On the other hand, the in-plane component of ferromagnetism could be a consequence of mixing a pairing symmetry of A or B-type with a two-dimensional representation of the E-type.[95]

Loosely speaking, A, B, and E refer to the s, d and p-wave pairing symmetries respectively; the subindices 1 and 2 refer to the parity with respect to the vertical plane reflection; and g means even parity under inversion. Because of the orbital degree of freedom, the E-type pairing symmetry can also be spin-singlet. Such a complex pairing gap function can couple to

the bulk magnetization via spin-orbit coupling according to a symmetry analysis,[95] enabling the establishment of a long-range magnetic order in superconducting FTS. This driving force is due to the TRSB Cooper pairing, whose effect may be weak. Nevertheless, the FTS system contains local moments,[119] and they may be further aligned by the bulk magnetization to amplify such effect.

3.5 Conclusion

In summary, we have demonstrated NV-based quantum sensing and imaging of magnetic flux generated by exfoliated FTS flakes. The obtained spatial profile of stray fields generated by supercurrents in FTS flakes follows the characteristic Meissner screening effect. By employing NV ODMR method, we provide direct evidence of superconductivity-correlated ferromagnetism in FTS, opening up new opportunities for exploring the rich physics related to the interplay among topology, superconductivity, and magnetism in topological superconductors. At the same time, our results also reveal the unconventional pairing mechanism and the time reversal symmetry breaking in FTS, demonstrating NV centers as a versatile local probe to investigate nanoscale electrical and magnetic properties of emergent quantum materials. The observed spatially tunable coupling between NV centers and superconducting FTS also provides a new route for developing hybrid quantum architectures,[120] aiding in the development of next-generation, solid-state-based quantum information technologies.

3.6 Acknowledgements

Chapter 3 is adapted with permission from Nano Lett. 2021, 21, 17, 7277–7283. Copyright 2021 American Chemical Society. The dissertation author was an author of this paper, and coauthors are Hailong Wang, Mengqi Huang, Eric Lee-Wong, Lunhui Hu, Hanyi Lu, Gerald Q. Yan, Genda Gu, Congjun Wu, Yi-Zhuang You, and Chunhui Rita Du

Chapter 4

Quantum Imaging of Magnetic Phase Transitions and Spin Fluctuations in Intrinsic Magnetic Topological Nanoflakes

4.1 Introduction

In this section, we first introduce the family of $MnBi_2Te_4$ $(Bi_2Te_3)_n$ materials. These materials possess nontrivial band topology, tunable magnetism, and extraordinary quantum transport properties, which are only recently being explored. While previous studies have explored bulk properties of these materials, the local magnetic properties of $MnBi_2Te_4$ $(Bi_2Te_3)_n$ remain an open question, hindering a comprehensive understanding of their fundamental material properties. In particular, the interplay between magnetism and band topology must be explored locally, to fully understand the spectrum of exotic behavior present in these materials. These properties include the quantum anomalous Hall effect,[121–126] surface ferromagnetism,[127–131] topological magnetoelectric effect,[132,133] and many others.[134–136] The family of $MnBi_2Te_4$ $(Bi_2Te_3)_n$ materials has emerged as a particularly attractive platform for exploring topologically dictated quantum spin and charge transport behaviors at relatively high temperatures.[124,137–146] The discovery and understanding of these emergent material properties of two-dimensional (2D) $MnBi_2Te_4$ $(Bi_2Te_3)_n$ materials relies on concurrent developments in theory, material synthesis, and sensitive metrology tools capable of characterizing local magnetic properties at the nanoscale,

which remains a formidable challenge given the current state of the art. The major difficulty results from the significantly reduced magnetic flux generated by the weak or nearly compensated magnetic moment of 2D $MnBi_2Te_4$ $(Bi_2Te_3)_n$ samples, which is beyond the detection limit of most conventional magnetometry techniques. While some methods such as magneto-optic-Kerr-effect microscopy,[147] reflective magnetic circular dichroism,[137] and Raman spectroscopy[138,139] could be employed to qualitatively diagnose the magnetic states of 2D $MnBi_2Te_4$ $(Bi_2Te_3)_n$ flakes, these techniques provide limited quantitative information about local magnetization, and the field sensitivity of these tools is often compromised by interference effects and constrained by the optical diffraction limit. Exploiting nitrogen-vacancy (NV) centers in diamond, we explore nanoscale quantum imaging of the magnetic phase transitions and spin fluctuations in exfoliated $MnBi_4Te_7$ flakes, revealing the underlying spin transport physics and magnetic domains at the nanoscale.

4.2 Measurement platform

To these problems we apply NV centers to perform nanoscale quantum imaging of $MnBi_4Te_7$ nanoflakes. By performing spatially resolved NV wide-field magnetometry measurements,[35,23,4,36] we directly image the local magnetization of $MnBi_4Te_7$ nanoflakes and the characteristic multidomain evolution behavior in a first-order magnetic transition process. Using NV relaxometry methods,[103,30,29,3,34] we have observed spatially varied dynamic magnetic fluctuations in $MnBi_4Te_7$, revealing the underlying spin transport physics and the low-frequency spin dynamics hosted by domain walls in these magnetic materials. We expect that the presented NV quantum sensing platform can be readily extended to a large family of layered van der Waals crystals,[5,115,148] providing ample opportunities for investigating the local spin dynamics and transport behaviors in a broad range of quantum materials.[34,149–151]

Figure 4.1a shows a schematic of our measurement platform, in which a [111] oriented diamond sample[37] containing shallowly implanted NV ensembles is used for the quantum

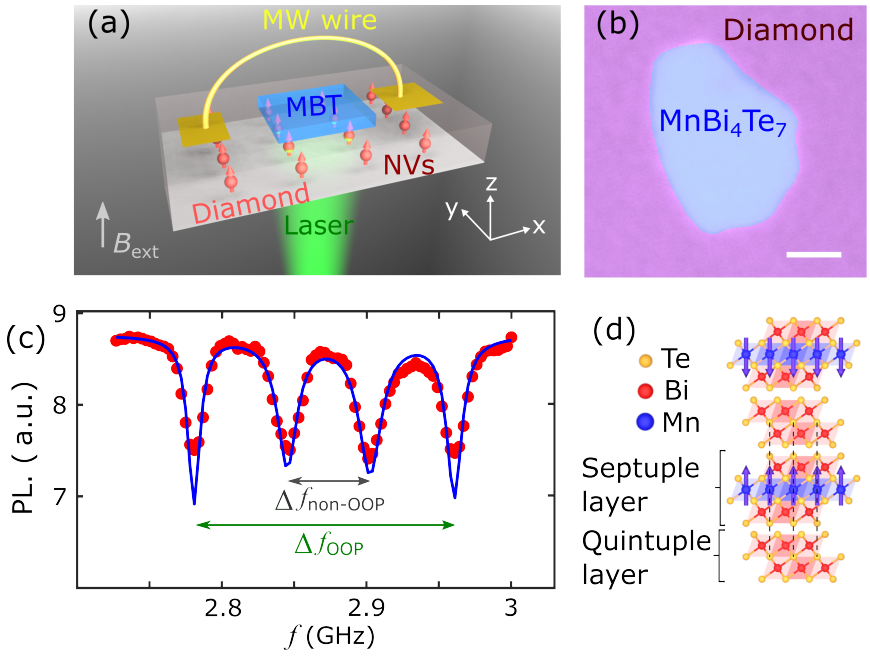

Figure 4.1. (a) Schematic of an exfoliated $MnBi_4Te_7$ flake transferred onto a [111] oriented diamond membrane for nitrogen-vacancy (NV) wide-field magnetometry measurements. (b) Optical image of a prepared diamond-$MnBi_4Te_7$ device. (c) Optically detected magnetic resonance spectrum of NV centers contained in [111] oriented diamond with an external field B_{ext} applied along the out-of-plane (OOP) direction. The experimental spectrum is comprised of two pairs of resonance peaks corresponding to the Zeeman splitting of NV spins with OOP orientation and NV spins aligned along other directions (non-OOP). (c) Schematic of the crystal and magnetic structures of $MnBi_4Te_7$. The scale bar is 4 μm in panel (b). This figure is adapted from Ref. [27].

sensing measurements. Note that one of the four possible NV orientations is along the out-of-plane direction (z-axis), serving as an ideal local sensor to investigate the magnetic dynamics and phase transition of $MnBi_4Te_7$ with spontaneous perpendicular anisotropy. We measure spatially resolved magnetic features of $MnBi_4Te_7$ using our widefield microscope system, more details of which are in Appendix section A.7.1. An 83 nm thick exfoliated $MnBi_4Te_7$ flake with lateral dimensions of approximately $\sim 10 \times 14\ \mu m^2$ is transferred onto the diamond surface, as shown in Figure 4.1b. These single crystals of $MnBi_4Te_7$ were grown using the self-flux method[152], and transferred via the standard polydimethylsiloxane (PDMS) stamp process.[153] techniques onto the surface of the diamond (more details in section 1.4.2. Figure 4.1d illustrates the crystal and magnetic structure of $MnBi_4Te_7$, where the magnetic septuple layer ($MnBi_2Te_4$) and the nonmagnetic quintuple layer (Bi_2Te_3) stack alternately.[152] In the magnetic ground state, below the Néel temperature of 13 K, moments carried by the Mn^{2+} ions in individual septuple layers align parallel with each other, along the out-of-plane direction due to the dominant intralayer ferromagnetic exchange interaction. Neighboring septuple layers are antiferromagnetically coupled, but can be driven into a ferromagnetic configuration by applying a sufficiently strong external perpendicular magnetic field B_{ext}.

4.3 Field-driven antiferromagnetic-to-ferromagnetic phase transition of $MnBi_4Te_7$

We first image the field-driven antiferromagnetic-to-ferromagnetic phase transition of the exfoliated $MnBi_4Te_7$ flake using our NV spin sensors. Figure 4.1c shows an example of the measured NV ESR spectrum, which exhibits two pairs of Zeeman split NV spin energy levels. The outer pair corresponds to NV centers with the out-of-plane (OOP) orientation, whereas the inner pair is degenerate and corresponds to NV centers with axes along the other three possible directions.[37] The magnitude of the local static magnetic field B_{tot} can be extracted as $B_{tot} = \frac{\pi \Delta f_{OOP}}{\tilde{\gamma}}$, where Δf_{OOP} characterizes the Zeeman splitting of the OOP-oriented NVs,

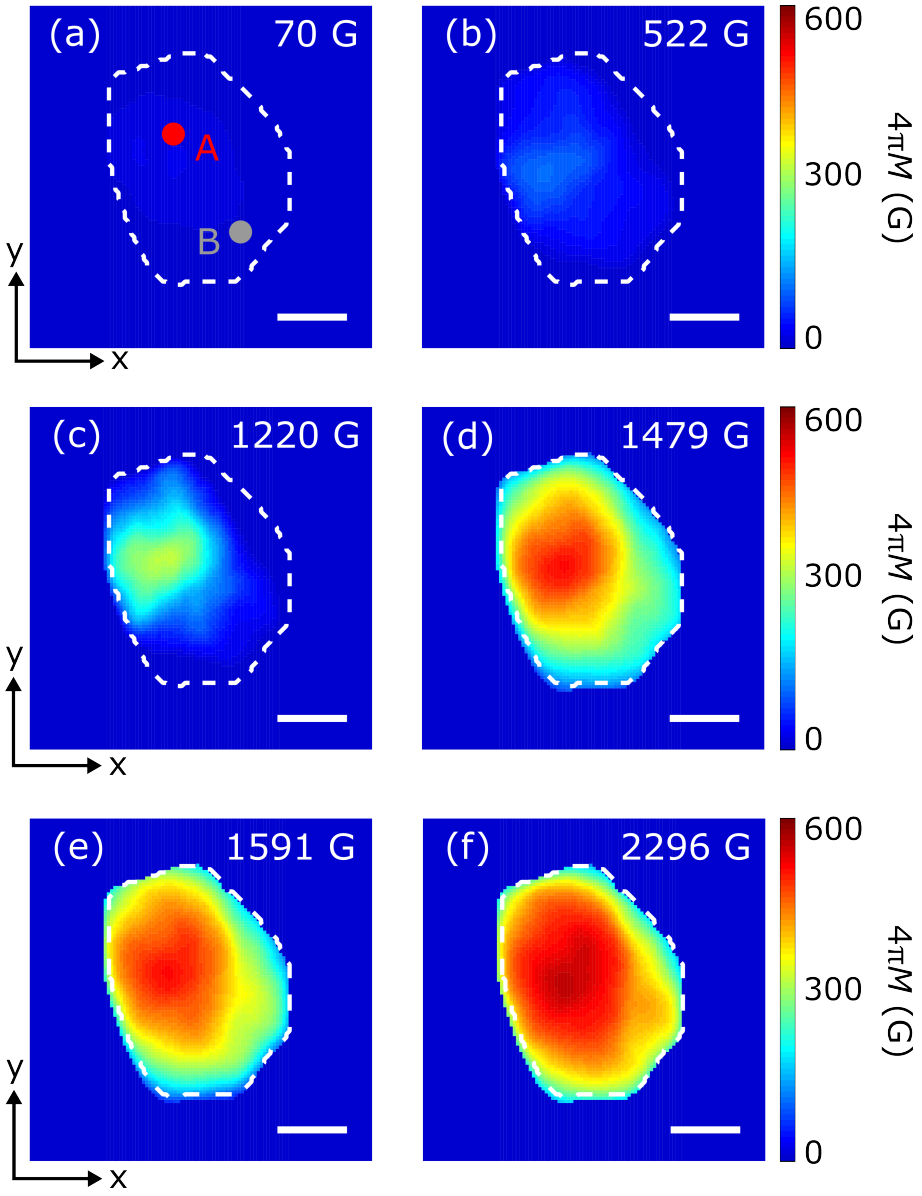

Figure 4.2. (a-f) Reconstructed magnetization ($4\pi M$) maps of an $MnBi_4Te_7$ flake measured at 4.5 K and B_{ext} = 70 G (a), 522 G (b), 1220 G (c), 1479 G (d), 1591 G (e), and 2296 G (f), respectively. The white dashed lines mark the boundary of the exfoliated flake, and the scale bar is 4 μm. This figure is adapted from Ref. [27].

and $\tilde{\gamma}$ is the gyromagnetic ratio of the NV centers. Subtracting the contribution from the external magnetic field B_{ext}, the magnetic stray field B_M generated from the $MnBi_4Te_7$ flake can be quantitatively measured. By performing spatially dependent optically detected magnetic resonance (ODMR) measurements over the NV ensembles, we can obtain a 2D stray field map. Through established reverse-propagation protocols[5,23], expanded on in Appendix section A.1, the corresponding magnetization ($4\pi M$) map of the exfoliated $MnBi_4Te_7$ flake can be quantitatively extracted.

To directly image the first-order magnetic phase transition, Figure 4.2a-f presents the obtained 2D magnetization maps of the $MnBi_4Te_7$ flake measured with an increasing perpendicular magnetic field B_{ext}. In the low-field regime ($B_{ext} < 1000$ G), the exfoliated $MnBi_4Te_7$ flake exhibits a vanishingly small net magnetic moment, as shown in Figure 4.2a,b, due to the antiferromagnetic coupling between the neighboring magnetic septuple layers. A finite magnetic moment shown in the top left region of the flake results from field induced polarization. When B_{ext} increases to 1220 G, the characteristic spin flip transition propagates from the top left area of the flake, leading to a "partial" ferromagnetic state with enhanced local magnetization. Such a "partial" ferromagnetic phase features a coexistence of ferromagnetic and antiferromagnetic ordering of septuple layers along the out-of-plane direction due to the weak interlayer exchange coupling. Note that the remaining area of the $MnBi_4Te_7$ flake stays in the antiferromagnetic ground state with the formation of incipient magnetic domain walls at locations with the lowest energy barrier, as shown in Figure 4.2c. The observed spin flip transition expands to the entire $MnBi_4Te_7$ flake through domain wall propagation with increasing perpendicular field [Figure 4.2d,e] and the local magnetization further increases as the individual magnetic septuple layers become fully aligned. When $B_{ext} >$2000 G, this magnetic phase transition concludes with a saturated local magnetization, as shown in Figure 4.2f. The variation of the local magnetization of the $MnBi_4Te_7$ flake may result from inhomogeneities,[154] magnetic domains,[147,155] and localized defects.[156] The presented results highlight a spatially nonuniform spin flip transition process of the 2D $MnBi_4Te_7$ flake at the nanoscale, exhibiting magnetic domain nucleation and domain

wall propagation behaviors.

4.4 Spatially resolved magnetization dynamics

We now apply our NV wide-field techniques to directly measure dynamic magnetic fluctuations in an exfoliated $MnBi_4Te_7$ flake, from which the underlying spin transport physics and the low-frequency spin dynamics hosted by magnetic domain walls in this magnetic topological material can be revealed. In the next section the theoretical background of this procedure will be described in detail.

4.4.1 Theoretical calculations of spin-wave dispersion of $MnBi_4Te_7$

A complete understanding of the expected spin-wave dispersion of our samples is essential to fully understand our experimental results. Figure 4.3a shows the spin-wave dispersion of bulk $MnBi_4Te_7$. At thermal equilibrium, fluctuations of the transverse and longitudinal spin density of $MnBi_4Te_7$ generate fluctuating stray fields, as illustrated in Figure 4.3b. We derive the dispersion of these fluctuations by considering the Zeeman effect, antiferromagnetic interaction between neighboring layers A and B, ferromagnetic interaction within each layer, and the anisotropy energy to write the Hamiltonian of $MnBi_4Te_7$ as:

$$H = -J_F \left(\sum_{\langle i,i' \in A \rangle} S_i \cdot S_{i'} + \sum_{\langle j,j' \in B \rangle} S_j \cdot S_{j'} \right) + J_A \sum_{\langle i \in A, j \in B \rangle} S_i \cdot S_j - K \sum_l \left(S_l^z\right)^2 - h_B \sum_l S_l^z, \quad (4.1)$$

where J_A and J_F characterize the antiferromagnetic and ferromagnetic exchange constants, respectively, K is the anisotropy constant, $h_B = \mu_B g B_{ext}$ is the Zeeman splitting term, μ_B is Bohr magneton, g is the Landé factor, and B_{ext} is the external magnetic field applied along z axis. Supposing the ground state has spins all up on the sublattice A and all down on the sublattice B, we can invoke the Holstein-Primakoff transformation:

$$
\begin{aligned}
&i \in A : S_i^+ = \sqrt{2S - n_i a_i}, \quad S_i^- = a_i^\dagger \sqrt{2S - n_i}, \quad S_i^z = S - n_i, \qquad n_i = a_i^\dagger a_i, \\
&j \in B : S_j^+ = b_j^\dagger \sqrt{2S - n_j}, \quad S_j^- = \sqrt{2S - n_j b_j}, \quad S_j^z = -S + n_j, \quad n_j = b_j^\dagger b_j.
\end{aligned} \tag{4.2}
$$

The quadratic part of the Hamiltonian is:

$$
\begin{aligned}
H = & -SJ_F \left[\sum_{\langle i,i' \in A \rangle} \left(a_i a_{i'}^\dagger + a_i^\dagger a_{i'} \right) + \sum_{\langle j,j' \in B \rangle} \left(b_j^\dagger b_{j'} + a_i a_{i'}^\dagger \right) \right] \\
& + SJ_A \sum_{\langle i \in A, j \in B \rangle} \left(a_i b_j + a_i^\dagger b_j^\dagger \right) \\
& + \left(z_F SJ_F + z_A SJ_A + 2SK + h_B \right) \sum_{i \in A} a_i^\dagger a_i \left(z_F SJ_F + z_A SJ_A + 2SK - h_B \right) \sum_{j \in B} b_j^\dagger b_j \\
& - \frac{NS^2}{2} \left(z_F J_F + z_A J_A + 2K \right),
\end{aligned} \tag{4.3}
$$

where $z_F = 6$ and $z_A = 2$ are the intralayer and interlayer coordinate numbers, S is the spin quantum number of $MnBi_4Te_7$, and N is the total number of lattice sites. Next, we perform a Fourier transform for the annihilation operator:

$$
a_k = \sqrt{\frac{2}{N}} \sum_{i \in A} e^{-ik \cdot r_i} a_i, b_k = \sqrt{\frac{2}{N}} \sum_{j \in A} e^{-ik \cdot r_j} b_j \tag{4.4}
$$

and the Boboliubov transformation:

$$
\alpha_k = u_k a_k - v_k b_{-k}^\dagger, \beta_k = u_k b_k - v_k a_{-k}^\dagger \tag{4.5}
$$

where $\alpha_k^\dagger, \alpha_k, \beta_k^\dagger, \beta_k$ are the magnon creation and annihilation operators and the transformation coefficients satisfying the condition: $v_{-k} = v_k, u_{-k} = u_k$ and $u_k^2 - v_k^2 = 1$. Through this transformation, the Hamiltonian can be further expressed in a diagonal form:

$$H = \sum_k \omega_{\alpha k} \alpha_k^\dagger \alpha_k + \omega_{\beta k} \beta_k^\dagger \beta_k \tag{4.6}$$

Two spin wave eigen-modes of $MnBi_4Te_7$ are given by:

$$\omega_{\alpha k} = \omega_k + h_B, \omega_{\beta k} = \omega_k - h_B \tag{4.7}$$

and

$$\omega_k = S\sqrt{\left(6J_F\left(1-\gamma_k^F\right)+2J_A+2K\right)^2 - \left(J_A\gamma_k^A\right)^2}, \tag{4.8}$$

where $\gamma_k^A = 2\cos k_z c_{MBT}$, and $\gamma_k^F = (1/3)\left[\cos k_x a_{MBT} + 2\cos\left(k_x a_{MBT}/2\right)\cos\left(\sqrt{3}k_y a_{MBT}/2\right)\right]$. a_{MBT} is the in-plane lattice constant of individual magnetic septuple layers and c_{MBT} characterizes the distance between neighboring magnetic septuple layers. Substituting the relevant material parameters: S = 5/2, $K \sim 9.5$ GHz, $J_F \sim 168$ GHz and $J_A \sim 0.84$ GHz, we are able to plot the spin wave dispersion of $MnBi_4Te_7$ at B_{ext} = 70 G, as shown in Figure 4.3a, and magnon gap is calculated to be 51 GHz. Microscopically, the transverse spin fluctuations vanish below the magnon band minimum and are related to single magnon processes.[34,25] The longitudinal spin fluctuations are related to two-magnon processes,[29,150,151] where a magnon with frequency f is scattered to another one with frequency $f \pm f_{2m}$, emitting (absorbing) magnetic noise at frequency f_{2m}.

4.4.2 Inferring spin diffusion constant and longitudinal magnetic susceptibility of $MnBi_4Te_7$ from nitrogen vacancy relaxometry measurements

In this section, we provide a detailed method to extract the spin diffusion constant D and the static uniform longitudinal magnetic susceptibility χ_0 from the measured NV relaxometry results. An exfoliated $MnBi_4Te_7$ flake has been transferred on a diamond substrate lying in the x-y plane. For simplicity, we consider the $MnBi_4Te_7$ flake as consisting of intermediately stacked septuple layers, and spin transport in each magnetic septuple layer can be treated independently

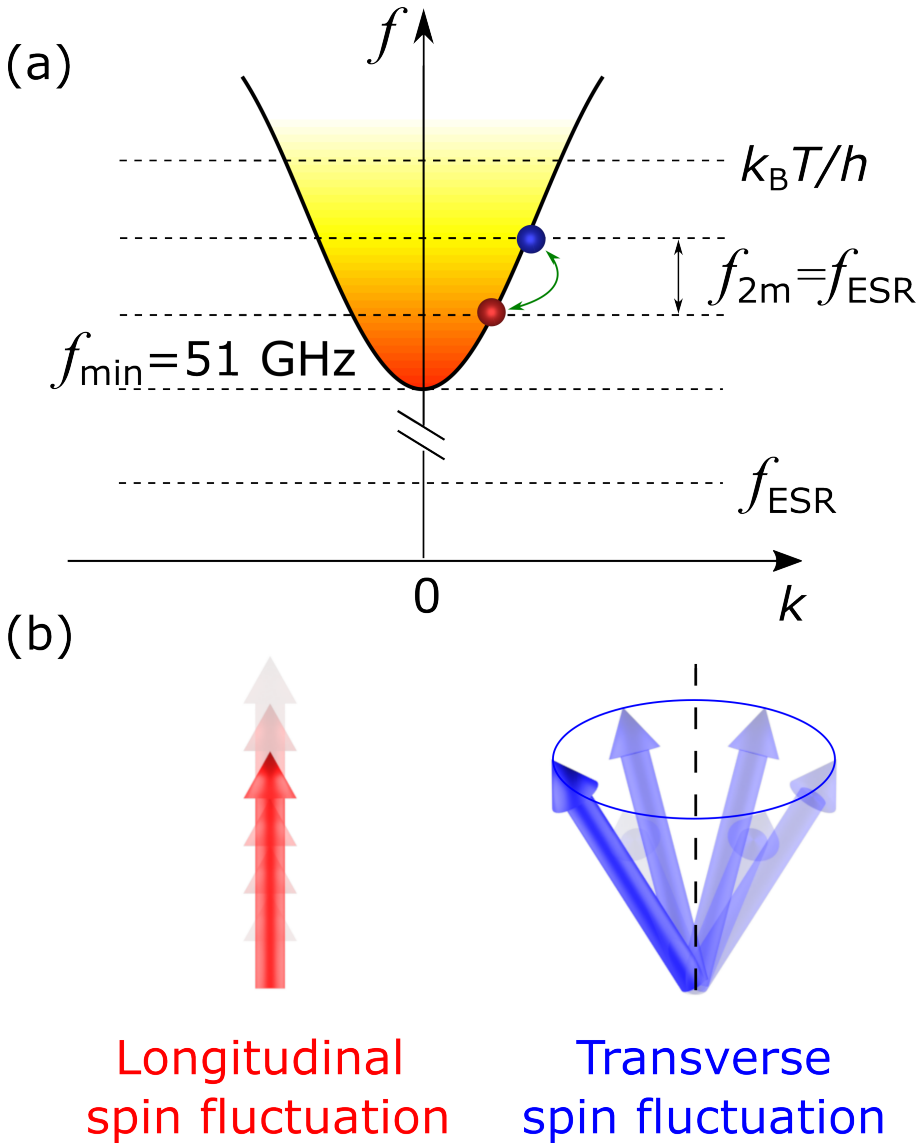

Figure 4.3. (a) Sketch of the magnon dispersion of bulk $MnBi_4Te_7$. The magnon occupation follows the Bose-Einstein distribution as indicated by the fading colors. The minimal magnon frequency f_{min} is ~51 GHz, which is much larger than the NV electron spin resonance frequencies f_{ESR} in our measured field range. The longitudinal spin fluctuations with a characteristic frequency of f_{2m} are associated with two-magnon scattering processes and couple with a NV center through dipolar interactions. (b) Schematic of the dynamic fluctuations of the longitudinal and transverse spin density. This figure is adapted from Ref. [27].

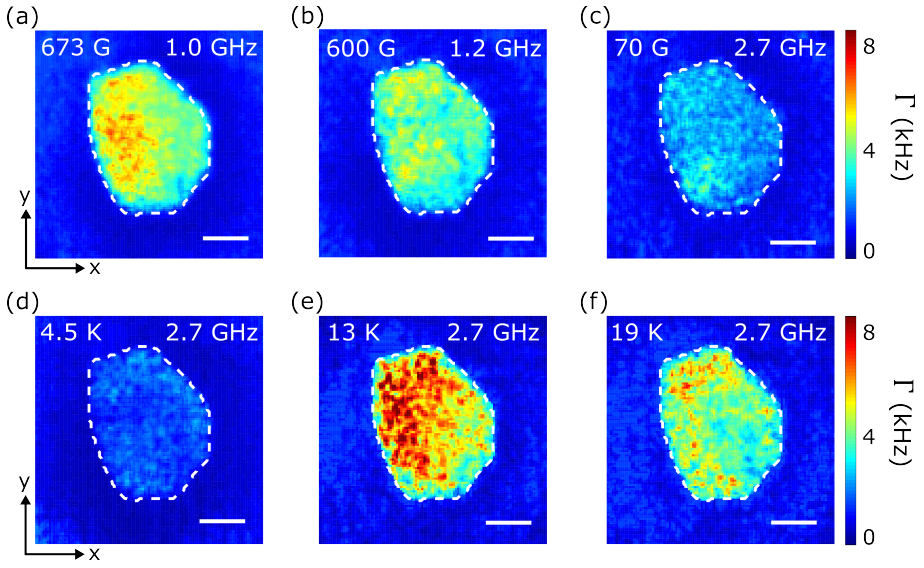

Figure 4.4. (a-c) NV spin relaxation maps measured at f_{ESR} of 1.0 GHz (a), 1.2 GHz (b), and 2.7 GHz (c) at 8.5 K. Top panel of (a): optical and microwave sequence of NV relaxometry measurements. (d-f) NV spin relaxation maps measured at 4.5 K (d), 13 K (e), and 19 K (f) with f_{ESR} = 2.7 GHz. The white dashed lines mark the boundary of the exfoliated flake, and scale bar is 4 μm in panels (a-f). This figure is adapted from Ref. [27].

due to the weak interlayer coupling. Within each layer, the dynamics of the spin density can be described by a two-dimensional diffusion equation at length scales larger than the magnon mean-free path.

The measured NV relaxation rate driven by longitudinal spin fluctuations at the NV ESR frequency f_{ESR} is related by the fluctuation-dissipation theorem to the dynamic spin susceptibility χ'' of the $MnBi_4Te_7$ sample and the NV transfer function in the high temperature limit as follows[150,151]

$$\Gamma(f_{ESR}) = \frac{(\gamma\tilde{\gamma})^2 k_B T}{2\pi f_{ESR}} \int \mathscr{F}(\mathbf{k},d)\chi''(\mathbf{k},d)d\mathbf{k} + \Gamma^0 \tag{4.9}$$

where the first term on the right represents the NV relaxation rate Γ^M induced by spin dynamics of the $MnBi_4Te_7$ flake and Γ^0 is the intrinsic NV relaxation rate that is independent of the spin dynamics of $MnBi_4Te_7$. γ and $\tilde{\gamma}$ are the gyromagnetic ratio of the magnetic sample and NV centers, k_B is the Boltzmann constant, T is temperature, k is the magnon wavevector, $\mathscr{F}(k,d)$ is the transfer function[28] describing the magnetic fields generated at the NV site, and d is the NV-to-sample distance. The dynamic spin susceptibility χ'' reflects underlying spin transport properties of a magnetic sample, which can be expressed as a function of the intrinsic spin diffusion constant D and the static longitudinal magnetic susceptibility per layer χ_0 via the conventional diffusion equation[151,157]. We treat spin transport independently in each magnetic septuple layer due to weak interlayer coupling. By doing this, we can use the two-dimensional diffusion equation at length scales larger than the magnon mean-free path. Assuming U(1) symmetry, the diffusion equation for spin density along the direction of the order parameter s^z can be written:

$$\partial_t s^z + \nabla \cdot \mathbf{j}_s = -\frac{1}{\tau_s}(s^z - \chi H). \tag{4.10}$$

Here, we have introduced the spin-relaxation time τ_s and the spin current $\mathbf{j}_s = -\sigma\nabla\mu$, where σ is the spin conductivity, $\mu = \chi^{-1}s^z - H$ is the spin chemical potential, χ is the static uniform

longitudinal spin susceptibility, and H is an external perturbation thermodynamically conjugate to the spin density. By introducing diffusion coefficient $D = \sigma/\chi$, we can get:

$$\partial_t s^z - D\nabla^2 s^z + D\chi\nabla^2 H = -\frac{1}{\tau_s}\left(s^z - \chi H\right). \tag{4.11}$$

By introducing the Fourier transform $s^z(\mathbf{k}, f) = \int e^{i\mathbf{k}\cdot\mathbf{r} - 2\pi f} s^z(\mathbf{r}, t)\, d^2\mathbf{r}dt$, we have:

$$s^z(\mathbf{k}, f) = \frac{\chi\left(Dk^2 + 1/\tau_s\right)}{(2\pi i f) + \left(Dk^2 + 1/\tau_s\right)} H. \tag{4.12}$$

Thus, the imaginary part of the dynamical longitudinal spin susceptibility can be written as:

$$\chi''(k, f) = \frac{2\pi\chi\left(Dk^2 + 1/\tau_s\right) f}{(2\pi f)^2 + \left(Dk^2 + 1/\tau_s\right)^2}. \tag{4.13}$$

In the rest of the section, we first show each septuple layer's contribution to the relaxation rate and then sum them up to get the total relaxation rate. The spin wave gap for $MnBi_4Te_7$ is about 51 GHz, which is much larger than the NV ESR frequency in our experiments. Therefore, only the longitudinal spin fluctuation s^z along the magnetic order parameter direction (z) will contribute to the NV relaxation. Note that $MnBi_4Te_7$ consists of alternatively stacked magnetic septuple layers and non-magnetic quintuple layers and only the spin fluctuations in septuple layers will drive the NV relaxation. The contribution to the NV relaxation by individual magnetic septuple layers can be expressed as:

$$\Gamma^M(z, f) = \frac{1}{2\pi f B} G(\theta) \int dk k^3 e^{-2kz} \chi''(k, f), \tag{4.14}$$

where $\beta = 1/k_B T$, k_B is the Boltzmann constant, T is the temperature, and θ is the angle between the NV axis and out-of-plane direction. The geometric factor $G(\theta)$ can be expressed as:

$$G(\theta) = \frac{\left(\gamma\tilde{\gamma}\right)^2 \pi}{2}\left(5 - \cos 2\theta\right). \tag{4.15}$$

where $\tilde{\gamma}$ and γ are the gyromagnetic ratio of the NV spin and $MnBi_4Te_7$ flake. The total NV relaxation rate generated from all magnetic septuple layers can be expressed as:

$$\begin{aligned}\Gamma^M(f) &= \sum_i \Gamma^M(z_i, f) \\ &= \frac{G(\theta)}{2\pi f \beta} \int_0^\infty \left(\frac{1}{c_{MBT}} \int_d^{d+t_{MBT}} dz e^{-2kz} \chi''(k,f) \right),\end{aligned} \tag{4.16}$$

where t_{MBT} the thickness of the $MnBi_4Te_7$ flake, d is the distance between NV center and the sample surface, and c_{MBT} characterizes the distance between neighboring magnetic septuple layers. Combined with Eq. 4.13, the NV relaxation rate can be expressed as:

$$\Gamma^M(f) = \frac{G(\theta)}{2\beta c_{MBT}} \int_0^\infty dk k^2 \left[e^{-2kd} - e^{-2k(d+t_{MBT}} \right] \frac{\left(Dk^2 + 1/\tau_s\right)\chi}{(2\pi f)^2 + \left(Dk^2 + 1/\tau_s\right)^2}. \tag{4.17}$$

In the limit of slow relaxation $\tau_s \to \infty$, Eq. 4.17 can be approximated as:

$$\Gamma^M(f) = \frac{G(\theta)}{2\beta c_{MBT}} \int_0^\infty dk k^2 \left[e^{-2kd} - e^{-2k(d+t_{MBT}} \right] \frac{\left(Dk^2\right)\chi}{(2\pi f)^2 + \left(Dk^2\right)^2}. \tag{4.18}$$

From the frequency dependent noise, we can extract the longitudinal magnetic susceptibility per layer $\chi_0 = \gamma^2 \chi$ and the spin diffusion constant at certain temperatures. Qualitatively, the induced NV relaxation rate is higher (lower) at a lower (higher) ESR frequency, corresponding to a smaller (larger) energy difference invoked in the two-magnon process[151,150]. By fitting the individual points of the measured 2D NV relaxation maps to Eq. 4.18, we obtain spatially dependent spin diffusion constant D and magnetic susceptibility χ_0 of the exfoliated $MnBi_4Te_7$ flake.

From the frequency dependent noise, we can extract the longitudinal magnetic susceptibility per layer $\chi_0 = \gamma^2 \chi$ and the spin diffusion constant at certain temperatures. The gapless longitudinal spin noise spectrum can be calculated based on Eq. 4.18. Qualitatively, the induced NV relaxation rate is higher (lower) at a lower (higher) ESR frequency, corresponding to a

smaller (larger) energy difference invoked in the two-magnon process[151,150]. By fitting the presented results to Eq. 4.18, the intrinsic spin diffusion constants of $MnBi_4Te_7$ is obtained to be $(5.4 \pm 0.7) \times 10^{-6}$ m^2/s. The magnetic susceptibility per layer χ_0 is extracted to be $(52.3 \pm 3.2) \times 10^{-4}$ nm. This number can be converted into $(87.3 \pm 5.3) \times 10^{-2}$ emu·mol^{-1}·Oe^{-1}, in agreement with previous studies on bulk $MnBi_4Te_7$ crystals[152]. Lastly, by fitting the individual points of the measured 2D NV relaxation maps to Eq. 4.18, we obtain spatially dependent spin diffusion constant D and magnetic susceptibility χ_0 of the exfoliated $MnBi_4Te_7$ flake.

4.5 Spin dynamics measurement results

We note present the experimental results of using NV relaxometry techniques to detect the fluctuating magnetic fields generated by spin fluctuations in the $MnBi_4Te_7$ flake. The top panel of Figure 1.4b shows the optical and microwave measurement sequence. A green laser pulse first initializes the NV spin to the $m_s = 0$ state. Spin fluctuations in the $MnBi_4Te_7$ sample couple to proximate NV centers through the dipole-dipole interaction. Fluctuating magnetic fields at the NV ESR frequencies induce NV spin transitions from the $m_s = 0$ to the $m_s = \pm 1$ states, leading to an enhancement of the NV relaxation rate Γ.[103,30,29,3,34] After a delay time t, we measure the occupation probabilities of the NV spin in the $m_s = 0$ and the $m_s = \pm 1$ states by applying a microwave π-pulse at the corresponding ESR frequencies and measuring the spin-dependent photoluminescence via a green-laser readout pulse.[25] By measuring the integrated photoluminescence intensity as a function of the delay time t and fitting the data with a three-level model,[34,28] the NV relaxation rates can be quantitatively obtained (more details in Appendix section A.5). We highlight that in the low-field regime with a quasi-uniform magnetic domain structure, the NV ESR frequencies in our measurements are much lower than the minimum magnon energy of $MnBi_4Te_7$. Thus, the measured NV relaxation is driven primarily by longitudinal spin fluctuations. In contrast, in the high-field regime where multidomains form during the spin flip transition of $MnBi_4Te_7$, the magnetic noise generated by the low-frequency

spin dynamics hosted by magnetic domain walls[3,158] also plays a role.

4.5.1 Low-field regime

We focus our NV relaxometry measurements in the low-field regime to detect the longitudinal spin fluctuations of the $MnBi_4Te_7$ nanoflake. Figure 4.4a-c shows the 2D maps of the measured NV relaxation rate at 8.5 K at ESR frequencies of 1.0, 1.2, and 2.7 GHz, respectively. The applied perpendicular magnetic field B_{ext} is below 800 G to ensure a quasi-single magnetic domain feature of the sample. Notably, the measured NV spin relaxation rate Γ is significantly enhanced in the diamond area covered by the $MnBi_4Te_7$ flake. The magnitude of Γ decreases with increasing NV ESR frequency, suggesting that a larger energy difference invoked in the two-magnon process discussed above suppresses longitudinal spin fluctuations, in qualitative agreement with our theoretical model.[150,151]Figure 4.4d-f shows the 2D NV relaxation maps measured at an ESR frequency of 2.7 GHz at 4.5, 13, and 19 K, respectively. When T = 4.5 K, the magnetic fluctuations are suppressed due to the reduced thermal magnon energy, leading to negligible NV spin relaxation. Notably, we observed significantly enhanced longitudinal spin fluctuations at a temperature of 13 K, which is expected due to the increase in the magnetic susceptibility of $MnBi_4Te_7$ around the Néel temperature T_N.[152] When T = 19 K, longitudinal spin fluctuations remain, which is attributed to the finite spin-spin correlation in the paramagnetic state.[159] The observed spatially varying magnetic fluctuations over the exfoliated $MnBi_4Te_7$ flake could be induced by inhomogeneities in magnetic susceptibility, spin diffusion constant, and exchange coupling strength.

By measuring the NV relaxation rate as a function of ESR frequency, we can extract the key material parameters D and χ_0 of the $MnBi_4Te_7$ flake. Figure 4.5a plots a three-dimensional map of the spatially averaged NV relaxation rates Γ^M of the flake as a function of ESR frequency and temperature. The variation of the NV relaxation rate agrees well with the theoretical model of Equation 4.9 from which the intrinsic spin diffusion constant D and the static longitudinal magnetic susceptibility χ_0 of $MnBi_4Te_7$ at individual temperatures can be extracted, as presented

in Figure 4.5b-c. D is obtained to be $(6.1 \pm 0.8) \times 10^{-6}$ m/s^2 at 4.5 K, in qualitative agreement with the theoretical estimation of $D = v^2\tau/2$ [160] when taking the magnon velocity to be $v \approx 1$ km/s [152] and the momentum scattering time $\tau \approx 10$ ps. Below the Néel temperature ($\sim$13 K) of $MnBi_4Te_7$, D monotonically decreases as the temperature increases due to a reduction of τ caused by enhanced Umklapp scattering. [161] When $T > 14$ K, D decays to an approximately constant value and the residual spin transport capability results from atomic scale thermal spin fluctuations. The obtained static magnetic susceptibility χ_0 generally agrees with previous measurements of bulk $MnBi_4Te_7$ samples. [152] As shown in Figure 4.4c, χ_0 reaches a peak value of $(9.9 \pm 0.6) \times 10^{-3}$ nm around the Néel temperature of $MnBi_4Te_7$, which is consistent with the antiferromagnetic phase transition. [152]Figure 4.5d,e shows the obtained 2D maps of spin diffusion constant D and static magnetic susceptibility χ_0 of the exfoliated $MnBi_4Te_7$ flake, respectively, measured at 8.5 K. Note that the enhanced χ_0 in the top left region of the flake is consistent with the observed larger field-induced magnetic moment, as shown in Figure 4.2a,b.

4.5.2 High-field regime

Next, we move to the high-field regime to image spin fluctuations generated by magnetic domain walls in an $MnBi_4Te_7$ flake during the spin flip transition. In magnetic topological materials, domain walls serve as intrinsic boundaries between two topological states with opposite chiralities. [135,162] Because the Chern number must change discontinuously across neighboring magnetic domains, chiral edge states are expected to reside along domain walls, offering an attractive platform to realize and engineer exotic quantum spin and charge transport behaviors. [135,162]Figure 4.6a illustrates the evolution of magnetic phases of $MnBi_4Te_7$ as a function of increasing perpendicular magnetic field B_{ext}. In the antiferromagnetic and ferromagnetic states, the magnetization of each septuple layer is uniformly aligned and the bulk spin excitation energy of $MnBi_4Te_7$ is larger than the NV ESR frequencies in the accessible magnetic field range due to the large magnetic anisotropy. In this case, the NV-magnon coupling is mediated by longitudinal spin fluctuations as discussed above. During the spin flip transition, spins in individual septuple

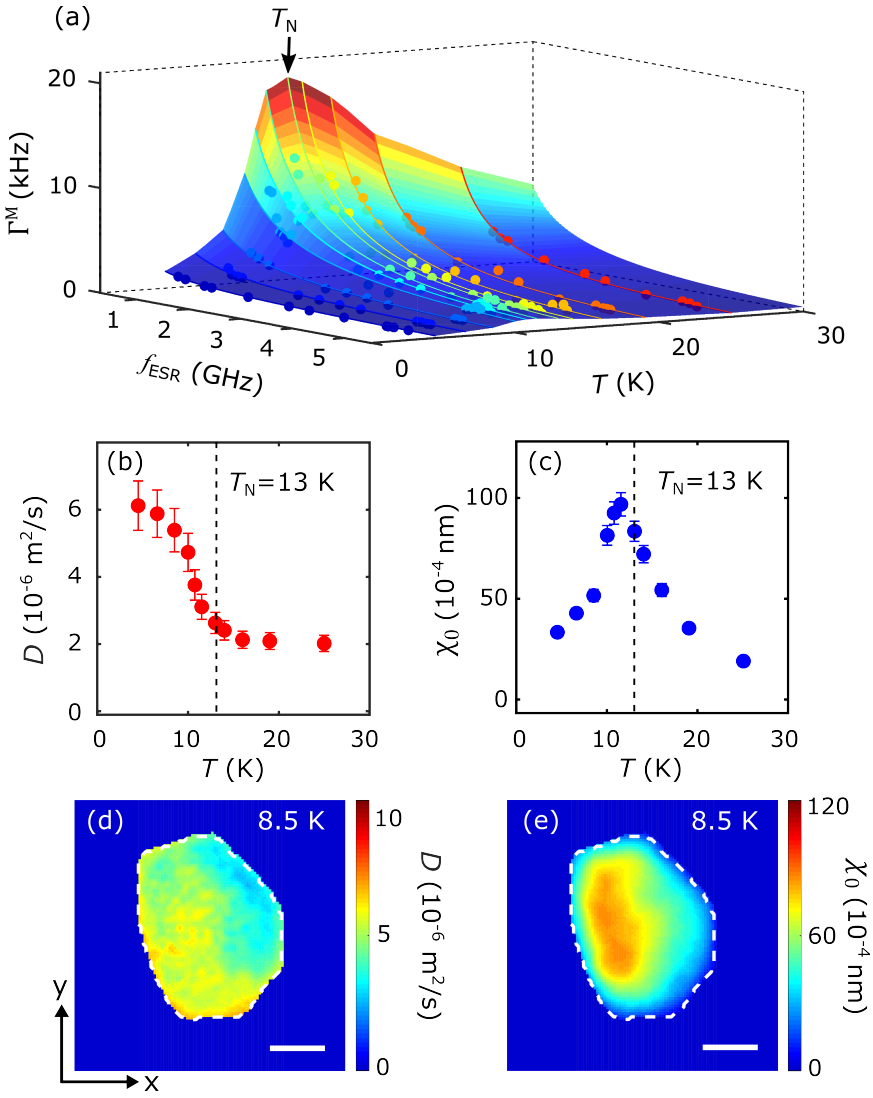

Figure 4.5. (a) NV relaxation rates Γ^M measured as a function of temperature and the NV electron spin resonance frequency f_{ESR}, from which the spin diffusion constant and magnetic susceptibility per layer can be extracted. The solid lines are fitting curves to the theoretical calculation. (b) Intrinsic spin diffusion constant D measured as a function of temperature. (c) Temperature dependence of the obtained longitudinal static magnetic susceptibility χ_0. (d,e) Two-dimensional images of D and χ_0 of the $MnBi_4Te_7$ flake at 8.5 K. The white dashed lines mark the boundary of the exfoliated flake, and the scale bar is 4 μm. This figure is adapted from Ref. [27].

layers may flip mostly independently due to weak interlayer coupling. Nucleation of domain walls occurs at locations within of an exfoliated $MnBi_4Te_7$ flake where the energy barrier is the lowest and form partially magnetically flipped septuple layers, as illustrated in the middle panel of Figure 4.6a. The low-frequency spin dynamics hosted by magnetic domain walls will generate fluctuating magnetic stray fields,[3,158] driving NV relaxation at the corresponding ESR energy.

Figure 4.6b-d shows NV wide-field static magnetization images of the $MnBi_4Te_7$ flake measured at 1311, 1442, and 2340 G, respectively. An applied perpendicular magnetic field B_{ext} induces the formation of magnetic domains during the spin flip transition [Figure 4.6b,c]. Figure 4.6e-g shows 2D maps of the NV relaxation rate measured at the corresponding magnetic fields. Note that the background of the NV relaxation rate induced by longitudinal spin noise generated from bulk spin excitations has been subtracted to highlight the contribution Γ^D from the spin fluctuations in magnetic domain walls. When B_{ext} = 1311 G, the top-left corner of the $MnBi_4Te_7$ flake becomes polarized while the rest of the sample remains partially magnetically flipped. This is accompanied by the formation of lateral magnetic domain walls that generate significantly enhanced magnetic noise. Note that the flipped area of the $MnBi_4Te_7$ flake expands when increasing B_{ext} to 1422 G and suppresses the NV relaxation rate, as shown in Figure 4.6f. When B_{ext} = 2340 G, $MnBi_4Te_7$ enters the fully saturated ferromagnetic state shown in Figure 4.6d, and generates a vanishingly small spin noise Γ^D due to the absence of magnetic domain walls.

4.6 Estimation of magnetic domain wall density from the lateral magnetization gradient of the $MnBi_4Te_7$ flake

Qualitatively, the measured NV relaxation rate increases with the domain wall density, which is further related to the gradient of the magnetization. In this section, we provide a qualitative estimation of the domain wall density from the lateral magnetization gradient of the exfoliated $MnBi_4Te_7$ flake. To exclude the contribution of the intrinsic spatial inhomogeneity, the

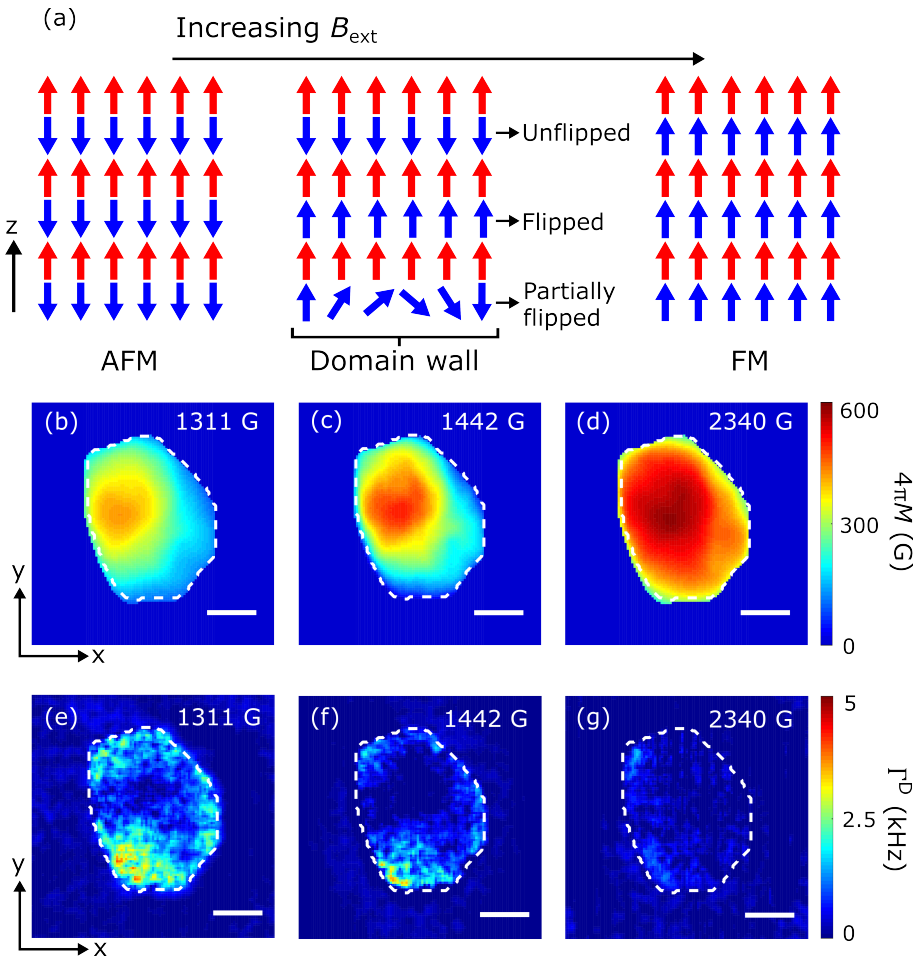

Figure 4.6. (a) Schematic of the evolution of the magnetic states of $MnBi_4Te_7$ as a function of increasing perpendicular magnetic field B_{ext}. In the ferromagnetic and antiferromagnetic phases, the magnetic moments of individual magnetic septuple layers are fully aligned parallel or antiparallel without the formation of magnetic domains. During the spin flip transition process, spins in individual septuple layers could flip mostly independently. Magnetic domain walls nucleate at locations where the energy barrier is lowest, leading to a magnetic gradient in the lateral direction of a partially flipped septuple layer. (b-d) Reconstructed magnetization maps of the $MnBi_4Te_7$ flake measured at B_{ext} of 1311 G (b), 1442 G (c), and 2340 G (d). (e-g) Magnetic domain wall-induced NV spin relaxation maps measured at the corresponding magnetic fields. The longitudinal spin noise generated from the bulk spin excitations has been subtracted to highlight the contribution Γ^D from the magnetic domain walls. The white dashed lines mark the boundary of the exfoliated flake, and the scale bar is 4 μm in panels (b-g). This figure is adapted from Ref. [27].

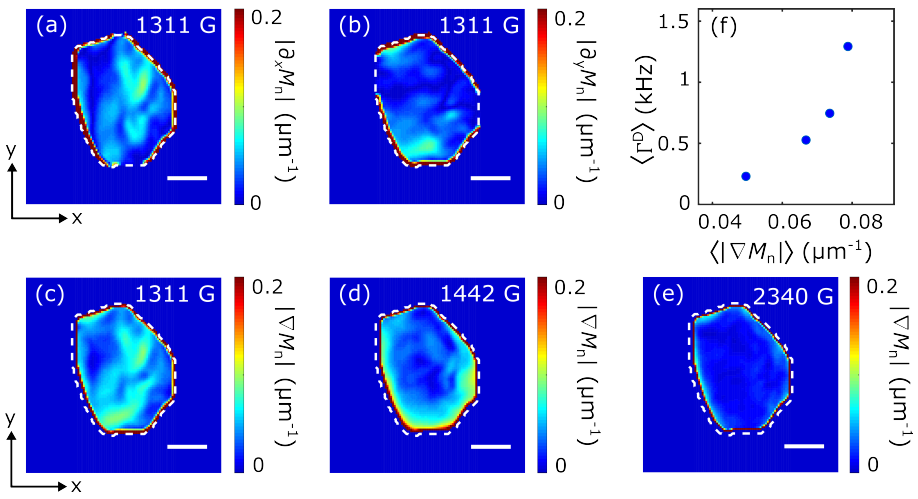

Figure 4.7. Calculation of lateral magnetization gradient of an $MnBi_4Te_7$ flake. (a)-(b) 2D maps of the x component (a) and y component (b) of the gradient vector of normalized magnetization maps of an $MnBi_4Te_7$ flake measured at B_{ext} = 1311 G and T = 4.5 K. (c)-(e) 2D maps of the magnitude of the gradient vector $|\nabla M_n|$ of normalized magnetization measured at three perpendicular magnetic fields: 1311 G (c), 1442 G (d), and 2340 G (e). The measurement temperature is T = 4.5 K. (f) Spatially averaged spin noise $\langle\Gamma^D\rangle$ across the exfoliated $MnBi_4Te_7$ flake area plotted as a function of the spatially averaged gradient of the normalized magnetization $\langle|\nabla M_n|\rangle$. For Figures 4.7a-4.7e, the white dashed lines mark the boundary of the exfoliated flake, and the scale bar is 4 μm. This figure is adapted from Ref. [27].

2D magnetization $M(B_{ext})$ maps at a given field are first normalized to the saturated magnetization M_s measured at B_{ext} = 2580 G. A built-in gradient function in MATLAB is used to individually extract the x and y components of the gradient vector of the normalized 2D magnetization map $M_n = M(B_{ext})/M_s$, as shown in Figures 4.7a and 4.7b. The two components $\partial_x M_n$ and $\partial_y M_n$ are combined to calculate the magnitude of the gradient vector:$|\nabla M_n| = \sqrt{(\partial_x M_n)^2 + (\partial_y M_n)^2}$. Figures 4.7c-4.7e show the obtained 2D images of $|\nabla M_n|$ at B_{ext} = 1311 G, B_{ext} = 1442 G, and B_{ext} = 2340 G, respectively. Notably, the obtained magnetic gradient monotonically decreases with increasing perpendicular magnetic field from 1311 G to 2340 G. Because the domain wall density is largely proportional to the magnetic gradient, we expect dramatically suppressed

magnetic noise generated by domain walls in the $MnBi_4Te_7$ flake (from 1311 G to 2340 G), which is in agreement with the measured NV relaxation maps shown in Figures 4.6e-4.6g in the manuscript. Figure 4.7f plots the averaged magnetic noise $\langle \Gamma^D \rangle$ measured across the $MnBi_4Te_7$ flake area as a function of the spatially averaged magnetic gradient $\langle |\nabla M_n| \rangle$. The magnitude of the measured spin noise qualitatively increases with the magnetic gradient, suggesting that the formed magnetic domain walls indeed play a dominant role in generating the extra fluctuating magnetic fields leading to the observed NV spin relaxation.

4.7 Comparison to family of $MnBi_2Te_4$ $(Bi_2Te_3)_n$ materials

To reveal the underlying spin transport mechanism in the magnetic topological material $MnBi_2Te_4$ $(Bi_2Te_3)_n$ family, we extend the demonstrated NV wide-field relaxometry platform to $MnBi_2Te_4$ and $MnBi_8Te_{13}$. Figures 4.8a-4.8c show schematics of the material structure of $MnBi_2Te_4$, $MnBi_2Te_4$, and $MnBi_8Te_{13}$, respectively. In $MnBi_2Te_4$, magnetic septuple layers directly stack on each other without the insertion of the nonmagnetic quintuple layer (Figure 4.8a). The higher-order magnetic topological compounds $MnBi_4Te_7$ and $MnBi_8Te_{13}$ feature an increasing number of the intercalating quintuple layers [163], as illustrated in Figures 4.8b and 4.8c. By changing the spacing between neighboring magnetic septuple layers, the interlayer coupling strength of $MnBi_2Te_4$ $(Bi_2Te_3)_n$ systematically varies, while the intralayer coupling strength remains largely the same [145]. Figures 4.8d-4.8f present the 2D maps of spin diffusion constant of the exfoliated $MnBi_2Te_4$, $MnBi_4Te_7$, and $MnBi_8Te_{13}$ flakes measured at 8.5 K, respectively. Despite the difference in the shape of the flakes and defect-induced inhomogeneities,
the spatially averaged spin diffusion constants of the three $MnBi_2Te_4$ $(Bi_2Te_3)_n$ samples show notable consistency, which are $(5.7 \pm 0.6) \times$ 10-6 m/s2, $(5.4 \pm 0.7) \times 10^{-6}$ m/s^2, and $(5.4 \pm 0.4) \times 10^{-6}$ m/s^2, respectively, suggesting a common mechanism underlying the intrinsic spin transport in this magnetic material family. Microscopically, the spin diffusion process describes the random Brownian motion of a thermally populated magnon gas with a velocity v governed

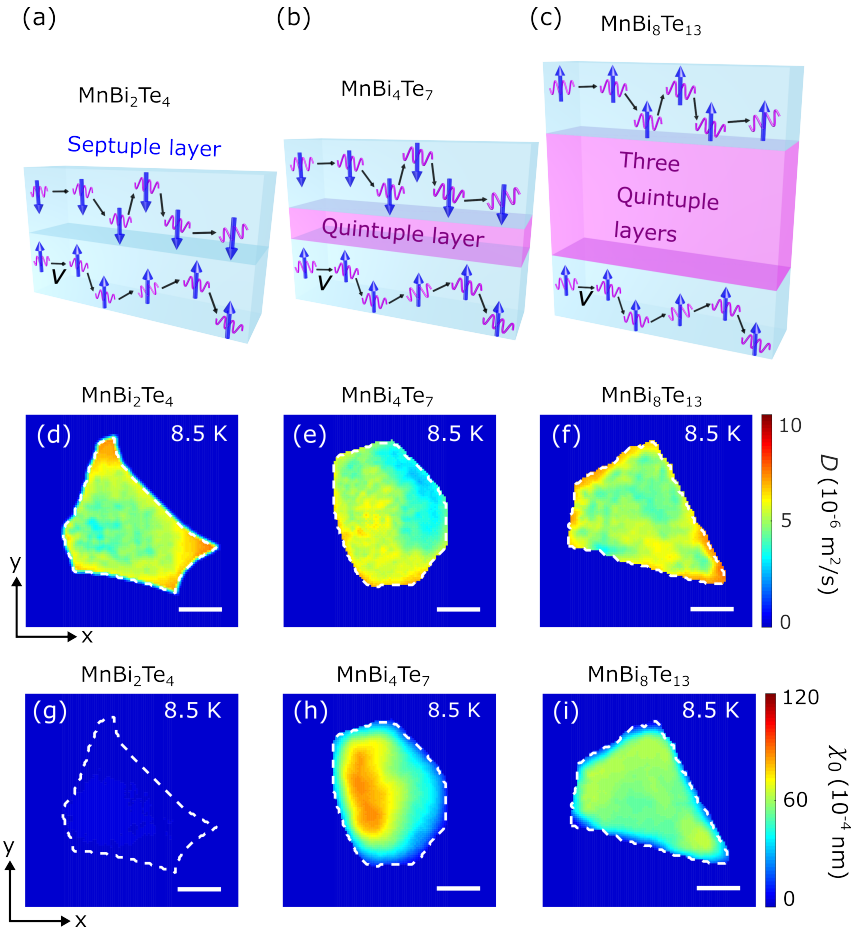

Figure 4.8. Intralayer exchange coupling driven spin diffusion in the family of $MnBi_2Te_4$ $(Bi_2Te_3)_n$ materials. (a)-(c) Schematics of the material structure of $MnBi_2Te_4$ (a), $MnBi_4Te_7$ (b), and $MnBi_8Te_{13}$ (c) consisting of alternately stacked nonmagnetic quintuple layers and magnetic septuple layers. Spin diffusive transport is driven by spin-conserved scattering of a thermally populated magnon gas with a characteristic velocity v that is dominated by the intralayer exchange interaction. Blue arrows represent the spin carried by magnons (denoted by purple waves) in magnetic septuple layers. The spatially random trajectory of the spin (denoted by the black arrows) represents the exchange-dominated spin scattering process. (d)-(f) 2D maps of the obtained spin diffusion constant of exfoliated $MnBi_2Te_4$ (d), $MnBi_4Te_7$ (e), and $MnBi_8Te_{13}$ (f) flakes measured at 8.5 K. (g)-(i) 2D maps of the magnetic susceptibility χ_0 of exfoliated $MnBi_2Te_4$ (d), $MnBi_4Te_7$ (e), and $MnBi_8Te_{13}$ (f) flakes also measured at 8.5 K. The white dashed lines mark the boundary of the exfoliated flakes, and the scale bar is 4 μm. This figure is adapted from Ref. [27].

by the exchange energy. The intrinsic spin diffusion constant is determined by: $D = v^2\tau/2$[160], where $v \sim (J_s a)/\hbar$ (J_s is the exchange coupling strength, a is the lattice constant, and $\hbar$ is the reduced Planck constant) and τ is the momentum relaxation time. The minimal variation of the obtained D of $MnBi_2Te_4$, $MnBi_4Te_7$, and $MnBi_8Te_{13}$ flakes indicates that spin diffusion in $MnBi_2Te_4$ $(Bi_2Te_3)_n$ family is mainly driven by the intralayer exchange interaction while the role of the interlayer coupling is secondary. Intuitively, we expect that spin transport in $MnBi_2Te_4$ $(Bi_2Te_3)_n$ is largely confined in individual magnetic septuple layers and the effect of interlayer spin diffusion is negligible, as illustrated in Figures 4.8a-4.8c.

Using the method discussed in section 4.4.2, we further obtain the spatially dependent magnetic susceptibility χ_0 of the exfoliated $MnBi_2Te_4$ $(Bi_2Te_3)_n$ flakes, as shown in Figures 4.8g-4.8i. χ_0 is extracted to be $(3.4 \pm 0.1) \times 10^{-4}$ nm, $(52.3 \pm 3.2) \times 10^{-4}$ nm, and $(47.8 \pm 0.8) \times 10^{-4}$ nm for $MnBi_2Te_4$, $MnBi_4Te_7$, and $MnBi_8Te_{13}$, respectively. These parameters can be converted into $(3.3 \pm 0.1) \times 10^{-2}$, $(87.3 \pm 5.3) \times 10^{-2}$, and $(152.3 \pm 2.6) \times 10^{-2}$ emu·mol^{-1}·Oe^{-1}, in agreement with previous studies on bulk $MnBi_2Te_4$ $(Bi_2Te_3)_n$ crystals[152]. The significantly larger χ_0 of $MnBi_4Te_7$ and $MnBi_8Te_{13}$ in comparison with that of $MnBi_2Te_4$ could be partially attributed to the vicinity of the magnetic transition point (10.5 K and 13 K) to the measurement temperature (8.5 K).

4.8 Conclusion

Direct imaging of magnetic domain walls in intrinsic magnetic topological materials could provide an opportunity to investigate the interplay between local magnetization and macroscopic quantum transport behaviors, for example, the high-temperature quantum anomalous Hall effect[124–126,136] and layer Hall effect[138] recently discovered in $MnBi_2Te_4$ $(Bi_2Te_3)_n$. The spatial resolution of the presented NV wide-field imaging technique lies at the optical diffraction limit of ~500 nm. By employing scanning NV microscopy methods,[5,13,3,115] we expect the spatial resolution to ultimately reach the tens of nanometers regime, offering new opportunities to

uncover detailed microscopic features of magnetic patterns in quantum materials.

In summary, we have used NV centers as a nanoscale local probe to investigate magnetic phase transitions and spin fluctuations in magnetic topological materials. The spatially resolved NV magnetometry measurements reveal characteristic domain wall nucleation and propagation features during the spin flip transition of $MnBi_4Te_7$ flakes. By employing NV relaxometry techniques, we access the longitudinal spin fluctuations in $MnBi_4Te_7$, from which the intrinsic spin diffusion constant and static magnetic susceptibility are obtained. We also observe a dramatic increase of magnetic noise arising from magnetic domain walls in an $MnBi_4Te_7$ flake, which is attributed to low-frequency spin fluctuations hosted by spatially evolving magnetic textures. Because magnetic domain walls and spin fluctuations are fundamentally related to mesoscopic spin and charge transport in topological materials, nanoscale imaging of relevant material parameters will contribute to a comprehensive understanding of the exotic properties of the family of $MnBi_2Te_4$ $(Bi_2Te_3)_n$ materials. Our results further illustrate the capabilities of NV centers in probing the nanoscale spin transport and dynamics in emergent condensed matter systems, opening new possibilities for investigating the interplay between magnetism and topology in a broad range of low-dimensional materials. The dynamic coupling between topological materials and NV spin qubits may also point to the possibility of developing NV-based hybrid architectures for next-generation quantum information sciences and technologies.[158]

4.9 Acknowledgements

Chapter 4 is adapted with permission from Nano Lett. 2022, 22, 14, 5810–5817. Copyright 2022 American Chemical Society. The dissertation author was an author of this paper, and coauthors are Chaowei Hu, Mengqi Huang, Shu Zhang, Hanyi Lu, Gerald Q. Yan, Hailong Wang, Yaroslav Tserkovnyak, Ni Ni, and and Chunhui Rita Du

Chapter 5

Local control of a single nitrogen-vacancy center by nanoscale engineered magnetic domain wall motion

5.1 Introduction

Effective control and readout of qubits form the technical foundation of next-generation, transformative quantum information sciences and technologies. While optical strategies, as described in previous chapters, have proven to be effective, they are limiting in terms of high scalability. Here, we report magnetic domain wall motion driven local control and measurements of NV spin properties. By engineering the local magnetic field environment of an NV center via nanoscale reconfigurable domain wall motions, we show that NV photoluminescence, spin level energies, and coherence time can be reliably controlled and correlated to the magneto-transport response of a magnetic device. Our results highlight the electrically tunable dipole interaction between NV centers and nanoscale magnetic structures, providing an attractive platform to realize interactive information transfer between spin qubits and non-volatile magnetic memory in hybrid quantum spintronic systems.

Hybrid quantum structures consisting of state-of-the-art qubits and electronic devices have received immense research interest recently due to their potential for developing next-generation, transformative information technologies.[164,7,165,166] Nitrogen-vacancy (NV) centers

and magnetic domain walls hosted by solid-state memory devices[167–171,158,172] stand out as two promising candidates for use in practical devices. As discussed previously, NV centers provide an attractive platform to develop cutting-edge quantum sensing,[12] network,[173,8] and computing technologies.[7–10,174,175] On another front, magnetic domain walls in thin films, which sustain nanoscale spatially evolving and reconfigurable spin textures, promise to deliver a wide range of novel functionalities to modern spintronic devices.[171,176–179] Examples include high-speed domain wall-based logic gates,[168,170,180] magnetic racetrack memory,[167,180] long-range, energy-efficient spin transport,[181–183] and many others.[184,185] More recently, magnetic domain walls have been theoretically predicted to enable entanglement between distant spin qubits through dipole-dipole interactions.[158,172] Despite enormous promise to date, integration of magnetic domain walls with NV centers to realize effective transfer and readout of information encoded in quantum entities and magnetic memory devices remains elusive. One of the major technical challenges involves establishing nanoscale proximity between NV centers and magnetic domain walls in a controllable and reconfigurable way. Here, we show our efforts along this direction. By utilizing NV quantum sensing technologies,[5,13,3,186,36,187] we achieve nanoscale imaging of spin-orbit-torque (SOT)-induced[169,178,188] domain wall dynamics in Co-Ni multilayer based heterostructures. The internal spin structure of magnetic domain walls is diagnosed by measuring the spatial distribution of the emanating magnetic stray fields. By systematically controlling the SOT-induced domain wall motions, the local field environment of a proximal NV center can be precisely engineered, enabling electrical switching of NV photoluminescence, spin level energies, and coherence time between two different states. Local measurement of NV properties is achieved through the variation of anomalous Hall voltages, which is intimately tied to nanoscale domain-wall-motions in the magnetic channel of the Co-Ni device. Our results demonstrate the two-fold advantages of NV centers in quantum sensing and quantum information science research. The observed electrically tunable coupling between NV centers and propagating magnetic domain walls further highlights the appreciable opportunity for promoting the scalability, quantum interconnection, control of entanglement, and other tailored functionalities of NV-based hybrid

quantum systems.[174,189]

5.2 Co-Ni heterostructure composition and device structure]

We first discuss the magnetic films, device structures and our measurement platform as illustrated in Figures 5.1a and 5.1b. The structure of the magnetic device used in our studies is: substrate/Pt(5)/[Co(0.5)Ni(0.5)]2/Ta(5)[190] where the numbers in brackets indicate the thickness of each layer in nanometers. Co-Ni-based multilayer heterostructures were deposited on oxidized Si substrates by magnetron sputtering in a confocal geometry at room temperature. The Co-Ni multilayer has strong perpendicular anisotropy and is sandwiched between a Pt underlayer and a Ta capping layer, both of which have large spin-orbit coupling and a spin Hall effect of opposite sign.[188,190–192] These heavy metal layers serve as efficient and additive spin current sources to drive domain wall dynamics via SOT. The prepared samples were patterned into standard Hall cross structures with a width of $\sim$10 μm for electrical transport measurements as shown in Figure 5.1c. The anomalous Hall characterization (Figure 5.1d) shows full perpendicular remanence expected for strong perpendicular magnetic anisotropy and thin film thickness.[171,190]

5.3 Preliminary characterization of Co-Ni heterostructures

Figure 5.2b shows field dependent magnetization of a [Co-Ni]$_2$ sample measured at room temperature. The external magnetic field B_{ext} is applied perpendicular to the sample plane and the saturation magnetization is characterized to be $\sim$6763 G for samples with two repetitions of the Co-Ni layer. Figure 5.2a shows two typical sets of SOT-driven magnetic switching measurement results of the [Co-Ni]$_2$ device. The measured anomalous Hall signals exhibit positive (negative) jumps above the negative (positive) critical write currents. The magnetic switching curves change their polarity when reversing the direction of the longitudinal bias magnetic field, which is consistent with the mechanism of SOT-driven deterministic magnetic switching.[188]

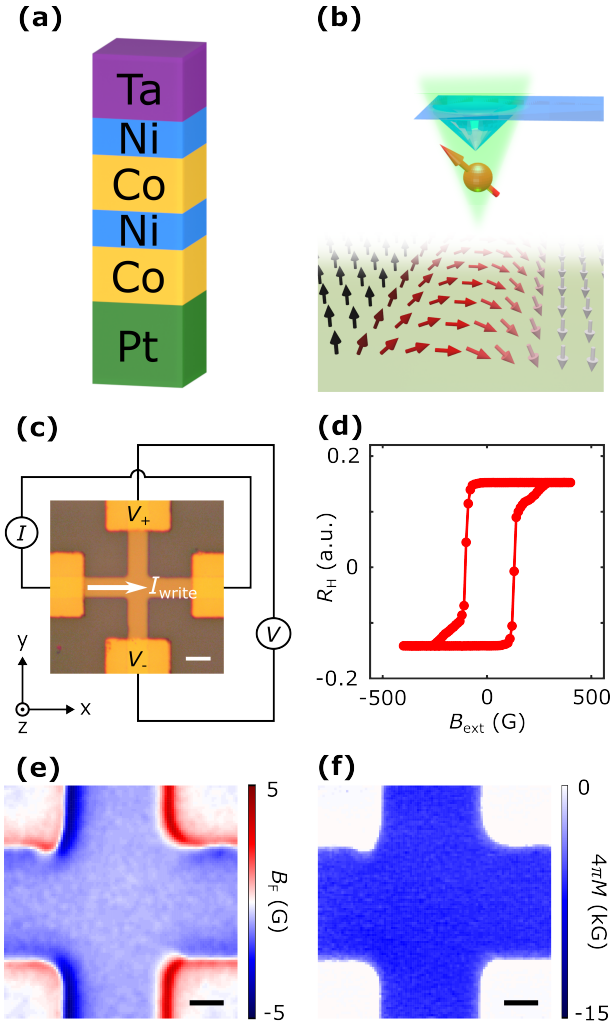

Figure 5.1. Measurement platform and Co-Ni multilayer device layout. (a) Schematic illustration of Co-Ni device structure. (b) Scanning NV magnetometry measurements of a spatially varying spin texture of a Co-Ni multilayer device. (c) Optical microscope image of a patterned Co-Ni multilayer Hall cross device with an illustration of the magneto-transport measurement geometry. Electrical write and read current pulses are applied along the x-axis, and the Hall voltage is measured along the y-axis. The scale bar is 10 μm. (d) Anomalous Hall resistance R_H of a patterned Co-Ni device measured as a function of an external perpendicular magnetic field B_{ext}. (e-f) Two-dimensional (2D) images of magnetic static stray field B_F (e) and reconstructed magnetization $4\pi M$ (f) of a Co-Ni Hall device. The external magnetic field B_{ext} is 30 G applied along the NV axis which is 54 degrees from the out-of-plane direction, and the scale bar is 3 μm. This figure is adapted from Ref. [31].

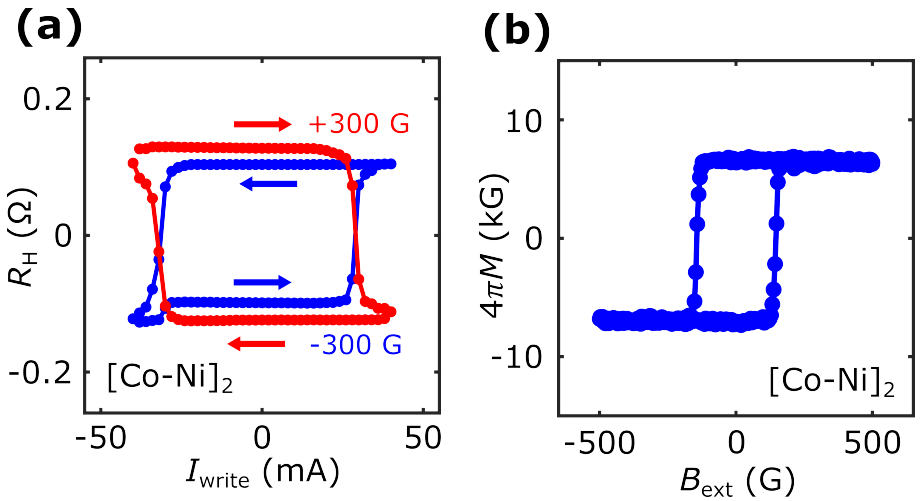

Figure 5.2. (a) Anomalous Hall resistance R_H of a patterned Pt/[Co-Ni]$_2$/Ta Hall device measured as a function of the write current I_{write} with application of a longitudinal bias field B_{ext} of ±300 G. (b) Field-dependent magnetization of [Co-Ni]$_2$ thin films measured at room temperature. The external magnetic field B_{ext} is applied along the out-of-plane direction of the film. This figure is adapted from Ref. [31].

5.4 Room temperature scanning NV magnetometry

To perform room-temperature nanoscale quantum sensing measurements, a micrometer-sized diamond cantilever[177,5,193] containing an NV single-electron spin is positioned above the surface of the patterned Hall device (Figure 5.1b). The diamond cantilever is attached to a quartz tuning fork for force-feedback atomic force microscopy (AFM) measurements. The ultimate spatial resolution of the scanning NV magnetometry system is primarily determined by the NV-to-sample distance,[12,5,186] which stays in the range from 50 nm to 200 nm in our measurements. We present here the detailed method to characterize this important instrumental parameter. Figure 5.3a shows the schematic of our measurement platform and the coordinate system used for numerical analysis. We assume that the Co-Ni magnetic device occupies the space Ω with $z \leq 0$ with its top surface lying in the x-y plane ($z = 0$). θ and ϕ represent the polar and azimuthal angles characterizing the NV spin orientation e_{NV}, which are equal to 54 and 0 degrees in the current measurement configuration. The NV center is located in the scanning plane of $z = d$. Quantitative measurement of the nanoscale NV-to-sample distance d can be realized by mapping the spatially dependent magnetic stray field B_F arising from the patterned Co-Ni multilayer device. Figure 5.3b shows a typical set of one-dimensional B_F data measured along the x-axis across the edge of the Co-Ni Hall device. Note that the presented scanning measurement was performed in a "contact" mode, where the diamond cantilever is attached to the surface of sample with a stand-off distance to be zero. According to dipole interactions, $B_F(x)$ can be expressed by the following equation:[194]

$$B_F(x) = \left[\mathbf{B}^{edge}\left(x - \frac{w_c}{2}\right) - \mathbf{B}^{edge}\left(x + \frac{w_c}{2}\right)\right] \cdot \mathbf{e}_{NV} \tag{5.1}$$

where w_c is the width of the Hall device and $B^{edge}(x)$ is a vector field with the x, y, z components to be:[194]

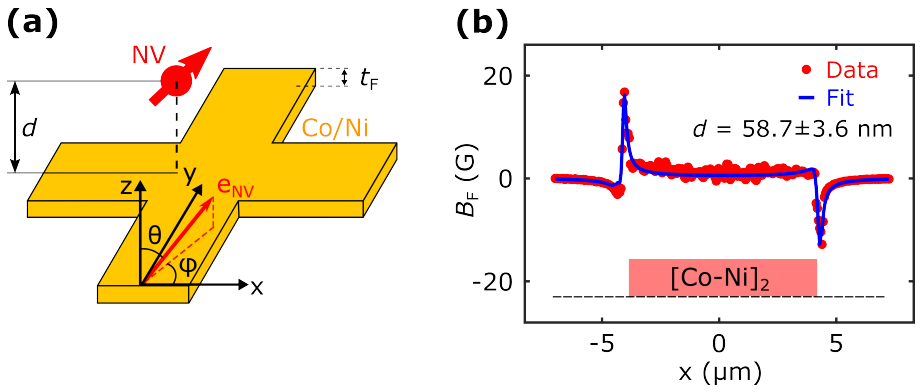

Figure 5.3. Characterization of NV-to-sample distance. (a) Schematic of the measurement platform and the coordinate system used for numerical analysis. (b) One-dimensional stray B_F measured across the lateral width (x-axis) of a patterned [Co-Ni] Hall device. The NV-to-sample distance can be quantitatively obtained by fitting the spatial distribution of the magnetic stray field to Eq. 5.1. This figure is adapted from Ref. [31].

$$\begin{cases} B_x^{edge}(x) & = 2M_f t_s \frac{d+\Delta d(x)}{x^2+[d+\Delta d(x)]^2} \\ B_x^{edge}(x) & = 0 \\ B_x^{edge}(x) & = -2M_f t_s \frac{x}{x^2+[d+\Delta d(x)]^2} \end{cases} \tag{5.2}$$

Here, M_s and t_F are the saturation magnetization and thickness of the Co-Ni sample, respectively, and Δd characterizes the variation of the sample height which is simultaneously recorded by atomic force microscopy during the scanning measurements. By fitting $B_F(x)$ to Equation 5.1, the NV-to-sample distance d is extracted to be 58.7 ± 3.6 nm. In the current studies, the NV-to-sample distance was $\sim$59 nm for scanning measurements of NV photoluminescence to enhance the signal-to-noise ratio.

5.5 Magnetic multilayer SOT switching devices

As a first step towards identifying the layout and structure of magnetic domain walls at the nanoscale, we carried out scanning NV imaging of SOT-driven domain wall movements in the Co-Ni multilayer devices. By scanning the NV center over a mesoscopic length scale above the sample surface, we are able to map the spatially varying B_F, enabling nanoscale imaging of local magnetic textures of the Co-Ni multilayer device as shown in Figure 5.1e. Through established reverse-propagation protocols as described in Appendix section A.1,[5,186] the corresponding magnetization ($4\pi M$) pattern of the magnetic device can be quantitatively reconstructed, as shown in Figure 5.1f. The obtained $4\pi M$ of the Co-Ni multilayer sample is $\sim$6763 G, and the strong perpendicular magnetic anisotropy of the sample is evidenced by the uniform spatial distribution of the out-of-plane magnetization.

5.6 Quantum imaging of SOT-driven deterministic magnetic switching

We now present data to show nucleation and propagation of domain walls during the SOT-driven deterministic magnetic switching process of the Co-Ni device. In these measurements, millisecond-long electrical write current pulses I_{write} are applied along the x-axis direction of the patterned Hall device, generating spin currents flowing along the $(\pm)z$-axis with polarization s oriented along the y-axis via the spin Hall effect in the heavy metal Pt and Ta layers,[188,195] as illustrated in Figure 5.1c. The accumulated spin currents are injected across the Co-Ni/heavy-metal interfaces and exert SOTs on the Néel type domain walls whose chirality is dictated by the interfacial Dzyaloshinskii-Moriya interaction (iDMI).[190,192,196–199] Application of an in-plane longitudinal magnetic field breaks the energy degeneracy of "up-down" and "down-up" domain walls with respect to the SOT, leading to preferential domain wall motions that accomplish bipolar switching of the Co-Ni magnetization between two magnetic easy states.[190] The anomalous Hall resistance R_H is recorded by supplying a read current with a magnitude of 3 mA after

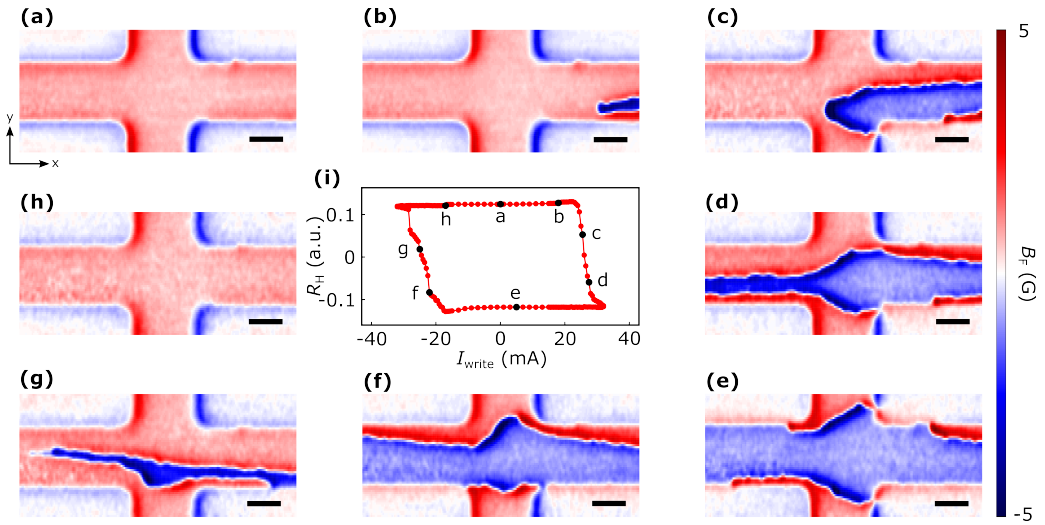

Figure 5.4. Scanning NV imaging of SOT-driven deterministic magnetic switching. (a-h) Nanoscale stray field imaging of domain wall motion during SOT-driven magnetic switching of a Co-Ni device. Scale bar is 5 μm for all images. (i) Anomalous Hall resistance R_H of the Co-Ni multilayer device measured as a function of write current I_{write}. For SOT-driven magnetic switching measurements, an external bias magnetic field of 190 G is applied along the applied current direction. Scanning NV imaging results presented in Figures 5.4a-5.4h were performed at individual points from "a" to "h" marked on the current-induced magnetic hysteresis loop shown in Figure 5.4i. This figure is adapted from Ref. [31].

each write current pulse I_{write}. Figure 5.4i shows a typical set of SOT-driven deterministic magnetic switching of the Co-Ni multilayer device. Notably, the measured anomalous Hall signals characterize reversible switching above the positive and negative critical write currents with a polarity depending on the sign of the external bias field, consistent with the mechanism of SOT-driven magnetic switching.[188]

Next, we utilize NV magnetometry to investigate the formation and propagation of magnetic domain walls at the nanoscale. Scanning NV imaging measurements are performed at the end of each electrical readout current pulse to visualize spin current-induced variations of the local magnetic texture. Figures 5.4a-5.4h show a series of representative magnetic stray field

B_F maps taken at the corresponding points ("a" to "h") on the SOT-induced magnetic hysteresis loop. At the initial magnetic state "a" where $I_{write} = 0$, the measured magnetic stray field B_F shows a largely uniform distribution over the Hall cross area, indicating a quasi-single domain state of the Co-Ni device with spontaneous perpendicular magnetization. At higher magnitude electrical write current pulses, the effect of the SOT becomes more pronounced, resulting in the nucleation of incipient magnetic domain walls at locations where the energy barrier is lowest, as shown in Figure 5.4b. The observed magnetic domain wall propagates with increasing write current pulse I_{write} and causes deterministic switching of the Co-Ni magnetization, as shown in Figures 5.4c-5.4e. When inverting the polarity of the write current, the up-aligned magnetic domain (along $+z$ direction) is preferentially selected by the exerted SOT, accompanied by the "reversal" of the magnetic switching polarity and the corresponding domain wall motions as shown in Figures 5.4f and 5.4g. Lastly, when sweeping the write current to point "h", the Co-Ni multilayer device returns to the initial magnetic state, showing an almost identical stray field map (Figure 5.4h).

5.7 Domain wall internal structure determination from stray field

The internal structure of the magnetic domain walls formed in the Co-Ni sample can be diagnosed by measuring the spatial distribution of the emanating magnetic stray fields, which is tied to its underlying spin configuration as illustrated in Figure 5.5a. Figure 5.5b shows a zoomed-in view of a stray field map of a formed domain wall in the magnetic device studied. The out-of-plane magnetic moments of Co-Ni multilayer sample exhibit an abrupt spatial rotation, leading to a sign reversal of the measured magnetic stray fields on each side of the domain wall. Figures 5.5c and 5.5d plot a line cut of the magnetic stray field B_x and B_z measured by scanning the diamond cantilever across the magnetic domain wall. Our results can be explained by a theoretical model assuming a combination of Bloch and left-handed Néel type magnetic domain

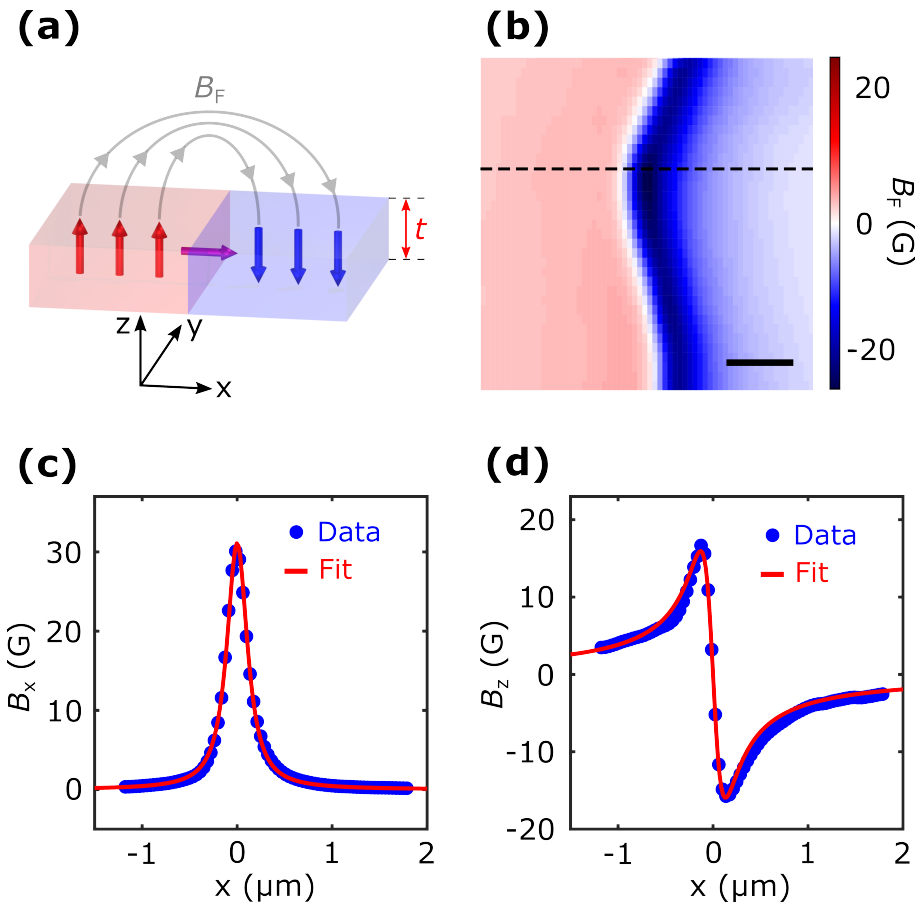

Figure 5.5. Probing the internal spin structure of magnetic domain walls in the Co-Ni multilayer device. (a) Schematic view of a magnetic domain wall formed in a perpendicularly magnetized Co-Ni film. The red (blue) and grey arrows represent the magnetic moment and emanated stay field, respectively. (b) Scanning NV imaging of stray fields arising from a magnetic domain wall in a Co-Ni multilayer device. Scale bar is 500 nm. (c-d) One-dimensional magnetic stray field B_x and B_z measured along the line-cut across the formed magnetic domain wall shown in Figure 5.5b. The markers are the experimental results, and the solid lines are fittings to a theoretical model assuming a combination of Bloch and left-handed Néel type domain wall. This figure is adapted from Ref. [31].

walls in the Co-Ni multilayers.[177,194]

5.8 Local control of a single NV center by domain-wall motions

Our scanning NV magnetometry results highlight highly efficient, current-driven domain wall dynamics at the nanoscale, providing an attractive platform to investigate the dipolar interactions between NV centers and the local magnetic textures of proximal magnetic devices. As such, we demonstrate electrically tunable NV-domain-wall coupling in the presented hybrid system and explicitly show that the photoluminescence, ESR energies, and coherence time of an NV center electron spin can be effectively controlled by reconfigurable domain wall motions. Figures 5.6a-5.6b show the schematics and underlying mechanisms of our experiments. The coupling between an NV center and the Co-Ni multilayer sample is mediated by local dipole stray fields arising from the proximal spin textures below the NV sensor. An in-plane, longitudinal magnetic field B_{ext} of 190 Gauss is applied in these experiments, and the distance between the NV center and sample surface is set to be $\sim$59 nm, ensuring sufficiently high NV sensitivity to the variation of local emanating stray fields. When a magnetic domain wall is away from the NV center, the local stray field B_F at the NV site is negligibly small, as illustrated in Figure 5.6a. In this case, the off-axial component of the external magnetic field B_{ext} will drive the NV center to a mixture of the $m_s = 0$ and ± 1 state with reduced photoluminescence, resulting in a relatively "dark" NV spin state.[200] In contrast, the local field environment is dramatically modified when the domain wall is propagating to the position right underneath the NV center (Figure 5.6b). A significant in-plane orientated stray field B_F emerges and effectively compensates the external magnetic field B_{ext}, leading to a reduction of the NV off-axis field and enhancement of the NV photoluminescence.

The scenarios envisioned above are experimentally confirmed by our scanning NV imaging measurements. Figures 5.6c and 5.6f present the stray field B_F and photoluminescence maps

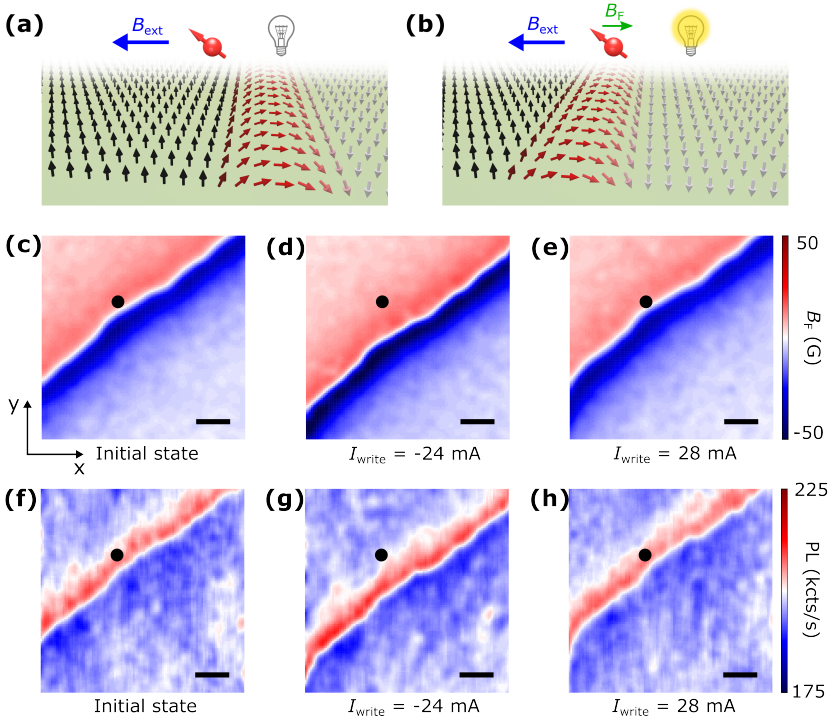

Figure 5.6. Local control of NV photoluminescence by nanoscale engineered magnetic domain wall motion. (a-b) Schematic illustration of tunable dipole interaction between an NV center and a propagating magnetic domain wall, resulting in reconfigurable engineering of the local magnetic field environment at the NV site. (c) Nanoscale stray field imaging of a magnetic domain wall formed in a Co-Ni multilayer device. (d-e) Application of a negative (-24 mA) and a positive (28 mA) electrical write current pulse reversibly drives domain wall forward propagation (d) and backward retraction (e) motions. (f-h) Corresponding NV photoluminescence imaging of the formed magnetic domain wall and its electrically controllable motion. The NV center shows enhanced (reduced) photoluminescence when being positioned right above (away from) the magnetic domain wall. Scale bar is 200 nm for all images. Black points in (c-h) mark the lateral position of the diamond cantilever for local control and measurement of NV properties presented in Figure 5.7. This figure is adapted from Ref. [31].

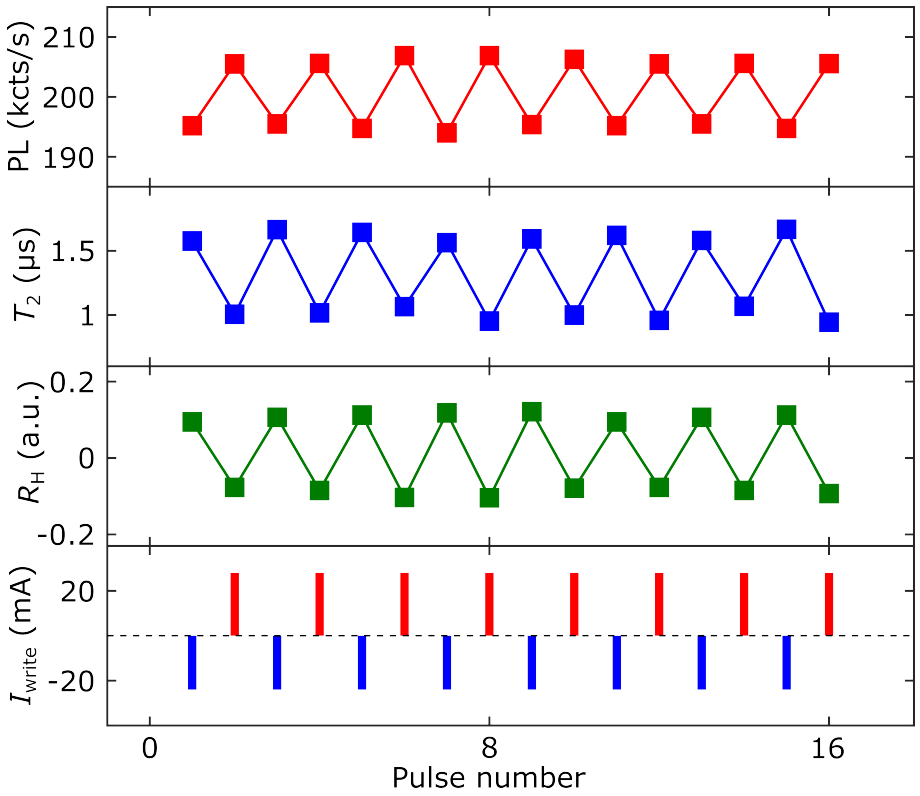

Figure 5.7. Reconfigurable control and measurement of NV photoluminescence and coherence time. Effective control of NV photoluminescence and coherence time (T_2) (top panels) by alternative applications of positive and negative write current pulses (bottom panel). The change of the NV spin properties can be well correlated to the anomalous Hall response driven by reversible domain wall motions in the Hall cross area of the Co-Ni multilayer device. Note that the NV center is not exactly positioned in the center above the formed magnetic domain wall when performing the two-state control measurements. This figure is adapted from Ref. [31].

measured by scanning the NV center over a magnetic domain wall formed in the Co-Ni multilayer device. Notably, the NV center stays in the "bright" state with enhanced photoluminescence when the diamond cantilever is positioned above the magnetic domain wall. As expected, the NV center enters the "dark" state when it is located above the uniform magnetic domain. We note that the lateral positions of the magnetic domain wall can be electrically controlled in a reversible way as shown in Figures 5.6d and 5.6e. Application of a write current pulse I_{write} of -24 mA will drive the forward propagation of domain wall over a length scale of $\sim$200 nm. In contrast, sending a current pulse of 28 mA will cause retraction of the magnetic domain wall back to the original position. The measured scanning NV photoluminescence image further confirms the reversible domain wall motions as shown in Figures 5.6g and 5.6h. In addition to photoluminescence, ESR energies and the intrinsic quantum coherence time (T_2) of the NV spin could also be controlled in a similar way by the nanoscale engineered domain wall motions. A linecut across the domain wall, as shown in Figure 5.8, reveals that the NV T_2 shows a significant decrease when the diamond cantilever is scanned across the magnetic domain wall, which is attributed to the gapless magnetic excitation arising from a ferromagnetic domain wall with a divergent susceptibility in the zero-frequency limit.[158,172,174,201] In contrast, the NV center shows an extended T_2 when sitting above the uniform magnetic domain.

The observed tunable dipolar interaction between an NV center and a magnetic domain wall provides a new avenue to electrically access the NV properties. When setting an NV center right above a formed magnetic domain wall, alternately applying write current pulses of opposite polarity will reversibly drive the magnetic domain wall either away from or back towards the NV spin, resulting in switching of the measured NV photoluminescence and coherence time between two different states as shown in Figure 5.7. By positioning the propagating domain wall in the Hall cross area, the observed binary variation of the NV spin properties can be further correlated to the simultaneously measured anomalous Hall signals of the Co-Ni multilayer device, enabling local control and measurement of NV centers. Note that the measured NV and magneto-transport signals are stable against consecutive write current pulses, demonstrating their robustness against

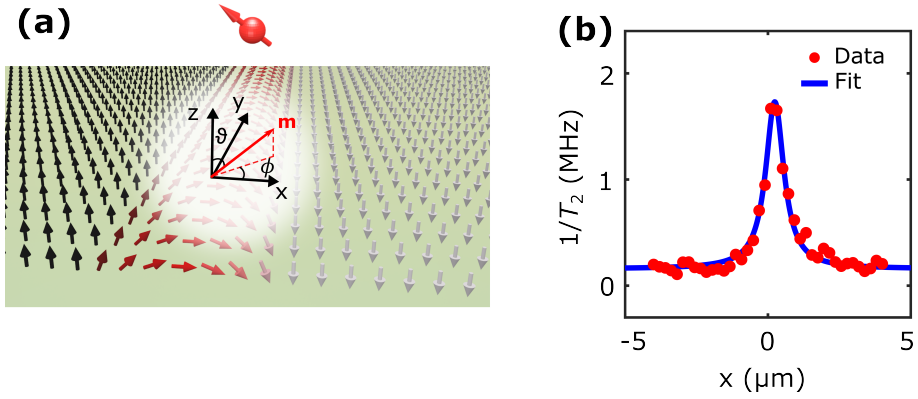

Figure 5.8. Variation of NV decoherence rate across a ferromagnetic domain wall. (a) Schematic and the coordinate system used for numerical analysis. (b) Experimentally measured one-dimensional NV spin decoherence rate ($1/T_2$) across a magnetic domain wall (red points), in agreement with the theoretical prediction (blue line). The NV spin decoherence rate far from the domain wall is very close to the value when the NV is retracted from the surface, which was approximately 0.125 MHz. This figure is adapted from Ref. [31].

external perturbations. Taking advantage of emergent racetrack memory technologies,[167] we expect that domain-wall-motion driven local addressing of individual quantum states of an array of NV spin qubits could be ultimately achieved.

5.9 Conclusion

In summary, we have demonstrated domain wall motion induced local control and readout of NV photoluminescence, spin level energies, and coherence time in a hybrid quantum spintronic system. By controlling magnetic domain wall motion in a Co-Ni multilayer device, the magnetic field environment of a proximal NV center can be modified in a reconfigurable way, enabling selective writing of NV spin properties. The reproducible control of NV photoluminescence emission and coherence time can be effectively detected by the anomalous Hall response, which is tied to the local magnetic domain wall position in the Hall cross area of the Co-Ni device. Our results illustrate the advantages of NV quantum metrology in studying nanoscale spin behaviors in emergent condensed matter systems. The demonstrated electrically controllable dipole coupling between NV centers and domain walls opens the possibility to realize interactive information transfer between spin qubits and electronic memory devices in hybrid solid-state systems. On a separate note, energy-efficient, current-driven fast domain wall motions may also serve as a suitable, mesoscopic scale quantum transducer/interconnecter,[7,158,189] promoting the functionality of NV centers in developing next-generation, transformative quantum information sciences and technological applications.

5.10 Acknowledgements.

Chapter 5 is adapted with permission from ACS Nano 2023, 17, 24, 25689–25696. Copyright 2023 The Authors. The dissertation author was an author of this paper, and coauthors are Senlei Li, Jeffrey A. Brock, Shu Zhang, Hanyi Lu, Mengqi Huang, Yuxuan Xiao, Jingcheng Zhou, Yaroslav Tserkovnyak, Eric E. Fullerton, Hailong Wang, and Chunhui Rita Du

Chapter 6

Low-Temperature Scanning NV Platform

6.1 Introduction

The arc of this dissertation is concerned with advancing NV sensing methodologies to what is currently required at the state-of-the-art to advance quantum sciences. We began in chapter 2 with diamond nanobeams. This NV centers are individually addressable by a confocal microscope system, and possess extraordinary coherence properties, as already described. While these NV's possess superlative qualities, in the course of a measurement they are necessarily static, and unable to perform measurements in more than on distinct location. We proceeded then in chapters 3 and 4 to describe widefield techniques, where we gained the ability to perform spatially resolved measurements, at the cost of NV coherence time, and a reduction of the spatial resolution to the optical diffraction limit of 500 nm. In chapter 5, a room-temperature scanning system was described, in which the single NV's in our diamond scanning probes retain high coherence properties, with around 10 times higher spatial resolution than the widefield system. This scanning system was confined to room temperature measurements, which limits its capacity to measure many cutting-edge magnetic and quantum systems, which only display their extraordinary properties at extremely low temperatures. In this chapter will be described the low-temperature extension of this technology, which can perform scanning measurements down to 1.8 K. Cryogenic NV scanning systems have recently advanced frontiers in measurements of superconductors[13,82,11], 2D magnets[5], non-trivial spin textures in antiferromagnets[202], twisted

moire materials[186], and unconventional current flow[203].

6.2 Experimental apparatus

6.2.1 Optical AFM/CFM Cryostat

Our low temperature scanning setup is implemented in a cryo-free, optically accessible cryostat. Sitting on top of this cryostat is a custom, home-built confocal or widefield microscope, which addresses NV centers through a window which looks down into the sample space. Within the sample space are two stacks of low-temperature capable piezo-based positioners. One of these stacks is used to mount the sample, and the other is used to hold diamond cantilevers containing single NV centers, purchased commercially. Using these stacks, we are able to perform force-feedback AFM measurements, controlled by the scanning probe microscope controller and *xy*-scan generator.

This system can operate at sample temperatures down to approximately 1.8 K. The positioning stacks are able to access a course positioning range of approximately 3×3 mm, and a fine scanning range of $40\ \mu$m at room temperature, and $20\ \mu$m at 2 K. The AFM scans have a typical RMS z-noise figure under 1 nm. This allows for sensitive AFM scans made concurrently with NV measurements. Static external magnetic fields are applied through a 1/1/1 T superconducting vector magnet. Due to thermal isolation between the superconducting magnet coils and the sample space, the magnet remains cold and superconducting, even while the sample space is at or slightly above room temperature. This allows for precise magnetic field control over the system's entire temperature range. Microwave control and spin-state manipulation signals are directed from the top of the sample probe at the top of the cryostat, through semi-rigid SMA cables, and directly to the sample space, where connections are made to the PCB onto which samples are fastened and measured. Details on the NV control hardware are given in the next section.

6.2.2 NV control equipment

NV initialization and readout laser pulses are provided by a pulsed laser operating at 515 nm. The NV photoluminescence is then collected by an avalanche photo-diode (APD), which sits outside the cryostat, and at room temperature. The APD outputs a 10-ns TTL pulse whenever a photon impinges on its detector surface, and these are detected, binned, and processed by a instruments FPGA based time-to-digital converter. Microwave signals are provided by an RF signal generator. The microwave signal is then sent through a Mini-circuits microwave switch, combined with other RF signals (if necessary) through an RF combiner/splitter, and finally amplified using an RF amplifier before being connected to the SMA connection at the top of the cryostat. The RF path is terminated with a 50 Ω resistor, to provide impedance matching, and to reduce the risk of burning sensitive on-chip fabricated RF wires. For pulsed NV-measurements, timing is achieved using a instruments digital pattern and arbitrary waveform generator (AWG). This device can provide 1 Giga-Sample/s digital signals, and 125 Mega-Sample/s arbitrary analog signals. The digital signals provide the timing control for photon counting, RF switch control, laser pulsing, and other events required for a given NV measurement. The AWG channels connect to the built-in mixer of the RF signal generator to provide fast RF frequency sweeping capabilities.

Chapter 7

Outlook

Quantum sensing using optically active spin qubits will continue to be an active area of research for many years to come. The extraordinary coherence properties of NV centers have meant that they have received the lion's share of research focus in this area, but other optical defects have begun to enter the scene to supplement NV research, and perform measurements where NV centers possess prohibitive shortcomings. For example, the fundamentally 3D nature of diamond-imbedded NV centers means that nanoscale proximity to sample can be a challenge, especially without access to costly and complex scanning cryostat systems like the one enunciated in chapter 6. To meet this need, optical defects in 2D materials, like boron vacancies in hexagonal boron nitride, are being used to perform quantum sensing measurements. The nature of these 2D transferrable materials means that establishing nanoscale proximity is a trivial matter, and except for some minor details, the measurement setup is identical to that of NV centers. To access extremely low temperature ranges and extremely high fields, some researchers have turned to the silicon-vacancy center (Si-V) in diamond, which is able to operate in conditions where NV field alignment and measurement contrast have so far proved challenging. Whichever qubit-based quantum sensing paradigm is ultimately used for a given measurement, the fundamental techniques remain similar. Those techniques outlined in this dissertation will continue to be perfected and expanded upon for years to come.

Chapter 8

Conclusion

In conclusion, nitrogen-vacancy centers in diamond have been used to study the local properties of a prototypical Mott insulator in VO_2, unconventional correlation between ferromagnetism and superconductivity in FTS, spin-dynamics in the topologically nontrivial antiferromagnet $MnBi_4Te_7$. We have also demonstrated local control over NV properties by nanoscale domain wall motions in [Co-Ni] multilayer structures. The techniques utilized for these measurements have advanced from diamond nanobeams, to diamond membranes for widefield magnetometry measurements, on to room-temperature scanning techniques. In order to build upon the already significant advances NV centers have made to cutting edge quantum sensing technologies, we also have built a low-temperature scanning NV setup using and AFM/CFM cryostat capable of reaching below 2 K. Low temperatures and high spatial resolution will be required to push forward quantum technologies into a new era, and the strategies and techniques used and developed in this dissertation will be used to enormous effect in the coming years.

Appendix A

Appendix

A.1 Reconstruction of magnetization maps of 2D materials

Here is presented the method to extract static magnetic stray fields generated from the magnetic sample by NV electron spin resonance (ESR) measurements.

Generally, a static magnetization distribution $\mathbf{M}(\mathbf{R}')$ generates a magnetic stray field distribution $\mathbf{B}_M(\mathbf{R})$[28]:

$$\mathbf{B}_M(\mathbf{R}) = \int d^3\mathbf{R}' \mathscr{D}\left(\mathbf{R},\mathbf{R}'\right)\mathbf{M}\left(\mathbf{R}'\right), \tag{A.1}$$

where $\mathscr{D}(\mathbf{R},\mathbf{R}') = -\nabla_{\mathbf{R}}\nabla_{\mathbf{R}'}\left(1/|\mathbf{R}-\mathbf{R}'|\right)$ is the magnetostatic Green's function tensor between coordinates $\mathbf{R}$ = (x, y, z) and $\mathbf{R}'$ = (x', y', z'). Focusing on the magnetic field at the positions of the NV centers (z = d), we take the following Fourier transform in the x and y directions, where translational symmetries are present, with r = (x, y) and k = (k_x, k_y). Introducing Fourier transforms for the magnetic stray field $\mathbf{B}_M$ and the static magnetization $\mathbf{M}$:

$$\begin{aligned}\mathbf{B}_M^{NV}(\mathbf{k}) &= \int \mathbf{B}_M(\mathbf{r},d)e^{i\mathbf{k}\cdot\mathbf{r}}d^2\mathbf{r}\\ \mathbf{M}(\mathbf{k},z) &= \int \mathbf{M}(\mathbf{r},z)e^{i\mathbf{k}\cdot\mathbf{r}}d^2\mathbf{r}\end{aligned} \tag{A.2}$$

Invoking the following identity[204]:

$$\frac{1}{|\mathbf{R}-\mathbf{R'}|} = \int \frac{d^2\mathbf{k}}{(2\pi)^2}\frac{2\pi}{k}e^{-k|z-z'|}e^{i\mathbf{k}\cdot\mathbf{r}-\mathbf{r'}} \tag{A.3}$$

where $k = |k|$, we can obtain the Green's function tensor in Fourier space for $\alpha, \beta = x, y$:

$$\begin{cases} D_{\alpha\beta}(\mathbf{k}, z') & = -2\pi\left(k_\alpha k_\beta / k\right)e^{-k(d-z')}, \\ D_{\alpha z}(\mathbf{k}, z') & = 2\pi i k_\alpha e^{-k(d-z')} \\ D_{zz}(\mathbf{k}, z') & = 2\pi k e^{-k(d-z')} \end{cases} \tag{A.4}$$

Thus

$$\mathbf{B}_M^{NV}(\mathbf{k}) = \int D(\mathbf{k}, z')\mathbf{M}(\mathbf{k}, z')dz' \tag{A.5}$$

For thin samples and flakes, we are interested in an effectively two-dimensional magnetization distribution, we assume **M** to be uniform along the thickness direction, and therefore independent of z. We consider primarily sample with easy-axis perpendicular anisotropy, and therefore the magnetization is assumed to be spontaneously aligned along the z direction, $\mathbf{M}(\mathbf{k}, z) = M(\mathbf{k})\hat{z}$. With the NV centers located at z = d, based on Eq. A.4 and Eq. A.5, the component of the magnetic field directed along the NV axis $B_M^{NV}(\mathbf{k})$ can be expressed as:

$$\begin{aligned} B_M^{NV}(\mathbf{k}) &= \int_{-t_F}^{0} e_{NV} \cdot D(\mathbf{k}, z') \cdot M(\mathbf{k})\hat{z}dz' \\ &= 2\pi e^{-kd}(1 - e^{-kt_F})\left(\cos\theta - i\frac{k_x}{k}\sin\theta\cos\phi - i\frac{k_y}{k}\sin\theta\sin\phi\right)M(\mathbf{k}), \end{aligned} \tag{A.6}$$

where t_F is the thickness of the magnetic sample, and θ and ϕ represent the polar and azimuthal angles of the NV axis, respectively. For NV imaging experiments conducted using [111] cut diamond membranes, this equation can be simplified to:

$$B_M^{NV}(\mathbf{k}) = 2\pi e^{-kd}(1-e^{-kt_F})M(\mathbf{k}), \tag{A.7}$$

We may now introduce an inverse Fourier transform to reconstruct the magnetization in the real space:

$$M(\mathbf{r}) = \frac{1}{(2\pi)^2}\int M(\mathbf{k})e^{-i\mathbf{k}\cdot\mathbf{r}}d^2\mathbf{k}. \tag{A.8}$$

A.2 Reconstruction of AC supercurrents in 2D superconducting materials

The spatial distribution of AC supercurrents in a superconducting flake can be reconstructed by the measured microwave field B_{SU}. B_{SU} at a specific position (x,y,z) can be expressed by the Biot-savart law:[105]

$$B_{SU}(x,y,z) = \frac{\mu_0 d}{4\pi}\int \frac{J_x(x',y')(y-y') - J_y(x',y')(x-x')}{\left((x-x')^2+(y-y')^2+z^2\right)^{3/2}} \tag{A.9}$$

where d is the thickness of a flake and μ_0 is the vacuum permeability. Due to the quasi-2D confinement, we assume that the supercurrent $\mathbf{J} = (J_x, J_y)$ only depends on the in-plane parameters x and y. Next, we introduce 2D Fourier transforms for B_{SU} and $J_k(k = x,y)$:[4]

$$\tilde{B}_{SU}(k_x,k_y,z_{NV}) = \iint B_{SU}(x,y,z_{NV})e^{i(k_x x+k_y y)}dxdy \tag{A.10}$$

$$\tilde{J}_k(k_x,k_y,z_{NV}) = \iint J_k(x,y,z_{NV})e^{i(k_x x+k_y y)}dxdy \tag{A.11}$$

where z_{NV} is the distance between the NV center and surface of a 2D superconducting flake. Combining Equations A.10 and A.11, we have:

$$\tilde{B}_{SU}(k_x,k_y,z_{NV}) = i\frac{\mu_0 d}{2}e^{-z_{NV}\sqrt{k_x^2+k_y^2}}\left[\frac{k_y}{\sqrt{k_x^2+k_y^2}}\tilde{J}_x(k_x,k_y) - \frac{k_x}{\sqrt{k_x^2+k_y^2}}\tilde{J}_y(k_x,k_y)\right] \tag{A.12}$$

According to the current continuity equation: $\nabla \cdot \mathbf{J} = 0$, we can get:

$$k_x\tilde{J}_x(k_x,k_y) + k_y\tilde{J}_y(k_x,k_y) = 0 \tag{A.13}$$

Combining Equations A.12 and A.13, we have:

$$\tilde{J}_x(k_x,k_y) = -\frac{2ik_y e^{z_{NV}\sqrt{k_x^2+k_y^2}}}{\mu_0 d\sqrt{k_x^2+k_y^2}}\tilde{B}_{SU}(k_x,k_y) \tag{A.14}$$

and

$$\tilde{J}_y(k_x,k_y) = \frac{2ik_x e^{z_{NV}\sqrt{k_x^2+k_y^2}}}{\mu_0 d\sqrt{k_x^2+k_y^2}}\tilde{B}_{SU}(k_x,k_y) \tag{A.15}$$

To reduce the high frequency noise, $\tilde{J}_x$ are passed through a Hanning filter.[205] Finally, we introduce the inverse Fourier transform to obtain the supercurrent density in real space:[4]

$$J_k(x,y) = \frac{1}{(2\pi)^2}\iint \tilde{J}_k(k_x,k_y)e^{-i(k_x x+k_y y)}dk_x dk_y \tag{A.16}$$

A.3 London penetration depth of 2D superconductor

In this section, we present the method to extract the London penetration depth of a quasi-2D flake via the measured microwave magnetic field B_{SU}. We start from the AC version of the London equation:

$$\partial_x J_y - \partial_y J_x = -\frac{\alpha(x,y,T)}{\mu_0 d}B_{AC} \tag{A.17}$$

where $B_{AC} = B_{SU} + B_{MW}$ and all three quantities orient along the out-of-plane direction. Here, we introduce a complex parameter $\alpha(x,y,T) = 2\pi i f \mu_0 \sigma(f,x,y,T)d$ to account for the dynamic response of our 2D superconductor in a microwave field with frequency f. The complex conductivity σ in the two-fluid model can be written as: $\sigma = \sigma_1 - \sigma_2$ and the real and imaginary components are related to the London penetration depth λ in the following way:[105]

$$\sigma_1(x,y,T) = \frac{\tau(T)}{\mu_0 \lambda^2(x,y,0K)} \left(1 - \frac{\lambda^2(x,y,0K)}{\lambda^2(x,y,T)}\right) \tag{A.18}$$

And

$$\sigma_2(x,y,T) = \frac{1}{2\pi\mu_0 \lambda^2(x,y,T) f} \tag{A.19}$$

where $\tau(T)$ is the relaxation time of charge carriers. The supercurrents obey current conservation ($\nabla \cdot \mathbf{J} = 0$), therefore, we can write the surface current density (J_x,J_y) with a scalar function ϕ in the following way:

$$J_x = \partial_y \phi \tag{A.20}$$

$$J_x = \partial_y \phi \tag{A.21}$$

Substituting Equation A.20 and A.21 into Equation A.17, the London equation becomes:

$$\nabla^2 \phi = \frac{\alpha(x,y,T)}{\mu_0 d} B_{AC}(x,y) \tag{A.22}$$

where α is related to the London penetration depth by: $Re\{\alpha(x,y,T)\} = d/\lambda^2(x,y,T)$. The solution of ϕ is given by:[206]

$$\phi(x,y) = \frac{1}{4\pi}\iint_{\Omega} dx'dy' ln\left((x-x')^2+(y-y')^2\right)\frac{\alpha(x',y',T)}{\mu_0 d}B_{AC}(x',y') \tag{A.23}$$

Combining Equations A.20, A.21, and A.23, the surface current density J_x and J_y can be written as:

$$J_x(x,y) = \frac{1}{2\pi\mu_0 d}\iint_{\Omega} dx'dy'\frac{\alpha(x',y',T)(y-y')B_{AC}(x',y')}{(x-x')^2+(y-y')^2} \tag{A.24}$$

$$J_y(x,y) = -\frac{1}{2\pi\mu_0 d}\iint_{\Omega} dx'dy'\frac{\alpha(x',y',T)(x-x')B_{AC}(x',y')}{(x-x')^2+(y-y')^2} \tag{A.25}$$

Substituting Equations A.24 and A.25 into the Biot-Savart equation, we can obtain the microwave magnetic field $\mathbf{B}_{SU}$ generated by supercurrents:

$$\mathbf{B}_{SU}(x,y,z) = \frac{\mu_0 d}{4\pi}\int \frac{\mathbf{J}(x',y')\times(x-x',y-y',z)}{\left((x-x')^2+(y-y')^2+z^2\right))^{3/2}}dx'dy' \tag{A.26}$$

A.4 Reconstruction of DC supercurrents in 2D superconducting materials

When the thickness of a superconducting flake is significantly smaller than its lateral dimensions, the out-of-plane component of the supercurrent density will be negligible in a steady state. Thus, B_{SC} along the z-axis direction can be written as a function of the in-plane supercurrent density (J_x, J_y) by solving the Biot-Savart equation:[105]

$$B_{SU}(x,y,z) = \frac{\mu_0 d}{4\pi}\int \frac{J_x(x',y')(y-y') - J_y(x',y')(x-x')}{\left((x-x')^2+(y-y')^2+z^2\right)^{3/2}} \tag{A.27}$$

The supercurrent density (J_x, J_y) can be obtained from the DC stray field generated from the superconducting flake. For a quasi-2D superconducting system, (J_x, J_y) and the produced

magnetic fields are related by the classical London equation as follows:[207]

$$\partial_x J_y - \partial_y J_x = -\frac{B_z^{tot}(x,y)}{\mu_0 \lambda^2(x,y,T)} \tag{A.28}$$

Where $B_z^{tot} = B_{SC} + B_z^{ext}$ is the total DC magnetic field along the z-axis, B_z^{ext} is the out-of-plane component of the external static magnetic field, and λ is the London penetration depth. According to the current conservation rule ($\nabla \cdot \mathbf{J} = 0$), the surface supercurrent density (J_x, J_y) can be expressed by a scalar function ϕ, as shown in Equations A.20 and A.21. Therefore, the London equation becomes:

$$\nabla^2 \phi = \frac{B_z^{tot}(x,y)}{\mu_0 \lambda^2(x,y,T)} \tag{A.29}$$

and the solution of ϕ is given by:[206]

$$\phi(x,y) = \frac{1}{4\pi} \iint_\Omega dx'dy' ln\left((x-x')^2 + (y-y')^2\right) \frac{B_z^{tot}(x,y)}{\mu_0 \lambda^2(x,y,T)} \tag{A.30}$$

Combining Equations A.20, A.21, and A.30, the surface supercurrent density J_x, J_y can be written as:

$$J_x(x,y) = \frac{1}{2\pi} \int_\Omega dx'dy' \frac{(y-y')B_z^{tot}(x',y')}{\mu_0 \lambda^2(x,y,T)\left[(x-x')^2 + (y-y')^2\right]} \tag{A.31}$$

and

$$J_y(x,y) = \frac{1}{2\pi} \int_\Omega dx'dy' \frac{(x-x')B_z^{tot}(x',y')}{\mu_0 \lambda^2(x,y,T)\left[(x-x')^2 + (y-y')^2\right]} \tag{A.32}$$

Substituting Equations A.31 and A.32 into Equation A.27, one can obtain the magnetic field generated by DC supercurrents.

A.5 Extraction of nitrogen-vacancy spin relaxation rates

In addition to static magnetic fields, NV centers also act as sensitive probes of non-coherent magnetic fields. Fluctuating magnetic fields at the NV ESR frequencies can induce m_s = $0 \leftrightarrow \pm 1$ transitions which can be optically accessed by NV relaxometry measurements via spin-dependent photoluminescence. We experimentally detect spin-dependent NV photoluminescence as a function of the delay time t between the initialization and readout green laser pulses to extract the spin lifetime of NV centers. The NV spins are first initialized to the $m_s = 0$ state at t = 0. The decrease (increase) of the NV photoluminescence corresponding to $m_s = 0$ (± 1) states as a function the delay time t indicates the relaxation of NV spin to a mixture of the three-level spin state. To extract the NV relaxation rates $\Gamma_{\pm}$, we fit the time-dependent photoluminescence data into following equation, which is based on a three-level model[28,34]:

$$\frac{d}{dt}\begin{pmatrix} P_0(t) \\ P_+(t) \\ P_-(t) \end{pmatrix} = \begin{pmatrix} -(\Gamma_+ + \Gamma_+) & \Gamma_+ & \Gamma_- \\ \Gamma_+ & -\Gamma_+ & 0 \\ \Gamma_- & 0 & -\Gamma_- \end{pmatrix} \begin{pmatrix} P_0(t) \\ P_+(t) \\ P_-(t) \end{pmatrix} \tag{A.33}$$

Here, P_0, P_+, and $P_-$are the occupation probabilities of an NV spin in the $m_s = 0$, m_s = +1, and m_s = -1 states, respectively, Γ_+ and Γ_- characterize the spin relaxation rates of the $m_s = 0 \leftrightarrow$ +1 and $m_s = 0 \leftrightarrow$ -1 transitions. Note that the magnetic noise generated by the the flakes in this dissertation will not affect the m_s = +1 $\leftrightarrow$ -1 transition to the leading order of the dipolar coupling, therefore, the corresponding relaxation rate is set to zero.

A.6 Permanent Magnet Alignment

NV magnetometry frequently requires manipulation of the external field condition, both to influence the magnetic properties of the material being studied, and to appropriately bias the NV spin states to enable clear separation of the $|m_s = \pm 1\rangle$ spin states for ODMR measurements. For all NV experiments performed in this dissertation, the external field was provided by a

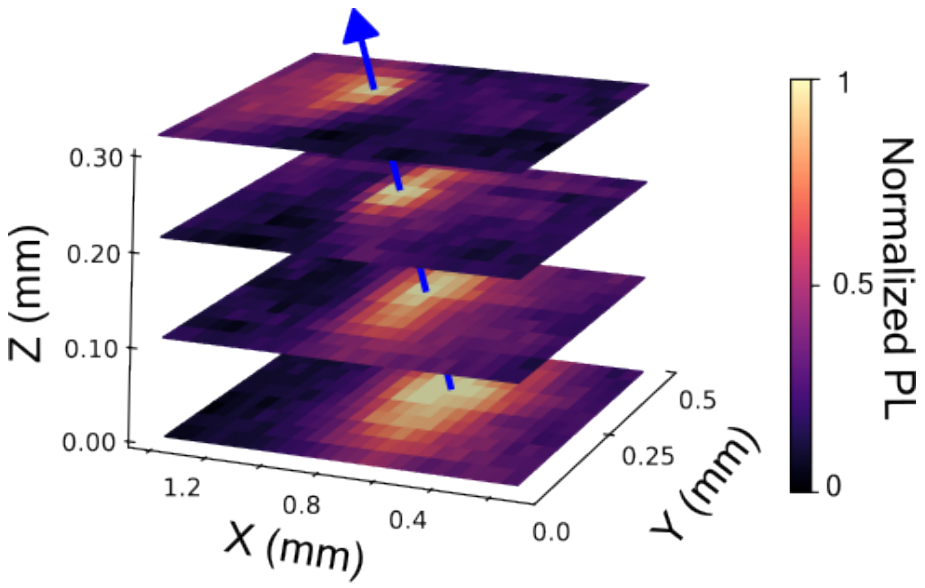

Figure A.1. Process for alignment of external magnetic field from a permanent magnet. The magnet is scanned in successive planes in the z direction. The aligned points on these maps show up as points of high photoluminescence.

neodymium-based cylindrical permanent magnet mounted on a micromechanical *xyz*-movement stage. The magnetic field surrounding these magnets was simulated, with the assumption that the cylindrical symmetry of the magnets reduces the results to a two-dimensional map of vector components. External magnetic field alignment to the NV center was done using the property that the NV will show a higher photoluminescence when the external field is aligned to its axis, as shown in Figure A.1. The *xyz* coordinates of these points are used with our magnet simulation to determine the full line of points in the space above the magnet where the magnetic field would be aligned. This allows for easy application of aligned fields across our entire desired range of bias fields.

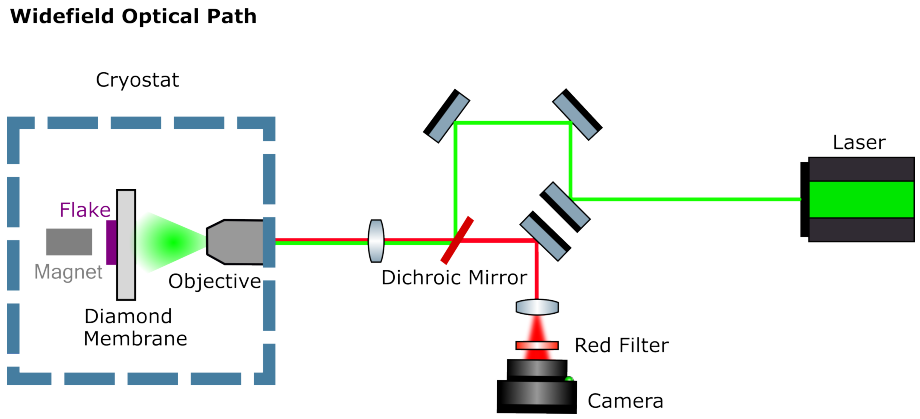

Figure A.2. Simplified schematic of the widefield optical path, as used in chapters 3 and 4.

A.7 NV microscope design and operation

A.7.1 Widefield NV microscope

Figure A.2 shows a basic schematic of the optical components involved in our widefield NV microscope. The laser is generated by a 515nm (green) laser. The beam is first collimated and expanded, before it is focused on the back of the objective. This ensures a diverging beam of the correct size before it hits the sample. Returning red photoluminescence passes through a dichroic mirror, before hitting a final lens to alter magnification before impinging on the camera sensor.

The pulse sequences of widefield measurements are constrained by the minimum exposure time of our camera, and by the reduced sensitivity of the CMOS photodetector, compared to our single photon detectors. In these experiments, hundreds or thousands of repetitions of individual pulse sequence are recorded with each camera exposure. Since light intensity is being recorded for the entirety of each laser pulse, the laser power, and pulse length must be tuned to yield the maximum spin contrast.

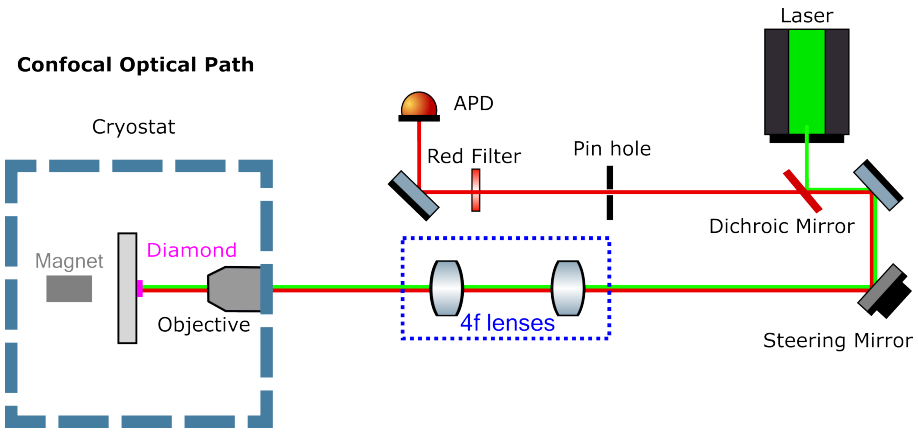

Figure A.3. Simplified schematic of the widefield optical path, as used in chapter 2

A.7.2 Confocal NV microscope

The confocal optics used in this dissertation are shown in Figure A.3. The laser is generated by a 515nm (green) laser. It bounces off a dichroic before it is incident upon a fast steering mirror, to direct the beam to the NV locations. Before entering the objective, it passes through a 4f lens system, which ensures that despite the large steering angle of the fast steering mirror, the collimated laser beam only travels along the back of the objective. The beam is focused onto a sample, then the returning red photoluminescence passes back along the path, through the dichroic, through a pinhole to filter out uncollimated light, through a red filter to remove photons outside the NV emission spectrum, and finally into our APD to be counted.

Bibliography

[1] L. Rondin, J. P. Tetienne, T. Hingant, J. F. Roch, P. Maletinsky, and V. Jacques. Magnetometry with nitrogen-vacancy defects in diamond. *Reports on Progress in Physics*, 77(5), 2014.

[2] C. L. Degen, F. Reinhard, and P. Cappellaro. Quantum sensing. *Reviews of Modern Physics*, 89(3), 7 2017.

[3] Aurore Finco, Angela Haykal, Rana Tanos, Florentin Fabre, Saddem Chouaieb, Waseem Akhtar, Isabelle Robert-Philip, William Legrand, Fernando Ajejas, Karim Bouzehouane, Nicolas Reyren, Thibaut Devolder, Jean Paul Adam, Joo Von Kim, Vincent Cros, and Vincent Jacques. Imaging non-collinear antiferromagnetic textures via single spin relaxometry. *Nature Communications 2021 12:1*, 12(1):1–6, 2 2021.

[4] Jean Philippe Tetienne, Nikolai Dontschuk, David A. Broadway, Alastair Stacey, David A. Simpson, and Lloyd C.L. Hollenberg. Quantum imaging of current flow in graphene. *Science Advances*, 3(4), 4 2017.

[5] L. Thiel, Z. Wang, M. A. Tschudin, D. Rohner, I. Gutiérrez-Lezama, N. Ubrig, M. Gibertini, E. Giannini, A. F. Morpurgo, and P. Maletinsky. Probing magnetism in 2D materials at the nanoscale with single-spin microscopy. *Science*, 364(6444):973–976, 6 2019.

[6] C. E. Bradley, J. Randall, M. H. Abobeih, R. C. Berrevoets, M. J. Degen, M. A. Bakker, M. Markham, D. J. Twitchen, and T. H. Taminiau. A Ten-Qubit Solid-State Spin Register with Quantum Memory up to One Minute. *Physical Review X*, 9(3):031045, 9 2019.

[7] David D Awschalom, Chunhui Rita Du, Rui He, F Joseph Heremans, Axel Hoffmann, Justin Hou, Hidekazu Kurebayashi, Yi Li, Luqiao Liu, Valentine Novosad, Joseph Sklenar, Sean E Sullivan, Dali Sun, Hong Tang, Vasyl Tyberkevych, Cody Trevillian, Adam W Tsen, Leah R Weiss, Wei Zhang, Xufeng Zhang, Liuyan Zhao, and Ch. W Zollitsch. Quantum Engineering With Hybrid Magnonic Systems and Materials (Invited Paper). *IEEE Transactions on Quantum Engineering*, 2:1–36, 2021.

[8] Lilian Childress and Ronald Hanson. Diamond NV centers for quantum computing and quantum networks. *MRS Bulletin*, 38(2):134–138, 2 2013.

[9] Sébastien Pezzagna and Jan Meijer. Quantum computer based on color centers in diamond. *Applied Physics Reviews*, 8(1), 3 2021.

[10] Gerald Q. Yan, Senlei Li, Tatsuya Yamamoto, Mengqi Huang, Nathan J. McLaughlin, Takayuki Nozaki, Hailong Wang, Shinji Yuasa, and Chunhui Rita Du. Electric-Field-Induced Coherent Control of Nitrogen-Vacancy Centers. *Physical Review Applied*, 18(6):064031, 12 2022.

[11] P. J. Scheidegger, S. Diesch, M. L. Palm, and C. L. Degen. Scanning nitrogen-vacancy magnetometry down to 350 mK. *Applied Physics Letters*, 120(22):224001, 5 2022.

[12] Francesco Casola, Toeno Van Der Sar, and Amir Yacoby. Probing condensed matter physics with magnetometry based on nitrogen-vacancy centres in diamond. *Nature Reviews Materials*, 3, 1 2018.

[13] Matthew Pelliccione, Alec Jenkins, Preeti Ovartchaiyapong, Christopher Reetz, Eve Emmanouilidou, Ni Ni, and Ania C. Bleszynski Jayich. Scanned probe imaging of nanoscale magnetism at cryogenic temperatures with a single-spin quantum sensor. *Nature Nanotechnology*, 11(8):700–705, 8 2016.

[14] Marcus W. Doherty, Neil B. Manson, Paul Delaney, Fedor Jelezko, Jörg Wrachtrup, and Lloyd C.L. Hollenberg. The nitrogen-vacancy colour centre in diamond. *Physics Reports*, 528(1):1–45, 7 2013.

[15] R. Hanson, O. Gywat, and D. D. Awschalom. Room-temperature manipulation and decoherence of a single spin in diamond. *Physical Review B*, 74(16):161203, 10 2006.

[16] J. H.N. Loubser and J. A. Van Wyk. Electron spin resonance in the study of diamond. *Reports on Progress in Physics*, 41(8):1201, 8 1978.

[17] Amila Ariyaratne, Dolev Bluvstein, Bryan A. Myers, and Ania C.Bleszynski Jayich. Nanoscale electrical conductivity imaging using a nitrogen-vacancy center in diamond. *Nature Communications 2018 9:1*, 9(1):1–7, 6 2018.

[18] David A. Hopper, Richard R. Grote, Samuel M. Parks, and Lee C. Bassett. Amplified Sensitivity of Nitrogen-Vacancy Spins in Nanodiamonds Using All-Optical Charge Readout. *ACS Nano*, 12(5):4678–4686, 5 2018.

[19] B. J. Shields, Q. P. Unterreithmeier, N. P. De Leon, H. Park, and M. D. Lukin. Efficient Readout of a Single Spin State in Diamond via Spin-to-Charge Conversion. *Physical Review Letters*, 114(13):136402, 3 2015.

[20] G. D. Fuchs, V. V. Dobrovitski, D. M. Toyli, F. J. Heremans, C. D. Weis, T. Schenkel, and D. D. Awschalom. Excited-state spin coherence of a single nitrogen–vacancy centre in

diamond. *Nature Physics 2010 6:9*, 6(9):668–672, 7 2010.

[21] N. B. Manson, J. P. Harrison, and M. J. Sellars. Nitrogen-vacancy center in diamond: Model of the electronic structure and associated dynamics. *Physical Review B - Condensed Matter and Materials Physics*, 74(10):104303, 9 2006.

[22] Nathan J. McLaughlin, Yoav Kalcheim, Albert Suceava, Hailong Wang, Ivan K. Schuller, and Chunhui Rita Du. Quantum Sensing of Insulator-to-Metal Transitions in a Mott Insulator. *Advanced Quantum Technologies*, 4(5), 5 2021.

[23] Nathan J. McLaughlin, Hailong Wang, Mengqi Huang, Eric Lee-Wong, Lunhui Hu, Hanyi Lu, Gerald Q. Yan, Genda Gu, Congjun Wu, Yi Zhuang You, and Chunhui Rita Du. Strong Correlation between Superconductivity and Ferromagnetism in an Fe-Chalcogenide Superconductor. *Nano Letters*, 21(17):7277–7283, 9 2021.

[24] F. Jelezko, T. Gaebel, I. Popa, A. Gruber, and J. Wrachtrup. Observation of Coherent Oscillations in a Single Electron Spin. *Physical Review Letters*, 92(7), 2004.

[25] G. D. Fuchs, V. V. Dobrovitski, D. M. Toyli, F. J. Heremans, and D. D. Awschalom. Gigahertz dynamics of a strongly driven single quantum spin. *Science*, 326(5959):1520–1522, 12 2009.

[26] R. Hanson, V. V. Dobrovitski, A. E. Feiguin, O. Gywat, and D. D. Awschalom. Coherent dynamics of a single spin interacting with an adjustable spin bath. *Science*, 320(5874):352–355, 4 2008.

[27] Nathan J. Mclaughlin, Chaowei Hu, Mengqi Huang, Shu Zhang, Hanyi Lu, Gerald Q. Yan, Hailong Wang, Yaroslav Tserkovnyak, Ni Ni, and Chunhui Rita Du. Quantum Imaging of Magnetic Phase Transitions and Spin Fluctuations in Intrinsic Magnetic Topological Nanoflakes. *Nano Letters*, 22(14):5810–5817, 7 2022.

[28] Toeno Van Der Sar, Francesco Casola, Ronald Walsworth, and Amir Yacoby. Nanometre-scale probing of spin waves using single-electron spins. *Nature Communications*, 6, 8 2015.

[29] Brendan A. McCullian, Ahmed M. Thabt, Benjamin A. Gray, Alex L. Melendez, Michael S. Wolf, Vladimir L. Safonov, Denis V. Pelekhov, Vidya P. Bhallamudi, Michael R. Page, and P. Chris Hammel. Broadband multi-magnon relaxometry using a quantum spin sensor for high frequency ferromagnetic dynamics sensing. *Nature Communications*, 11(1), 12 2020.

[30] S. Kolkowitz, A. Safira, A. A. High, R. C. Devlin, S. Choi, Q. P. Unterreithmeier, D. Patterson, A. S. Zibrov, V. E. Manucharyan, H. Park, and M. D. Lukin. Probing Johnson noise and ballistic transport in normal metals with a single-spin qubit. *Science*, 347(6226):1129–

1132, 3 2015.

[31] Nathan J. McLaughlin, Senlei Li, Jeffrey A. Brock, Shu Zhang, Hanyi Lu, Mengqi Huang, Yuxuan Xiao, Jingcheng Zhou, Yaroslav Tserkovnyak, Eric E. Fullerton, Hailong Wang, and Chunhui Rita Du. Local Control of a Single Nitrogen-Vacancy Center by Nanoscale Engineered Magnetic Domain Wall Motion. *ACS Nano*, 17:25689–25696, 12 2023.

[32] E. L. Hahn. Spin Echoes. *Physical Review*, 80(4):580, 11 1950.

[33] Michael J. Burek, Nathalie P. De Leon, Brendan J. Shields, Birgit J.M. Hausmann, Yiwen Chu, Qimin Quan, Alexander S. Zibrov, Hongkun Park, Mikhail D. Lukin, and Marko Lončar. Free-standing mechanical and photonic nanostructures in single-crystal diamond. *Nano Letters*, 12(12):6084–6089, 12 2012.

[34] Chunhui Du, Toeno van der Sar, Tony X. Zhou, Pramey Upadhyaya, Francesco Casola, Huiliang Zhang, Mehmet C. Onbasli, Caroline A. Ross, Ronald L. Walsworth, Yaroslav Tserkovnyak, and Amir Yacoby. Control and local measurement of the spin chemical potential in a magnetic insulator. *Science*, 357(6347):195–198, 7 2017.

[35] Till Lenz, Georgios Chatzidrosos, Zhiyuan Wang, Lykourgos Bougas, Yannick Dumeige, Arne Wickenbrock, Nico Kerber, Jakub Zázvorka, Fabian Kammerbauer, Mathias Kläui, Zeeshawn Kazi, Kai Mei C. Fu, Kohei M. Itoh, Hideyuki Watanabe, and Dmitry Budker. Imaging Topological Spin Structures Using Light-Polarization and Magnetic Microscopy. *Physical Review Applied*, 15(2), 2 2021.

[36] Mark J.H. Ku, Tony X. Zhou, Qing Li, Young J. Shin, Jing K. Shi, Claire Burch, Laurel E. Anderson, Andrew T. Pierce, Yonglong Xie, Assaf Hamo, Uri Vool, Huiliang Zhang, Francesco Casola, Takashi Taniguchi, Kenji Watanabe, Michael M. Fogler, Philip Kim, Amir Yacoby, and Ronald L. Walsworth. Imaging viscous flow of the Dirac fluid in graphene. *Nature*, 583(7817):537–541, 7 2020.

[37] D. Rohner, J. Happacher, P. Reiser, M. A. Tschudin, A. Tallaire, J. Achard, B. J. Shields, and P. Maletinsky. (111)-oriented, single crystal diamond tips for nanoscale scanning probe imaging of out-of-plane magnetic fields. *Applied Physics Letters*, 115(19), 11 2019.

[38] James F. Ziegler, M. D. Ziegler, and J. P. Biersack. SRIM – The stopping and range of ions in matter (2010). *Nuclear Instruments and Methods in Physics Research Section B: Beam Interactions with Materials and Atoms*, 268(11-12):1818–1823, 6 2010.

[39] B. A. Myers, A. Das, M. C. Dartiailh, K. Ohno, D. D. Awschalom, and A. C. Bleszynski Jayich. Probing surface noise with depth-calibrated spins in diamond. *Physical Review Letters*, 113(2):027602, 7 2014.

[40] John Von Neumann and Michael D. Godfrey. First Draft of a Report on the EDVAC. *IEEE*

Annals of the History of Computing, 15(4):27–75, 1993.

[41] Don Monroe. Neuromorphic computing gets ready for the (really) big time. *Communications of the ACM*, 57(6):13–15, 6 2014.

[42] Javier del Valle, Pavel Salev, Federico Tesler, Nicolás M. Vargas, Yoav Kalcheim, Paul Wang, Juan Trastoy, Min Han Lee, George Kassabian, Juan Gabriel Ramírez, Marcelo J. Rozenberg, and Ivan K. Schuller. Subthreshold firing in Mott nanodevices. *Nature 2019 569:7756*, 569(7756):388–392, 5 2019.

[43] Hai Tian Zhang, Priyadarshini Panda, Jerome Lin, Yoav Kalcheim, Kai Wang, John W. Freeland, Dillon D. Fong, Shashank Priya, Ivan K. Schuller, Subramanian K.R.S. Sankaranarayanan, Kaushik Roy, and Shriram Ramanathan. Organismic materials for beyond von Neumann machines. *Applied Physics Reviews*, 7(1):33, 3 2020.

[44] Carver Mead. Neuromorphic electronic systems. *Proceedings of the IEEE*, 78(10):1629–1636, 10 1990.

[45] Masatoshi Imada, Atsushi Fujimori, and Yoshinori Tokura. Metal-insulator transitions. *Reviews of Modern Physics*, 70(4):1039, 10 1998.

[46] Jae Hyung Park, Jim M. Coy, T. Serkan Kasirga, Chunming Huang, Zaiyao Fei, Scott Hunter, and David H. Cobden. Measurement of a solid-state triple point at the metal–insulator transition in VO2. *Nature 2013 500:7463*, 500(7463):431–434, 8 2013.

[47] Pablo Stoliar, Julien Tranchant, Benoit Corraze, Etienne Janod, Marie Paule Besland, Federico Tesler, Marcelo Rozenberg, and Laurent Cario. A Leaky-Integrate-and-Fire Neuron Analog Realized with a Mott Insulator. *Advanced Functional Materials*, 27(11):1604740, 3 2017.

[48] J. H. Ngai, F. J. Walker, and C. H. Ahn. Correlated oxide physics and electronics. *Annual Review of Materials Research*, 44:1–17, 2014.

[49] Tran M. Dao, Partha S. Mondal, Y. Takamura, E. Arenholz, and Jaichan Lee. Metal-insulator transition in low dimensional La0.75Sr 0.25VO3 thin films. *Applied Physics Letters*, 99(11), 9 2011.

[50] Justin S. Brockman, Li Gao, Brian Hughes, Charles T. Rettner, Mahesh G. Samant, Kevin P. Roche, and Stuart S.P. Parkin. Subnanosecond incubation times for electric-field-induced metallization of a correlated electron oxide. *Nature Nanotechnology*, 9(6):453–458, 2014.

[51] G. Stefanovich, A. Pergament, and D. Stefanovich. Electrical switching and Mott transition in VO2. *Journal of Physics Condensed Matter*, 12(41):8837–8845, 10 2000.

[52] P. Diener, E. Janod, B. Corraze, M. Querré, C. Adda, M. Guilloux-Viry, S. Cordier, A. Camjayi, M. Rozenberg, M. P. Besland, and L. Cario. How a dc Electric Field Drives Mott Insulators out of Equilibrium. *Physical Review Letters*, 121(1), 7 2018.

[53] Dasheng Li, Abhishek A. Sharma, Darshil K. Gala, Nikhil Shukla, Hanjong Paik, Suman Datta, Darrell G. Schlom, James A. Bain, and Marek Skowronski. Joule Heating-Induced Metal-Insulator Transition in Epitaxial VO2/TiO2 Devices. *ACS Applied Materials and Interfaces*, 8(20):12908–12914, 5 2016.

[54] Flavio Giorgianni, Joe Sakai, and Stefano Lupi. Overcoming the thermal regime for the electric-field driven Mott transition in vanadium sesquioxide. *Nature Communications*, 10(1), 12 2019.

[55] D. Lee, B. Chung, Y. Shi, G. Y. Kim, N. Campbell, F. Xue, K. Song, S. Y. Choi, J. P. Podkaminer, T. H. Kim, P. J. Ryan, J. W. Kim, T. R. Paudel, J. H. Kang, J. W. Spinuzzi, D. A. Tenne, E. Y. Tsymbal, M. S. Rzchowski, L. Q. Chen, J. Lee, and C. B. Eom. Isostructural metal-insulator transition in VO2. *Science*, 362(6418):1037–1040, 11 2018.

[56] A. Mansingh and Ramadhar Singh. The mechanism of electrical threshold switching in VO2 crystals. *Journal of Physics C: Solid State Physics*, 13(31):5725–5733, 1980.

[57] A. Zimmers, L. Aigouy, M. Mortier, A. Sharoni, Siming Wang, K. G. West, J. G. Ramirez, and Ivan K. Schuller. Role of thermal heating on the voltage induced insulator-metal transition in VO2. *Physical Review Letters*, 110(5), 1 2013.

[58] Yoav Kalcheim, Alberto Camjayi, Javier del Valle, Pavel Salev, Marcelo Rozenberg, and Ivan K. Schuller. Non-thermal resistive switching in Mott insulator nanowires. *Nature Communications*, 11(1), 12 2020.

[59] Javier Del Valle, Yoav Kalcheim, Juan Trastoy, Aliaksei Charnukha, Dimitri N. Basov, and Ivan K. Schuller. Electrically Induced Multiple Metal-Insulator Transitions in Oxide Nanodevices. *Physical Review Applied*, 8(5), 11 2017.

[60] M. M. Qazilbash, M. Brehm, Byung Gyu Chae, P. C. Ho, G. O. Andreev, Bong Jun Kim, Sun Jin Yun, A. V. Balatsky, M. B. Maple, F. Keilmann, Hyun Tak Kim, and D. N. Basov. Mott transition in VO2 revealed by infrared spectroscopy and nano-imaging. *Science*, 318(5857):1750–1753, 12 2007.

[61] P. Neumann, I. Jakobi, F. Dolde, C. Burk, R. Reuter, G. Waldherr, J. Honert, T. Wolf, A. Brunner, J. H. Shim, D. Suter, H. Sumiya, J. Isoya, and J. Wrachtrup. High-precision nanoscale temperature sensing using single defects in diamond. *Nano Letters*, 13(6):2738–2742, 6 2013.

[62] V. M. Acosta, E. Bauch, M. P. Ledbetter, A. Waxman, L. S. Bouchard, and D. Bud-

ker. Temperature dependence of the nitrogen-vacancy magnetic resonance in diamond. *Physical Review Letters*, 104(7), 2 2010.

[63] Ning Wang, Gang Qin Liu, Weng Hang Leong, Hualing Zeng, Xi Feng, Si Hong Li, Florian Dolde, Helmut Fedder, Jörg Wrachtrup, Xiao Dong Cui, Sen Yang, Quan Li, and Ren Bao Liu. Magnetic Criticality Enhanced Hybrid Nanodiamond Thermometer under Ambient Conditions. *Physical Review X*, 8(1):011042, 3 2018.

[64] I. Valmianski, P. Y. Wang, S. Wang, Juan Gabriel Ramirez, S. Guénon, and Ivan K. Schuller. Origin of the current-driven breakdown in vanadium oxides: Thermal versus electronic. *Physical Review B*, 98(19), 11 2018.

[65] Takashi Oka, Ryotaro Arita, and Hideo Aoki. Breakdown of a Mott Insulator: A Nonadiabatic Tunneling Mechanism. *Physical Review Letters*, 91(6), 8 2003.

[66] H. Yamakawa, T. Miyamoto, T. Morimoto, T. Terashige, H. Yada, N. Kida, M. Suda, H. M. Yamamoto, R. Kato, K. Miyagawa, K. Kanoda, and H. Okamoto. Mott transition by an impulsive dielectric breakdown. *Nature Materials*, 16(11):1100–1105, 8 2017.

[67] B. Mayer, C. Schmidt, A. Grupp, J. Bühler, J. Oelmann, R. E. Marvel, R. F. Haglund, T. Oka, D. Brida, A. Leitenstorfer, and A. Pashkin. Tunneling breakdown of a strongly correlated insulating state in v O2 induced by intense multiterahertz excitation. *Physical Review B - Condensed Matter and Materials Physics*, 91(23), 6 2015.

[68] Takashi Oka and Hideo Aoki. Ground-state decay rate for the Zener breakdown in band and mott insulators. *Physical Review Letters*, 95(13), 9 2005.

[69] B. Wu, A. Zimmers, H. Aubin, R. Ghosh, Y. Liu, and R. Lopez. Electric-field-driven phase transition in vanadium dioxide. *Physical Review B - Condensed Matter and Materials Physics*, 84(24), 12 2011.

[70] Woo Ram Lee and Kwon Park. Dielectric breakdown via emergent nonequilibrium steady states of the electric-field-driven Mott insulator. *Physical Review B - Condensed Matter and Materials Physics*, 89(20), 5 2014.

[71] Naoyuki Sugimoto, Shigeki Onoda, and Naoto Nagaosa. Field-induced metal-insulator transition and switching phenomenon in correlated insulators. *Physical Review B - Condensed Matter and Materials Physics*, 78(15), 10 2008.

[72] P. Stoliar, M. Rozenberg, E. Janod, B. Corraze, J. Tranchant, and L. Cario. Nonthermal and purely electronic resistive switching in a Mott memory. *Physical Review B - Condensed Matter and Materials Physics*, 90(4), 7 2014.

[73] Etienne Janod, Julien Tranchant, Benoit Corraze, Madec Querré, Pablo Stoliar, Marcelo

Rozenberg, Tristan Cren, Dimitri Roditchev, Vinh Ta Phuoc, Marie Paule Besland, and Laurent Cario. Resistive Switching in Mott Insulators and Correlated Systems. *Advanced Functional Materials*, 25(40):6287–6305, 10 2015.

[74] Pablo Stoliar, Laurent Cario, Etiene Janod, Benoit Corraze, Catherine Guillot-Deudon, Sabrina Salmon-Bourmand, Vincent Guiot, Julien Tranchant, and Marcelo Rozenberg. Universal electric-field-driven resistive transition in narrow-gap Mott insulators. *Advanced Materials*, 25(23):3222–3226, 6 2013.

[75] Gokul Gopalakrishnan, Dmitry Ruzmetov, and Shriram Ramanathan. On the triggering mechanism for the metal-insulator transition in thin film VO2 devices: Electric field versus thermal effects. *Journal of Materials Science*, 44(19):5345–5353, 10 2009.

[76] M. S. Grinolds, M. Warner, K. De Greve, Y. Dovzhenko, L. Thiel, R. L. Walsworth, S. Hong, P. Maletinsky, and A. Yacoby. Subnanometre resolution in three-dimensional magnetic resonance imaging of individual dark spins. *Nature Nanotechnology*, 9(4):279–284, 2014.

[77] Hinako Kizuka, Takashi Yagi, Junjun Jia, Yuichiro Yamashita, Shinichi Nakamura, Naoyuki Taketoshi, and Yuzo Shigesato. Temperature dependence of thermal conductivity of VO2 thin films across metal-insulator transition. *Japanese Journal of Applied Physics*, 54(5):053201, 4 2015.

[78] V. N. Andreev, F. A. Chudnovskii, A. V. Petrov, and E. I. Terukov. Thermal conductivity of VO2, V3O5, and V2O3. *physica status solidi (a)*, 48(2):K153–K156, 8 1978.

[79] J. E. Graebner. Measurements of thermal conductivity and thermal diffusivity of CVD diamond. *International Journal of Thermophysics*, 19(2 SPEC.ISS.):511–523, 3 1998.

[80] S. Ganichev, E. Ziemann, W. Prettl, and I. Yassievich. Distinction between the Poole-Frenkel and tunneling models of electric-field-stimulated carrier emission from deep levels in semiconductors. *Physical Review B - Condensed Matter and Materials Physics*, 61(15):10361–10365, 2000.

[81] J. Frenkel. On pre-breakdown phenomena in insulators and electronic semi-conductors [3]. *Physical Review*, 54(8):647–648, 1938.

[82] L. Thiel, D. Rohner, M. Ganzhorn, P. Appel, E. Neu, B. Müller, R. Kleiner, D. Koelle, and P. Maletinsky. Quantitative nanoscale vortex imaging using a cryogenic quantum magnetometer. *Nature Nanotechnology*, 11(8):677–681, 8 2016.

[83] Stephen J. Devience, Linh M. Pham, Igor Lovchinsky, Alexander O. Sushkov, Nir Bar-Gill, Chinmay Belthangady, Francesco Casola, Madeleine Corbett, Huiliang Zhang, Mikhail Lukin, Hongkun Park, Amir Yacoby, and Ronald L. Walsworth. Nanoscale

NMR spectroscopy and imaging of multiple nuclear species. *Nature Nanotechnology*, 10(2):129–134, 1 2015.

[84] Xiao Liang Qi and Shou Cheng Zhang. Topological insulators and superconductors. *Reviews of Modern Physics*, 83(4), 10 2011.

[85] Chetan Nayak, Steven H. Simon, Ady Stern, Michael Freedman, and Sankar Das Sarma. Non-Abelian anyons and topological quantum computation. *Reviews of Modern Physics*, 80(3):1083–1159, 9 2008.

[86] S. M. Frolov, M. J. Manfra, and J. D. Sau. Topological superconductivity in hybrid devices. *Nature Physics*, 16(7):718–724, 7 2020.

[87] Peng Zhang, Koichiro Yaji, Takahiro Hashimoto, Yuichi Ota, Takeshi Kondo, Kozo Okazaki, Zhijun Wang, Jinsheng Wen, G. D. Gu, Hong Ding, and Shik Shin. Observation of topological superconductivity on the surface of an iron-based superconductor. *Science*, 360(6385):182–186, 4 2018.

[88] P. D. Johnson, H. B. Yang, J. D. Rameau, G. D. Gu, Z. H. Pan, T. Valla, M. Weinert, and A. V. Fedorov. Spin-orbit interactions and the nematicity observed in the Fe-based superconductors. *Physical Review Letters*, 114(16), 4 2015.

[89] Zhenyu Wang, Jorge Olivares Rodriguez, Lin Jiao, Sean Howard, Martin Graham, G. D. Gu, Taylor L. Hughes, Dirk K. Morr, and Vidya Madhavan. Evidence for dispersing 1D Majorana channels in an iron-based superconductor. *Science*, 367(6473):104–108, 1 2020.

[90] Yangmu Li, Nader Zaki, Vasile O. Garlea, Andrei T. Savici, David Fobes, Zhijun Xu, Fernando Camino, Cedomir Petrovic, Genda Gu, Peter D. Johnson, John M. Tranquada, and Igor A. Zaliznyak. Electronic properties of the bulk and surface states of Fe1+yTe1-xSex. *Nature Materials*, 20(9):1221–1227, 9 2021.

[91] Dongfei Wang, Lingyuan Kong, Peng Fan, Hui Chen, Shiyu Zhu, Wenyao Liu, Lu Cao, Yujie Sun, Shixuan Du, John Schneeloch, Ruidan Zhong, Genda Gu, Liang Fu, Hong Ding, and Hong Jun Gao. Evidence for Majorana bound states in an iron-based superconductor. *Science*, 362(6412):333–335, 10 2018.

[92] Wei Cheng Lee, Shou Cheng Zhang, and Congjun Wu. Pairing state with a time-reversal symmetry breaking in FeAs-based superconductors. *Physical Review Letters*, 102(21), 5 2009.

[93] Lu Chen, Ziji Xiang, Colin Tinsman, Bin Lei, Xianhui Chen, G. D. Gu, and Lu Li. Spontaneous Nernst effect in the iron-based superconductor Fe1+yTe1-xSex. *Physical Review B*, 102(5), 8 2020.

[94] Nader Zaki, Genda Gu, Alexei Tsvelik, Congjun Wu, and Peter D. Johnson. Time-reversal symmetry breaking in the Fe-chalcogenide superconductors. *Proceedings of the National Academy of Sciences of the United States of America*, 118(3), 1 2021.

[95] Lun Hui Hu, P. D. Johnson, and Congjun Wu. Pairing symmetry and topological surface state in iron-chalcogenide superconductors. *Physical Review Research*, 2(2), 4 2020.

[96] J. D. Rameau, N. Zaki, G. D. Gu, P. D. Johnson, and M. Weinert. Interplay of paramagnetism and topology in the Fe-chalcogenide high- Tc superconductors. *Physical Review B*, 99(20), 5 2019.

[97] Zhuozhi Ge, Qiang Zou, Huimin Zhang, Chenhui Yan, Daniel Agterberg, Michael Weinert, and Lian Li. Superconductivity on Edge: Evidence of a One-Dimensional Superconducting Channel at the Edges of Single-Layer FeTeSe Antiferromagnetic Nanoribbons. *ACS Nano*, 14(6):6539–6547, 6 2020.

[98] Da Jiang, Yinping Pan, Shiyuan Wang, Yishi Lin, Connor M. Holland, John R. Kirtley, Xianhui Chen, Jun Zhao, Lei Chen, Shaoyu Yin, and Yihua Wang. Observation of robust edge superconductivity in Fe(Se,Te) under strong magnetic perturbation. *Science Bulletin*, 66(5):425–432, 3 2021.

[99] Mason J. Gray, Josef Freudenstein, Shu Yang F. Zhao, Ryan O'Connor, Samuel Jenkins, Narendra Kumar, Marcel Hoek, Abigail Kopec, Soonsang Huh, Takashi Taniguchi, Kenji Watanabe, Ruidan Zhong, Changyoung Kim, G. D. Gu, and K. S. Burch. Evidence for Helical Hinge Zero Modes in an Fe-Based Superconductor. *Nano Letters*, 19(8):4890–4896, 8 2019.

[100] Rui Xing Zhang, William S. Cole, and S. Das Sarma. Helical Hinge Majorana Modes in Iron-Based Superconductors. *Physical Review Letters*, 122(18), 5 2019.

[101] Rui Xing Zhang, William S. Cole, Xianxin Wu, and S. Das Sarma. Higher-Order Topology and Nodal Topological Superconductivity in Fe(Se,Te) Heterostructures. *Physical Review Letters*, 123(16), 10 2019.

[102] W. Meissner and R. Ochsenfeld. Ein neuer Effekt bei Eintritt der Supraleitfähigkeit. *Die Naturwissenschaften*, 21(44):787–788, 11 1933.

[103] Trond I. Andersen, Bo L. Dwyer, Javier D. Sanchez-Yamagishi, Joaquin F. Rodriguez-Nieva, Kartiek Agarwal, Kenji Watanabe, Takashi Taniguchi, Eugene A. Demler, Philip Kim, Hongkun Park, and Mikhail D. Lukin. Electron-phonon instability in graphene revealed by global and local noise probes. *Science*, 364(6436):154–157, 2019.

[104] A. K. Geim and I. V. Grigorieva. Van der Waals heterostructures. *Nature*, 499(7459):419–425, 2013.

[105] Ying Xu, Yijun Yu, Yuen Yung Hui, Yudan Su, Jun Cheng, Huan Cheng Chang, Yuanbo Zhang, Y. Ron Shen, and Chuanshan Tian. Mapping Dynamical Magnetic Responses of Ultrathin Micron-Size Superconducting Films Using Nitrogen-Vacancy Centers in Diamond. *Nano Letters*, 19(8):5697–5702, 8 2019.

[106] N. M. Nusran, K. R. Joshi, K. Cho, M. A. Tanatar, W. R. Meier, S. L. Bud'Ko, P. C. Canfield, Y. Liu, T. A. Lograsso, and R. Prozorov. Spatially-resolved study of the Meissner effect in superconductors using NV-centers-in-diamond optical magnetometry. *New Journal of Physics*, 20(4), 4 2018.

[107] Dominik Rohner, Lucas Thiel, Benedikt Müller, Mark Kasperczyk, Reinhold Kleiner, Dieter Koelle, and Patrick Maletinsky. Real-space probing of the local magnetic response of thin-film superconductors using single spin magnetometry. *Sensors (Switzerland)*, 18(11), 11 2018.

[108] Adam Paszke, Sam Gross, Francisco Massa, Adam Lerer, James Bradbury, Gregory Chanan, Trevor Killeen, Zeming Lin, Natalia Gimelshein, Luca Antiga, Alban Desmaison, Andreas Kopf, Edward Yang, Zachary DeVito, Martin Raison, Alykhan Tejani, Sasank Chilamkurthy, Benoit Steiner, Lu Fang, Junjie Bai, and Soumith Chintala. PyTorch: An Imperative Style, High-Performance Deep Learning Library. *Advances in Neural Information Processing Systems*, 32, 2019.

[109] Rustem Khasanov, Ritu Gupta, Debarchan Das, Andreas Leithe-Jasper, and Eteri Svanidze. Single-gap versus two-gap scenario: Specific heat and thermodynamic critical field of the noncentrosymmetric superconductor BeAu. *Physical Review B*, 102(1):014514, 7 2020.

[110] F. Bouquet, Y. Wang, R. A. Fisher, D. G. Hinks, J. D. Jorgensen, A. Junod, and N. E. Phillips. Phenomenological two-gap model for the specific heat of MgB2. *Europhysics Letters*, 56(6):856, 12 2001.

[111] Andrei Diaconu, Catalin Martin, Jin Hu, Tijiang Liu, Bin Qian, Zhiqiang Mao, and Leonard Spinu. Possible nodal superconducting gap in Fe1+y(Te 1-xSex) single crystals from ultralow temperature penetration depth measurements. *Physical Review B - Condensed Matter and Materials Physics*, 88(10):104502, 9 2013.

[112] G. M. Luke, A. Keren, L. P. Le, W. D. Wu, Y. J. Uemura, D. A. Bonn, L. Taillefer, and J. D. Garrett. Muon spin relaxation in UPt3. *Physical Review Letters*, 71(9):1466–1469, 1993.

[113] Lin Jiao, Sean Howard, Sheng Ran, Zhenyu Wang, Jorge Olivares Rodriguez, Manfred Sigrist, Ziqiang Wang, Nicholas P. Butch, and Vidya Madhavan. Chiral superconductivity in heavy-fermion metal UTe2. *Nature*, 579(7800):523–527, 3 2020.

[114] V. Grinenko, R. Sarkar, K. Kihou, C. H. Lee, I. Morozov, S. Aswartham, B. Büchner,

P. Chekhonin, W. Skrotzki, K. Nenkov, R. Hühne, K. Nielsch, S. L. Drechsler, V. L. Vadimov, M. A. Silaev, P. A. Volkov, I. Eremin, H. Luetkens, and H. H. Klauss. Superconductivity with broken time-reversal symmetry inside a superconducting s-wave state. *Nature Physics*, 16(7):789–794, 7 2020.

[115] Qi Chao Sun, Tiancheng Song, Eric Anderson, Andreas Brunner, Johannes Förster, Tetyana Shalomayeva, Takashi Taniguchi, Kenji Watanabe, Joachim Gräfe, Rainer Stöhr, Xiaodong Xu, and Jörg Wrachtrup. Magnetic domains and domain wall pinning in atomically thin CrBr3 revealed by nanoscale imaging. *Nature Communications*, 12(1), 12 2021.

[116] A A Serga, A V Chumak, and B Hillebrands. YIG magnonics. *Journal of Physics D: Applied Physics*, 43(26), 2010.

[117] Yi Zhuang You and Zheng Yu Weng. Two-fluid description for iron-based superconductors. *New Journal of Physics*, 16(2):023001, 2 2014.

[118] Gerald D. Mahan. *Many-Particle Physics*. Springer US, 2000.

[119] Yi Zhuang You, Fan Yang, Su Peng Kou, and Zheng Yu Weng. Magnetic and superconducting instabilities in a hybrid model of itinerant/localized electrons for iron pnictides. *Physical Review B - Condensed Matter and Materials Physics*, 84(5), 8 2011.

[120] Xiaoche Wang, Yuxuan Xiao, Chuanpu Liu, Eric Lee-Wong, Nathan J. McLaughlin, Hanfeng Wang, Mingzhong Wu, Hailong Wang, Eric E. Fullerton, and Chunhui Rita Du. Electrical control of coherent spin rotation of a single-spin qubit. *npj Quantum Information*, 6(1), 12 2020.

[121] Cui Zu Chang, Jinsong Zhang, Xiao Feng, Jie Shen, Zuocheng Zhang, Minghua Guo, Kang Li, Yunbo Ou, Pang Wei, Li Li Wang, Zhong Qing Ji, Yang Feng, Shuaihua Ji, Xi Chen, Jinfeng Jia, Xi Dai, Zhong Fang, Shou Cheng Zhang, Ke He, Yayu Wang, Li Lu, Xu Cun Ma, and Qi Kun Xue. Experimental observation of the quantum anomalous Hall effect in a magnetic topological Insulator. *Science*, 340(6129):167–170, 4 2013.

[122] J. G. Checkelsky, R. Yoshimi, A. Tsukazaki, K. S. Takahashi, Y. Kozuka, J. Falson, M. Kawasaki, and Y. Tokura. Trajectory of the anomalous Hall effect towards the quantized state in a ferromagnetic topological insulator. *Nature Physics*, 10(10):731–736, 1 2014.

[123] Xufeng Kou, Shih Ting Guo, Yabin Fan, Lei Pan, Murong Lang, Ying Jiang, Qiming Shao, Tianxiao Nie, Koichi Murata, Jianshi Tang, Yong Wang, Liang He, Ting Kuo Lee, Wei Li Lee, and Kang L. Wang. Scale-invariant quantum anomalous hall effect in magnetic topological insulators beyond the two-dimensional limit. *Physical Review Letters*, 113(3), 9 2014.

[124] Yujun Deng, Yijun Yu, Meng Zhu Shi, Zhongxun Guo, Zihan Xu, Jing Wang, Xian Hui Chen, and Yuanbo Zhang. Quantum anomalous Hall effect in intrinsic magnetic topological insulator MnBi2Te4. *Science*, 367(6480):895–900, 2 2020.

[125] M. Serlin, C. L. Tschirhart, H. Polshyn, Y. Zhang, J. Zhu, K. Watanabe, T. Taniguchi, L. Balents, and A. F. Young. Intrinsic quantized anomalous Hall effect in a moiré heterostructure. *Science*, 367(6480):900–903, 2 2020.

[126] Tingxin Li, Shengwei Jiang, Bowen Shen, Yang Zhang, Lizhong Li, Zui Tao, Trithep Devakul, Kenji Watanabe, Takashi Taniguchi, Liang Fu, Jie Shan, and Kin Fai Mak. Quantum anomalous Hall effect from intertwined moiré bands. *Nature*, 600(7890):641–646, 12 2021.

[127] D. Nevola, H. X. Li, J. Q. Yan, R. G. Moore, H. N. Lee, H. Miao, and P. D. Johnson. Coexistence of Surface Ferromagnetism and a Gapless Topological State in MnBi2Te4. *Physical Review Letters*, 125(11), 9 2020.

[128] Masataka Mogi, Kenji Yasuda, Reika Fujimura, Ryutaro Yoshimi, Naoki Ogawa, Atsushi Tsukazaki, Minoru Kawamura, Kei S. Takahashi, Masashi Kawasaki, and Yoshinori Tokura. Current-induced switching of proximity-induced ferromagnetic surface states in a topological insulator. *Nature Communications*, 12(1), 12 2021.

[129] Ferhat Katmis, Valeria Lauter, Flavio S. Nogueira, Badih A. Assaf, Michelle E. Jamer, Peng Wei, Biswarup Satpati, John W. Freeland, Ilya Eremin, Don Heiman, Pablo Jarillo-Herrero, and Jagadeesh S. Moodera. A High-Temperature Ferromagnetic Topological Insulating Phase by Proximity Coupling. *Nature*, 533(7604):513–516, 5 2016.

[130] A. I. Figueroa, F. Bonell, M. G. Cuxart, M. Valvidares, P. Gargiani, G. Van Der Laan, A. Mugarza, and S. O. Valenzuela. Absence of Magnetic Proximity Effect at the Interface of Bi2Se3 and (Bi,Sb)2Te3 with EuS. *Physical Review Letters*, 125(22), 11 2020.

[131] K. M. Fijalkowski, M. Hartl, M. Winnerlein, P. Mandal, S. Schreyeck, K. Brunner, C. Gould, and L. W. Molenkamp. Coexistence of Surface and Bulk Ferromagnetism Mimics Skyrmion Hall Effect in a Topological Insulator. *Physical Review X*, 10(1):011012, 1 2020.

[132] Di Xiao, Jue Jiang, Jae Ho Shin, Wenbo Wang, Fei Wang, Yi Fan Zhao, Chaoxing Liu, Weida Wu, Moses H.W. Chan, Nitin Samarth, and Cui Zu Chang. Realization of the Axion Insulator State in Quantum Anomalous Hall Sandwich Heterostructures. *Physical Review Letters*, 120(5), 1 2018.

[133] V. Dziom, A. Shuvaev, A. Pimenov, G. V. Astakhov, C. Ames, K. Bendias, J. Böttcher, G. Tkachov, E. M. Hankiewicz, C. Brüne, H. Buhmann, and L. W. Molenkamp. Observation of the universal magnetoelectric effect in a 3D topological insulator. *Nature*

Communications, 8, 5 2017.

[134] Hanshen Tsai, Tomoya Higo, Kouta Kondou, Takuya Nomoto, Akito Sakai, Ayuko Kobayashi, Takafumi Nakano, Kay Yakushiji, Ryotaro Arita, Shinji Miwa, Yoshichika Otani, and Satoru Nakatsuji. Electrical manipulation of a topological antiferromagnetic state. *Nature*, 580(7805):608–613, 4 2020.

[135] K. Yasuda, M. Mogi, R. Yoshimi, A. Tsukazaki, K. S. Takahashi, M. Kawasaki, F. Kagawa, and Y. Tokura. Quantized chiral edge conduction on domain walls of a magnetic topological insulator. *Science*, 358(6368):1311–1314, 12 2017.

[136] Yu Hang Li and Ran Cheng. Spin Fluctuations in Quantized Transport of Magnetic Topological Insulators. *Physical Review Letters*, 126(2), 1 2021.

[137] Dmitry Ovchinnikov, Xiong Huang, Zhong Lin, Zaiyao Fei, Jiaqi Cai, Tiancheng Song, Minhao He, Qianni Jiang, Chong Wang, Hao Li, Yayu Wang, Yang Wu, Di Xiao, Jiun Haw Chu, Jiaqiang Yan, Cui Zu Chang, Yong Tao Cui, and Xiaodong Xu. Intertwined Topological and Magnetic Orders in Atomically Thin Chern Insulator MnBi2Te4. *Nano Letters*, 21(6):2544–2550, 3 2021.

[138] Anyuan Gao, Yu Fei Liu, Chaowei Hu, Jian Xiang Qiu, Christian Tzschaschel, Barun Ghosh, Sheng Chin Ho, Damien Bérubé, Rui Chen, Haipeng Sun, Zhaowei Zhang, Xin Yue Zhang, Yu Xuan Wang, Naizhou Wang, Zumeng Huang, Claudia Felser, Amit Agarwal, Thomas Ding, Hung Ju Tien, Austin Akey, Jules Gardener, Bahadur Singh, Kenji Watanabe, Takashi Taniguchi, Kenneth S. Burch, David C. Bell, Brian B. Zhou, Weibo Gao, Hai Zhou Lu, Arun Bansil, Hsin Lin, Tay Rong Chang, Liang Fu, Qiong Ma, Ni Ni, and Su Yang Xu. Layer Hall effect in a 2D topological axion antiferromagnet. *Nature*, 595(7868):521–525, 7 2021.

[139] Yi Fan Zhao, Ling Jie Zhou, Fei Wang, Guang Wang, Tiancheng Song, Dmitry Ovchinnikov, Hemian Yi, Ruobing Mei, Ke Wang, Moses H.W. Chan, Chao Xing Liu, Xiaodong Xu, and Cui Zu Chang. Even-Odd Layer-Dependent Anomalous Hall Effect in Topological Magnet MnBi2Te4 Thin Films. *Nano Letters*, 21(18):7691–7698, 9 2021.

[140] Haiming Deng, Zhiyi Chen, Agnieszka Wołoś, Marcin Konczykowski, Kamil Sobczak, Joanna Sitnicka, Irina V. Fedorchenko, Jolanta Borysiuk, Tristan Heider, Łukasz Pluciński, Kyungwha Park, Alexandru B. Georgescu, Jennifer Cano, and Lia Krusin-Elbaum. High-temperature quantum anomalous Hall regime in a MnBi2Te4/Bi2Te3 superlattice. *Nature Physics*, 17(1):36–42, 1 2021.

[141] Shiqi Yang, Xiaolong Xu, Yaozheng Zhu, Ruirui Niu, Chunqiang Xu, Yuxuan Peng, Xing Cheng, Xionghui Jia, Yuan Huang, Xiaofeng Xu, Jianming Lu, and Yu Ye. Odd-Even Layer-Number Effect and Layer-Dependent Magnetic Phase Diagrams in MnBi2Te4. *Physical Review X*, 11(1), 1 2021.

[142] Chang Liu, Yongchao Wang, Hao Li, Yang Wu, Yaoxin Li, Jiaheng Li, Ke He, Yong Xu, Jinsong Zhang, and Yayu Wang. Robust axion insulator and Chern insulator phases in a two-dimensional antiferromagnetic topological insulator. *Nature Materials*, 19(5):522–527, 5 2020.

[143] Paul M. Sass, Jinwoong Kim, David Vanderbilt, Jiaqiang Yan, and Weida Wu. Robust A-Type Order and Spin-Flop Transition on the Surface of the Antiferromagnetic Topological Insulator MnBi2Te4. *Physical Review Letters*, 125(3), 7 2020.

[144] M. M. Otrokov, I. I. Klimovskikh, H. Bentmann, D. Estyunin, A. Zeugner, Z. S. Aliev, S. Gaß, A. U.B. Wolter, A. V. Koroleva, A. M. Shikin, M. Blanco-Rey, M. Hoffmann, I. P. Rusinov, A. Yu Vyazovskaya, S. V. Eremeev, Yu M. Koroteev, V. M. Kuznetsov, F. Freyse, J. Sánchez-Barriga, I. R. Amiraslanov, M. B. Babanly, N. T. Mamedov, N. A. Abdullayev, V. N. Zverev, A. Alfonsov, V. Kataev, B. Büchner, E. F. Schwier, S. Kumar, A. Kimura, L. Petaccia, G. Di Santo, R. C. Vidal, S. Schatz, K. Kißner, M. Ünzelmann, C. H. Min, Simon Moser, T. R.F. Peixoto, F. Reinert, A. Ernst, P. M. Echenique, A. Isaeva, and E. V. Chulkov. Prediction and observation of an antiferromagnetic topological insulator. *Nature*, 576(7787):416–422, 12 2019.

[145] J. Q. Yan, Y. H. Liu, D. S. Parker, Y. Wu, A. A. Aczel, M. Matsuda, M. A. McGuire, and B. C. Sales. A-type antiferromagnetic order in MnBi4Te7 and MnBi6Te10 single crystals. *Physical Review Materials*, 4(5), 5 2020.

[146] E. D.L. Rienks, S. Wimmer, J. Sánchez-Barriga, O. Caha, P. S. Mandal, J. Růžička, A. Ney, H. Steiner, V. V. Volobuev, H. Groiss, M. Albu, G. Kothleitner, J. Michalička, S. A. Khan, J. Minár, H. Ebert, G. Bauer, F. Freyse, A. Varykhalov, O. Rader, and G. Springholz. Large magnetic gap at the Dirac point in Bi2Te3/MnBi2Te4 heterostructures. *Nature*, 576(7787):423–428, 12 2019.

[147] Chaowei Hu, Makariy A. Tanatar, Ruslan Prozorov, and Ni Ni. Unusual dynamic susceptibility arising from soft ferromagnetic domains in MnBi8Te13and Sb-doped MnBi2nTen+1(n = 2, 3). *Journal of Physics D: Applied Physics*, 55(5), 2 2022.

[148] Xin Yue Zhang, Yu Xuan Wang, Thomas A. Tartaglia, Thomas Ding, Mason J. Gray, Kenneth S. Burch, Fazel Tafti, and Brian B. Zhou. Ac Susceptometry of 2D van der Waals Magnets Enabled by the Coherent Control of Quantum Sensors. *PRX Quantum*, 2(3), 9 2021.

[149] Shu Zhang and Yaroslav Tserkovnyak. Flavors of Magnetic Noise in Quantum Materials. *Physical Review B*, 106(8), 8 2021.

[150] Hailong Wang, Shu Zhang, Nathan J. McLaughlin, Benedetta Flebus, Mengqi Huang, Yuxuan Xiao, Chuanpu Liu, Mingzhong Wu, Eric E. Fullerton, Yaroslav Tserkovnyak, and Chunhui Rita Du. Noninvasive measurements of spin transport properties of an

antiferromagnetic insulator. *Science Advances*, 8(1):8562, 1 2022.

[151] B. Flebus and Y. Tserkovnyak. Quantum-Impurity Relaxometry of Magnetization Dynamics. *Physical Review Letters*, 121(18), 11 2018.

[152] Chaowei Hu, Kyle N. Gordon, Pengfei Liu, Jinyu Liu, Xiaoqing Zhou, Peipei Hao, Dushyant Narayan, Eve Emmanouilidou, Hongyi Sun, Yuntian Liu, Harlan Brawer, Arthur P. Ramirez, Lei Ding, Huibo Cao, Qihang Liu, Dan Dessau, and Ni Ni. A van der Waals antiferromagnetic topological insulator with weak interlayer magnetic coupling. *Nature Communications*, 11(1), 12 2020.

[153] Andres Castellanos-Gomez, Michele Buscema, Rianda Molenaar, Vibhor Singh, Laurens Janssen, Herre S.J. Van Der Zant, and Gary A. Steele. Deterministic transfer of two-dimensional materials by all-dry viscoelastic stamping. *2D Materials*, 1(1):011002, 4 2014.

[154] Aoyu Tan, Valentin Labracherie, Narayan Kunchur, Anja U.B. Wolter, Joaquin Cornejo, Joseph Dufouleur, Bernd Büchner, Anna Isaeva, and Romain Giraud. Metamagnetism of Weakly Coupled Antiferromagnetic Topological Insulators. *Physical Review Letters*, 124(19), 5 2020.

[155] Jianfeng Guo, Huan Wang, Xueyun Wang, Shangzhi Gu, Shuo Mi, Shiyu Zhu, Jiawei Hu, Fei Pang, Wei Ji, Hong Jun Gao, Tianlong Xia, and Zhihai Cheng. Coexisting Ferromagnetic-antiferromagnetic Phase and Manipulation in Magnetic Topological Insulator MnBi4Te7. *Journal of Physical Chemistry C*, 126(32):13884–13893, 12 2021.

[156] Chaowei Hu, Shang Wei Lien, Erxi Feng, Scott MacKey, Hung Ju Tien, Igor I. Mazin, Huibo Cao, Tay Rong Chang, and Ni Ni. Tuning magnetism and band topology through antisite defects in Sb-doped MnBi4Te7. *Physical Review B*, 104(5), 8 2021.

[157] Steven S.L. Zhang and Shufeng Zhang. Magnon mediated electric current drag across a ferromagnetic insulator layer. *Physical Review Letters*, 109(9), 8 2012.

[158] B. Flebus and Y. Tserkovnyak. Entangling distant spin qubits via a magnetic domain wall. *Physical Review B*, 99(14):140403, 4 2019.

[159] P. J. Brown, K. R.A. Ziebeck, J. Déportes, and D. Givord. Magnetic correlation in itinerant magnetic materials above TC (invited). *Journal of Applied Physics*, 55(6):1881–1886, 1984.

[160] Ka Shen. Magnon Spin Relaxation and Spin Hall Effect Due to the Dipolar Interaction in Antiferromagnetic Insulators. *Physical Review Letters*, 124(7), 2 2020.

[161] Joaquin F. Rodriguez-Nieva, Daniel Podolsky, and Eugene Demler. Probing hydrodynamic

sound modes in magnon fluids using spin magnetometers. *Physical Review B*, 105(17), 5 2022.

[162] Jianpeng Liu and Leon Balents. Anomalous Hall Effect and Topological Defects in Antiferromagnetic Weyl Semimetals: Mn3Sn/Ge. *Physical Review Letters*, 119(8), 8 2017.

[163] Chaowei Hu, Lei Ding, Kyle N. Gordon, Barun Ghosh, Hung Ju Tien, Haoxiang Li, A. Garrison Linn, Shang Wei Lien, Cheng Yi Huang, Scott Mackey, Jinyu Liu, P. V. Sreenivasa Reddy, Bahadur Singh, Amit Agarwal, Arun Bansil, Miao Song, Dongsheng Li, Su Yang Xu, Hsin Lin, Huibo Cao, Tay Rong Chang, Dan Dessau, and Ni Ni. Realization of an intrinsic ferromagnetic topological state in MnBi8Te13. *Science Advances*, 6(30):4275–4297, 7 2020.

[164] A. A. Clerk, K. W. Lehnert, P. Bertet, J. R. Petta, and Y. Nakamura. Hybrid quantum systems with circuit quantum electrodynamics. *Nature Physics 2020 16:3*, 16(3):257–267, 3 2020.

[165] Y Hirayama, K Ishibashi, and K Nemoto. *Hybrid Quantum Systems*. Springer Nature Singapore, Singapore, 2021.

[166] E. R. Macquarrie, T. A. Gosavi, N. R. Jungwirth, S. A. Bhave, and G. D. Fuchs. Mechanical spin control of nitrogen-vacancy centers in diamond. *Physical Review Letters*, 111(22):227602, 11 2013.

[167] Stuart S.P. Parkin, Masamitsu Hayashi, and Luc Thomas. Magnetic domain-wall racetrack memory. *Science*, 320(5873):190–194, 4 2008.

[168] Ioan Mihai Miron, Thomas Moore, Helga Szambolics, Liliana Daniela Buda-Prejbeanu, Stéphane Auffret, Bernard Rodmacq, Stefania Pizzini, Jan Vogel, Marlio Bonfim, Alain Schuhl, and Gilles Gaudin. Fast current-induced domain-wall motion controlled by the Rashba effect. *Nature Materials 2011 10:6*, 10(6):419–423, 5 2011.

[169] Satoru Emori, Uwe Bauer, Sung Min Ahn, Eduardo Martinez, and Geoffrey S.D. Beach. Current-driven dynamics of chiral ferromagnetic domain walls. *Nature Materials 2013 12:7*, 12(7):611–616, 6 2013.

[170] Zhaochu Luo, Aleš Hrabec, Trong Phuong Dao, Giacomo Sala, Simone Finizio, Junxiao Feng, Sina Mayr, Jörg Raabe, Pietro Gambardella, and Laura J. Heyderman. Current-driven magnetic domain-wall logic. *Nature 2020 579:7798*, 579(7798):214–218, 3 2020.

[171] Gong Chen, Tianping Ma, Alpha T. N'Diaye, Heeyoung Kwon, Changyeon Won, Yizheng Wu, and Andreas K. Schmid. Tailoring the chirality of magnetic domain walls by interface engineering. *Nature Communications 2013 4:1*, 4(1):1–6, 10 2013.

[172] B. Flebus, H. Ochoa, P. Upadhyaya, and Y. Tserkovnyak. Proposal for dynamic imaging of antiferromagnetic domain wall via quantum-impurity relaxometry. *Physical Review B*, 98(18):180409, 11 2018.

[173] Maximilian Ruf, Noel H. Wan, Hyeongrak Choi, Dirk Englund, and Ronald Hanson. Quantum networks based on color centers in diamond. *Journal of Applied Physics*, 130(7):70901, 8 2021.

[174] Luka Trifunovic, Fabio L. Pedrocchi, and Daniel Loss. Long-distance entanglement of spin qubits via ferromagnet. *Physical Review X*, 3(4):041023, 12 2014.

[175] F. Dolde, I. Jakobi, B. Naydenov, N. Zhao, S. Pezzagna, C. Trautmann, J. Meijer, P. Neumann, F. Jelezko, and J. Wrachtrup. Room-temperature entanglement between single defect spins in diamond. *Nature Physics 2013 9:3*, 9(3):139–143, 2 2013.

[176] J. P. Tetienne, T. Hingant, J. V. Kim, L. Herrera Diez, J. P. Adam, K. Garcia, J. F. Roch, S. Rohart, A. Thiaville, D. Ravelosona, and V. Jacques. Nanoscale imaging and control of domain-wall hopping with a nitrogen-vacancy center microscope. *Science*, 344(6190):1366–1369, 6 2014.

[177] M. S. Wörnle, P. Welter, M. Giraldo, T. Lottermoser, M. Fiebig, P. Gambardella, and C. L. Degen. Coexistence of Bloch and Néel walls in a collinear antiferromagnet. *Physical Review B*, 103(9):094426, 3 2021.

[178] Kwang Su Ryu, Luc Thomas, See Hun Yang, and Stuart Parkin. Chiral spin torque at magnetic domain walls. *Nature Nanotechnology 2013 8:7*, 8(7):527–533, 6 2013.

[179] Gong Chen, Sang Pyo Kang, Colin Ophus, Alpha T. N'Diaye, Hee Young Kwon, Ryan T. Qiu, Changyeon Won, Kai Liu, Yizheng Wu, and Andreas K. Schmid. Out-of-plane chiral domain wall spin-structures in ultrathin in-plane magnets. *Nature Communications 2017 8:1*, 8(1):1–7, 5 2017.

[180] Saül Vélez, Jakob Schaab, Martin S. Wörnle, Marvin Müller, Elzbieta Gradauskaite, Pol Welter, Cameron Gutgsell, Corneliu Nistor, Christian L. Degen, Morgan Trassin, Manfred Fiebig, and Pietro Gambardella. High-speed domain wall racetracks in a magnetic insulator. *Nature Communications 2019 10:1*, 10(1):1–8, 10 2019.

[181] Dion M.F. Hartmann, Andreas Rückriegel, and Rembert A. Duine. Nonlocal magnon transport in a magnetic domain wall waveguide. *Physical Review B*, 104(6):064434, 8 2021.

[182] Jiahao Han, Pengxiang Zhang, Justin T. Hou, Saima A. Siddiqui, and Luqiao Liu. Mutual control of coherent spin waves and magnetic domain walls in a magnonic device. *Science*, 366(6469):1121–1125, 11 2019.

[183] P. Yan, X. S. Wang, and X. R. Wang. All-magnonic spin-transfer torque and domain wall propagation. *Physical Review Letters*, 107(17):177207, 10 2011.

[184] Chong Wang, Yuan Gao, Hongyan Lv, Xiaodong Xu, and Di Xiao. Stacking Domain Wall Magnons in Twisted van der Waals Magnets. *Physical Review Letters*, 125(24):247201, 12 2020.

[185] Mohammad Mushfiqur Rahman, Avinash Rustagi, Yaroslav Tserkovnyak, and Pramey Upadhyaya. Electrically Active Domain Wall Magnons in Layered van der Waals Antiferromagnets. *Physical Review Letters*, 130(3):036701, 1 2023.

[186] Tiancheng Song, Qi Chao Sun, Eric Anderson, Chong Wang, Jimin Qian, Takashi Taniguchi, Kenji Watanabe, Michael A. McGuire, Rainer Stöhr, Di Xiao, Ting Cao, Jörg Wrachtrup, and Xiaodong Xu. Direct visualization of magnetic domains and moiré magnetism in twisted 2D magnets. *Science*, 374(6571):1140–1144, 11 2021.

[187] Abdelghani Laraoui, Halley Aycock-Rizzo, Yang Gao, Xi Lu, Elisa Riedo, and Carlos A. Meriles. Imaging thermal conductivity with nanoscale resolution using a scanning spin probe. *Nature Communications*, 6, 11 2015.

[188] Luqiao Liu, Chi Feng Pai, Y. Li, H. W. Tseng, D. C. Ralph, and R. A. Buhrman. Spin-torque switching with the giant spin hall effect of tantalum. *Science*, 336(6081):555–558, 5 2012.

[189] David Awschalom, Karl K. Berggren, Hannes Bernien, Sunil Bhave, Lincoln D. Carr, Paul Davids, Sophia E. Economou, Dirk Englund, Andrei Faraon, Martin Fejer, Saikat Guha, Martin V. Gustafsson, Evelyn Hu, Liang Jiang, Jungsang Kim, Boris Korzh, Prem Kumar, Paul G. Kwiat, Marko Lončar, Mikhail D. Lukin, David A.B. Miller, Christopher Monroe, Sae Woo Nam, Prineha Narang, Jason S. Orcutt, Michael G. Raymer, Amir H. Safavi-Naeini, Maria Spiropulu, Kartik Srinivasan, Shuo Sun, Jelena Vučković, Edo Waks, Ronald Walsworth, Andrew M. Weiner, and Zheshen Zhang. Development of Quantum Interconnects (QuICs) for Next-Generation Information Technologies. *PRX Quantum*, 2(1):017002, 1 2021.

[190] Jeffrey A. Brock, Michael D. Kitcher, Pierre Vallobra, Rajasekhar Medapalli, Maxwell P. Li, Marc De Graef, Grant A. Riley, Hans T. Nembach, Stéphane Mangin, Vincent Sokalski, and Eric E. Fullerton. Dynamic Symmetry Breaking in Chiral Magnetic Systems. *Advanced Materials*, 33(39):2101524, 10 2021.

[191] Jiawei Yu, Xuepeng Qiu, Yang Wu, Jungbum Yoon, Praveen Deorani, Jean Mourad Besbas, Aurelien Manchon, and Hyunsoo Yang. Spin orbit torques and Dzyaloshinskii-Moriya interaction in dual-interfaced Co-Ni multilayers. *Scientific Reports 2016 6:1*, 6(1):1–9, 9 2016.

[192] Kowsar Shahbazi, Joo Von Kim, Hans T. Nembach, Justin M. Shaw, Andreas Bischof, Marta D. Rossell, Vincent Jeudy, Thomas A. Moore, and Christopher H. Marrows. Domain-wall motion and interfacial Dzyaloshinskii-Moriya interactions in Pt/Co/Ir(tIr)/Ta multilayers. *Physical Review B*, 99(9):094409, 3 2019.

[193] Tony X. Zhou, Joris J. Carmiggelt, Lisa M. Gächter, Ilya Esterlis, Dries Sels, Rainer J. Stöhr, Chunhui Du, Daniel Fernandez, Joaquin F. Rodriguez-Nieva, Felix Büttner, Eugene Demler, and Amir Yacoby. A magnon scattering platform. *Proceedings of the National Academy of Sciences of the United States of America*, 118(25):e2019473118, 6 2021.

[194] J. P. Tetienne, T. Hingant, L. J. Martínez, S. Rohart, A. Thiaville, L. Herrera Diez, K. Garcia, J. P. Adam, J. V. Kim, J. F. Roch, I. M. Miron, G. Gaudin, L. Vila, B. Ocker, D. Ravelosona, and V. Jacques. The nature of domain walls in ultrathin ferromagnets revealed by scanning nanomagnetometry. *Nature Communications 2015 6:1*, 6(1):1–6, 4 2015.

[195] Jairo Sinova, Sergio O. Valenzuela, J. Wunderlich, C. H. Back, and T. Jungwirth. Spin Hall effects. *Reviews of Modern Physics*, 87(4):1213–1260, 10 2015.

[196] I. Dzyaloshinsky. A thermodynamic theory of "weak" ferromagnetism of antiferromagnetics. *Journal of Physics and Chemistry of Solids*, 4(4):241–255, 1 1958.

[197] Tôru Moriya. Anisotropic Superexchange Interaction and Weak Ferromagnetism. *Physical Review*, 120(1):91, 10 1960.

[198] C. Moreau-Luchaire, C. Moutafis, N. Reyren, J. Sampaio, C. A.F. Vaz, N. Van Horne, K. Bouzehouane, K. Garcia, C. Deranlot, P. Warnicke, P. Wohlhüter, J. M. George, M. Weigand, J. Raabe, V. Cros, and A. Fert. Additive interfacial chiral interaction in multilayers for stabilization of small individual skyrmions at room temperature. *Nature Nanotechnology 2016 11:5*, 11(5):444–448, 1 2016.

[199] Hongxin Yang, André Thiaville, Stanislas Rohart, Albert Fert, and Mairbek Chshiev. Anatomy of Dzyaloshinskii-Moriya Interaction at Co/Pt Interfaces. *Physical Review Letters*, 115(26):267210, 12 2015.

[200] J. P. Tetienne, L. Rondin, P. Spinicelli, M. Chipaux, T. Debuisschert, J. F. Roch, and V. Jacques. Magnetic-field-dependent photodynamics of single NV defects in diamond: an application to qualitative all-optical magnetic imaging. *New Journal of Physics*, 14(10):103033, 10 2012.

[201] Shu Zhang and Oleg Tchernyshyov. Ferromagnetic domain wall as a nonreciprocal string. *Physical Review B*, 98(10):104411, 9 2018.

[202] Anthony K. C. Tan, Hariom Jani, Michael Högen, Lucio Stefan, Claudio Castelnovo,

Daniel Braund, Alexandra Geim, Annika Mechnich, Matthew S. G. Feuer, Helena S. Knowles, Ariando Ariando, Paolo G. Radaelli, and Mete Atatüre. Revealing emergent magnetic charge in an antiferromagnet with diamond quantum magnetometry. *Nature Materials 2023*, pages 1–7, 12 2023.

[203] Uri Vool, Assaf Hamo, Georgios Varnavides, Yaxian Wang, Tony X. Zhou, Nitesh Kumar, Yuliya Dovzhenko, Ziwei Qiu, Christina A.C. Garcia, Andrew T. Pierce, Johannes Gooth, Polina Anikeeva, Claudia Felser, Prineha Narang, and Amir Yacoby. Imaging phonon-mediated hydrodynamic flow in WTe2. *Nature Physics 2021 17:11*, 17(11):1216–1220, 9 2021.

[204] Konstantin Y. Guslienko and Andrei N. Slavin. Magnetostatic Green's functions for the description of spin waves in finite rectangular magnetic dots and stripes. *Journal of Magnetism and Magnetic Materials*, 323(18-19):2418–2424, 10 2011.

[205] David A. Broadway, Sam C. Scholten, Cheng Tan, Nikolai Dontschuk, Scott E. Lillie, Brett C. Johnson, Guolin Zheng, Zhenhai Wang, Artem R. Oganov, Shangjie Tian, Chenghe Li, Hechang Lei, Lan Wang, Lloyd C.L. Hollenberg, and Jean Philippe Tetienne. Imaging Domain Reversal in an Ultrathin Van der Waals Ferromagnet. *Advanced Materials*, 32(39):2003314, 10 2020.

[206] U. D. Jentschura and J. Sapirstein. Green function of the Poisson equation: D = 2, 3, 4. *Journal of Physics Communications*, 2(1):015026, 1 2018.

[207] F. London and H. London. The electromagnetic equations of the supraconductor. *Proceedings of the Royal Society of London. Series A - Mathematical and Physical Sciences*, 149(866):71–88, 3 1935.